Dissertation

Simulation of the Urea-Water-Solution Preparation and Ammonia-Homogenization with a Validated CFD-Model for the Optimization of Automotive SCR-Systems

ausgeführt zum Zwecke der Erlangung des akademischen Grades eines Doktors der technischen Wissenschaften (Dr. techn.) unter der Leitung von

Prof. Dr. Bernhard Geringer

E315

Institut für Fahrzeugantriebe und Automobiltechnik

und (Zweitgutachter)

Prof. Dr. David Allen Gosman

Imperial College London

eingereicht an der Technischen Universität Wien

Fakultät für Maschinenwesen und Betriebswissenschaften

von

Dipl.-Phys. Simon Fischer

Matrikelnummer 0827232

Klostergasse 9/9, 1180 Wien

Wien, 19.09.2012

Acknowledgements - Danke

"For a successful technology, reality must take precedence over public relations,
for nature cannot be fooled."

Richard P. Feynman

Abstract

The Selective Catalytic Reduction (SCR) is a promising approach to meet future legislation regarding the nitric oxide emissions of Diesel engines. In automotive applications a liquid urea-water-solution (UWS) is injected into the hot exhaust gas that evaporates and reacts to ammonia vapor, acting as the reducing agent on a downstream SCR-catalyst. Significant criteria for an efficient SCR-system are a fast UWS preparation and a high ammonia uniformity at the catalyst intake.

This work presents the determination, adaption and integration of relevant submodels to establish a CFD simulation method for the evaluation of UWS based SCR-systems. A systematic experimental and numerical breakdown of the UWS preparation and ammonia mixing process is carried out to determine the relevant modelling depth for each step. A UWS decomposition model is implemented and validated with literature data. On the basis of video analysis of liquid film formation and available literature data, a multi-regime droplet-wall-interaction model is adapted to UWS. The necessity of a conjugate heat transfer model of the exhaust system walls, to correctly capture wall temperature dependent droplet impingement and liquid film boiling is proved. Validation is performed by transient infrared thermal imaging. Buffering of ammonia by liquid film formation is analyzed with the CFD-model and correlated to transient FTIR-concentration data. The liquid film decomposition model is validated by a comparison to a liquid film probe analysis. The resulting liquid phase model covers a wide range of operating conditions, from massive wall wetting at low- to classical Leidenfrost phenomena at high exhaust temperatures.

The liquid phase UWS model is applied to a passenger car SCR-system, with a mixing element creating a turbulent swirling flow upstream of the SCR-catalyst. The impact of the turbulence model and the numerical differencing scheme on the prediction of the mixing process of the gaseous ammonia is analyzed. The study proves the high impact of an advanced second order differencing scheme on the species transport. It further shows that Reynolds-averaged k-ε-models systematically underestimate the turbulence level in the swirl flow and, in consequence, the turbulent diffusion and homogenization of the ammonia vapor. In contrast, a Reynolds-Stress-model (RSM) leads to improved predictions by accounting for the anisotropic character of turbulence in the swirl. The relevance of a detailed simulation of the liquid phase dynamics and -evaporation for precise ammonia homogeneity predictions is proved. Numerical results are validated with measurements of back pressure and the spatial ammonia distribution at the catalyst.

The presented method allows a precise prediction of the ammonia homogenization and an estimation of liquid film deposition risks for a wide range of operating conditions.

Kurzfassung

Die Selektive Katalytische Reaktion stellt einen vielversprechenden Ansatz zur Erfüllung zukünfiger gesetzlicher Stickoxidgrenzwerte für Dieselmotoren dar. In der automobilen Anwendung basiert das Verfahren auf der Injektion einer Harnstoff-Wasser-Lösung (HWL) in das heiße Abgassystem. Nach der Verdampfung des Wassers aus dem feinen Spray, zersetzt sich der Harnstoff in einem chemo-physikalischen Prozess zu gasförmigem Ammoniak. Dieses dient an einem stromab liegenden SCR-Katalysator der chemischen Reduktion der motorischen Stickoxide. Wesentliche Kriterien eines effizienten SCR-Systems stellen die schnelle Aufbereitung der HWL und eine hohe Gleichverteilung von Ammoniak am Katalysator dar.

Die vorliegenden Arbeit beschreibt die Bestimmung, Anpassung und Integration relevanter Sub-Modelle für ein präzises CFD-Modell der Prozesskette vor dem SCR-Katalysator. Auf Basis von Literaturdaten wird ein Modell der HWL-Zersetzung implementiert. Mit Hilfe von Videoanalysen der Wandfilmbildung und Literaturdaten wird ein komplexes Tropfen-Wand-Interaktionsmodell für das HWL-Spray adaptiert. Die thermische Modellierung von Rohrwänden und Mischerelementen ist dabei von hoher Relevanz für eine korrekte Prognose der Wandtemperaturen, und damit den Tropfen-Wand-Kontakt und die Wandfilmbildung. Validierung erfolgt durch Infrarot-Thermografie. Das Zwischenspeichern von Ammoniak durch Wandfilm wird mit dem CFD-Modell analysiert und mit transienten FTIR- Ammoniak-Konzentrationsmessungen korreliert. Eine Laboranalyse der Wandfilmzusammensetzung dient der Überprüfung des HWL-Zersetzungsmodells. Das abgestimmte Modell beschreibt das Verhalten der HWL für einen weiten Betriebsbereich, von ausgeprägter Wandfilmbildung bis zum thermischen Aufbruch von Tropfen jenseits der Leidenfrosttemperatur.

Das Modell wird zur Simulation einer seriennahen PKW-SCR-Anlage, mit einem Drall-Mischerelement angewendet. Der Einfluss des Turbulenzmodells und des räumlichen Diskretisierungsschemas auf die Ammoniakhomogenisierung wird überprüft. Die Studie zeigt, dass etablierte k-ε-Modelle das Turbulenzniveau, damit die turbulente Diffusion und in Folge die Ammoniakhomogenisierung in der Drallströmung unterschätzen. Ein Reynolds- Spannungs-Modell (RSM) führt durch Berücksichtigung der Anisotropie der Turbulenz zu deutlich besseren Vorhersagen. Ferner zeigt sich eine hohe Sensitivität des Speziestransports bezüglich der numerischen Diskretisierung. Die Relevanz des Tropfen-Wand-Interaktionsmodells für die Prognose der Homogenisierung am Katalysator wird dargelegt. Die numerischen Ergebnisse werden mit Messungen der Reduktionsmittelverteilung und Gegendruckmessungen des Mischsystems validiert.

Die dargelegte Methode ermöglicht eine präzise Vorhersage der HWL- Aufbereitung und Ammoniak- Gleichverteilung für einen weiten Betriebsbereich.

Contents

Nomenclature

Mathematical Symbols (arabic)

A	m^2	Surface area
A	$-$	Bai-model splashing limit factor (dry wall)
A	s^{-1}	Reaction Frequency factor
A_w	$-$	Bai-model splahing limit factor (wetted wall)
B	$-$	Bai-model regime limit temperature factor
c	$-$	Pool-boiling model tuning factor
C	$-$	Constant of proportionality
c_p	$J/(kg \cdot K)$	Specific heat
D	m	Diameter
d	m	Liquid film thickness
E	J	Activation Energy
f	$-$	Numerical truncation error
h	$W/(m^2 \cdot K)$	Heat transfer coefficient
h	J/kg	Latent heat
k	$W/(m \cdot K)$	Heat conductivity
k	m^2/s^2	Turbulent kinetic energy
K	$-$	Kuhnke droplet stabilty number
La	$-$	Laplace-number
m	kg	Mass
M	g/mol	Molecular weight

Nu	–	Nusselt-number
O	–	Order of magnitude
p	Pa	Pressure
q	W/m^2	Heat flux density
q	–	Rosin-Rammler distribution, exponent
R	m	Maximum radius
R	$J/(mol \cdot K)$	Gas constant
r	m	Radius
r_s	m	Surface roughness
Re	–	Reynolds-number
S	–	Swirl-number
Sc	–	Schmidt-number
Sh	–	Sherwood-number
T	K	Temperature
t	s	Time
u	m/s	Velocity
u, v, w	m/s	Velocity components
V	m^2/s	Laminar diffusion velocity
We	–	Weber-number
x	mol/mol	Mole fraction
x	m	Position, length
x	m	Rosin-Rammler distribution, factor
Y	kg/kg	Mass fraction
Z	–	Heat transfer coefficient correction factor

Mathematical Symbols (greek)

α	$W/(m \cdot K)$	Heat conductivity
∂	$-$	Partial differencing operator
Δ	$-$	Absolute difference operator
Γ	mm^2/s	Characteristic droplet diminishing rate
Γ	m^2/s	Molecular diffusivity
ε	m^2/s^3	Turbulent dissipation
μ	$Pa \cdot s$	Viscosity
ν	$-$	Partial pressure factor
ρ	kg/m^3	Density
σ	N/m	Surface tension
τ	s/mm^2	Characteristic droplet diminishing timescale
ψ	$1/m$	Rosin-Rammler probability density function
Ω	m	Molecule collision integral

Subscripts, Superscripts

amb	Ambient
d	Droplet
$exhaust$	Exhaust gas
f	Fibre
g	Gaseous
H_2O	Water
l	Liquid
L	Leidenfrost
m	Component number

max	Maximum
min	Minimum
N	Counter Maximum
n	Counter
s	Sliding
s	Surface
$sect$	Cross section
sat	Saturation
sf	Surface factor
t	Turbulent
th	Thermolysis
$urea$	Urea
vap	Evaporative
w	Wall
wb	Wet bulb

Abbreviations

$BRIC$	Brazil, Russia, India, China
CFD	Computattional fluid dynamics
CHF	Critical heat flux
CHT	Conjugate heat transfer
CLD	Chemo luminescence detection
CYA	Cyanur acid
DDM	Discrete droplet modelling
DL	Diffusion limit model

DNS	Direct numerical simulation
DPF	Diesel particulate filter
ED	Effective diffusion model
EGR	Exhaust gas recirculation
$EUDC$	Extra-urban driving cycle
$FTIR$	Fourier-transform infrared (spectroscopy)
FTP	US American driving cycle
IFA	Institute for powertrains and automotive technology
IR	Infra-red
LDA	Laser-Doppler anemometry
LES	Large-eddy simulation
$MARS$	Monotone advection and reconstruction scheme
$NEDC$	New European driving cycle
NO_x	Nitrogen oxides
OP	Operating point
PDA	Particle-Doppler anemometry
$RANS$	Reynolds-average Navier-Stokes
RM	Rapid mixing model
RNG	Reynolds normalization group
RS	Reynolds stress
RSM	Reynolds stress model
SCR	Selective Catalytic Reduction
SMD	Sauter mean diameter
TGA	gravimetric analysis
TKE	Turbulent kinetic energy

TVD	Total variation diminishing
UD	Upwind differencing
UDC	Urban driving cycle
UI	Uniformity-index
UWS	Urea-water-solution

1 Introduction: SCR in Automotive Technology

The turbocharged Diesel engine has achieved a high market share of nearly $50\,\%$ in the passenger car segment on the European market [1]. Though currently at a low absolute level, a constantly rising number of clean Diesel engines is on the road in the US market and increasing shares are to be expected in the future. In India nearly $40\,\%$ of LDV are Diesel powered, followed by Russia ($20\,\%$), China ($12\,\%$) and Brazil ($6\,\%$), with enormous increases in absolute numbers, due to the significant market growth in the BRIC states [1].

The main reasons for these trends are the Diesel engines's comparably high thermal efficiency, leading to a superior fuel- and therefore driving cost economy, and its favorable torque characteristics. However, the disadvantage of higher emissions of particles and nitric oxides, caused by the non-premixed Diesel combustion, remains. In order to cope with the future emission legislation, a further drastic decrease of NO_x- and particle emissions is therefore necessary for any Diesel engine powered vehicle, see Figure 1.1. Particularly the nitric oxide
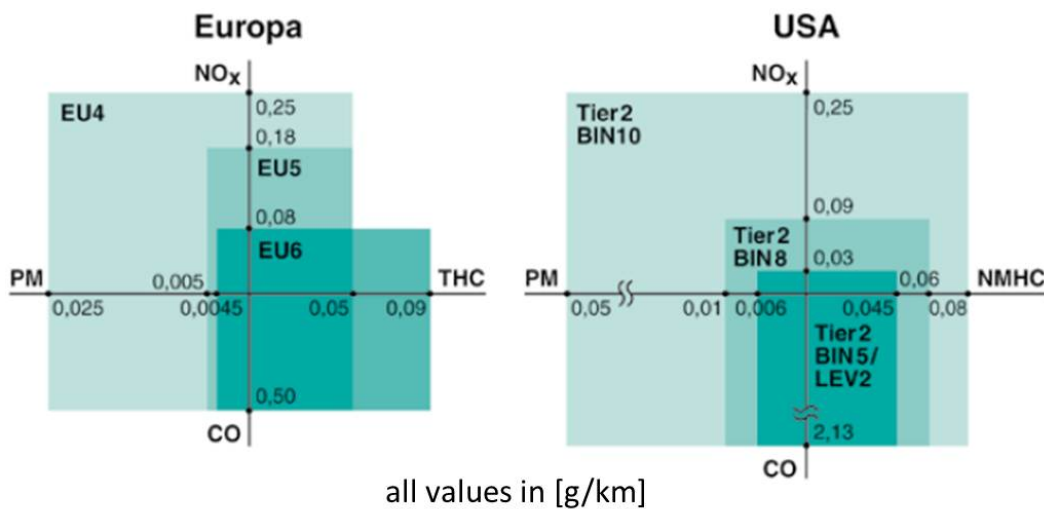
Figure 1.1:   *Development of legislative emission standards for light duty vehicles with Diesel engines on the European and US market [2]*

emissions will be further significantly restricted with the introduction of the European exhaust legislation step EURO VI and the American Tier 2 BIN 5 standards.

Similar trends can be observed in the heavy duty vehicle sector and in off-road applications [3]. Even in the non-road sector, including ships and trains, severe further restriction of NO_x-emissions are to be expected [1, 4]. Moreover, as e.g. the introduction of EURO V in Russia in 2014 indicates, other markets - including the BRIC states - can be expected to follow those restriction trends, even if with a certain temporal delay.

The necessary decrease of nitric oxides can be accomplished by engine modifications in combination with exhaust gas aftertreatment. However, internal measures like e.g. cooled EGR, two-stage turbocharging, optimization of fuel injection technology (high pressure injection, multiple injection) or closed loop combustion control, etc., as a stand alone solution have reached their limits to fulfill the present and upcoming stringent emission regulations with reasonable effort [5]. This is predominantly due to the trade-off between particulate matter and nitrogen oxide emissions, that intrinsically arises from the Diesel combustion process, see Figure 1.2. In addition, fuel economy measures like downsizing and down-speeding may
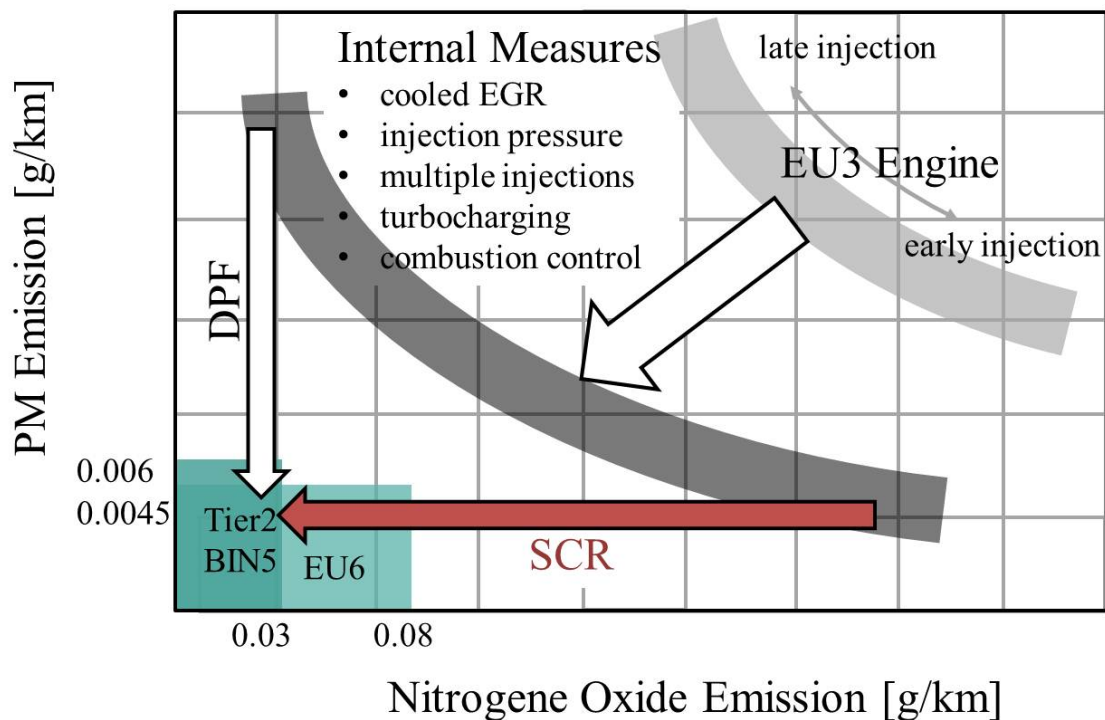
Figure 1.2:   *Trade-off between NO_x and PM- emissions of Diesel engines and possible reduction measures*

further increase combustion peak temperatures and therefore NO_x-raw emissions by up to $50\,\%$ [3]. For those reasons, exhaust gas aftertreatment has become a necessity in order to cope with both, CO_2- and emission-reduction. With respect to nitrogen oxide emissions in the sector of midsized and big passenger cars, the Selective Catalytic Reduction (SCR) with

ammonia as a reducing agent is considered as a promising technical solution to cope with this challenge. Already established in the heavy-duty sector, first systems have currently been applied to series-production passenger cars and an increase of SCR technology is to be expected on all markets and sectors [1].

In mobile applications, the SCR technology is based on the injection of a liquid urea-water-solution (UWS) into the exhaust system. In the hot exhaust, the water evaporates and the remaining urea decomposes to ammonia. Ammonia vapor is then used as the reducing agent for nitrogen oxides in a catalytic converter, located downstream of the injection position. Figure 1.3 gives an overview of the UWS preparation process details.
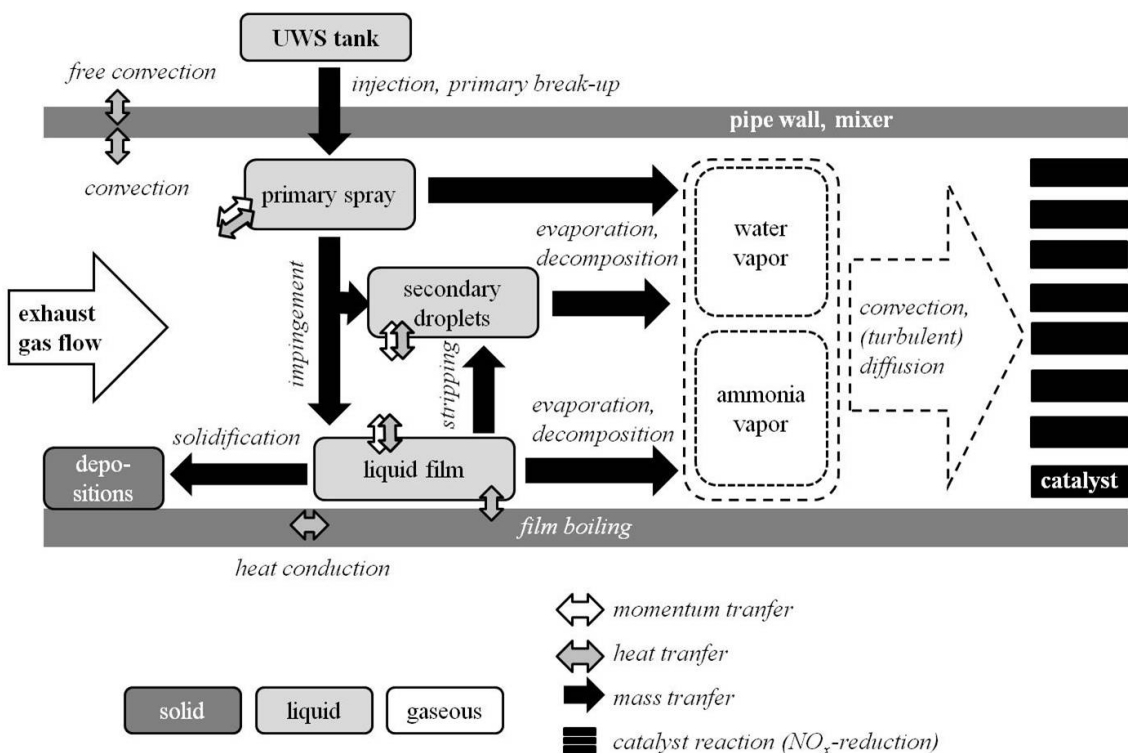
Figure 1.3: *Principle of the UWS based SCR for automotive applications: major subprocesses upstream of the SCR catalyst*

The urea-water-solution is injected as a fine spray, which interacts with the hot exhaust gas and surfaces of the exhaust system. Aerodynamic forces and heat are transferred from the turbulent exhaust flow to the droplets of the spray. After the evaporation of water from the droplets (drying), the remaining urea melts, evaporates and decomposes to ammonia and isocyanic acid in a thermolytic process, see Equation 1.1.

$$(NH_2)_2CO \rightleftharpoons HNCO + NH_3 \qquad \text{(Thermolysis)} \qquad (1.1)$$
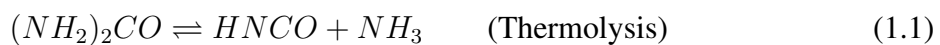
In presence of water vapor, isocyanic acid gets hydrolysed to another mole of ammonia according to Equation 1.2 [6].

$$HNCO + H_2O \rightleftharpoons NH_3 + CO_2 \qquad \text{(Hydrolysis)} \qquad (1.2)$$

Depending on spray characteristics and the geometric setup, UWS droplets may impinge on the hot surfaces of the exhaust system in different scenarios that range from an elastic rebound through the formation of secondary droplets by a thermal- or kinematic breakup, to wall wetting. In the latter case urea is stored in a wall film and, if not reacting to undesired deposits, is decomposed to ammonia via the above mentioned mechanisms. The released ammonia vapor is then transported downstream by the turbulent exhaust gas and mixed by convection and diffusion processes. In most automobile applications static mixing elements are introduced into the SCR system, on which the UWS spray is targeted. Those elements enhance both, the decomposition of UWS and the turbulent mixing of ammonia. In a downstream catalytic converter ammonia reduces nitrogen oxides from the combustion process to elementary nitrogen according to Equations 1.3 to 1.6 [6]:

$$4NH_3 + 4NO + O_2 \rightleftharpoons 4N_2 + 6H_2O \qquad (1.3)$$

$$2NH_3 + NO + NO_2 \rightleftharpoons 2N_2 + 3H_2O \qquad (1.4)$$

$$4NH_3 + 6NO \rightleftharpoons 5N_2 + 6H_2O \qquad (1.5)$$

$$8NH_3 + 6NO_2 \rightleftharpoons 7N_2 + 12H_2O \qquad (1.6)$$
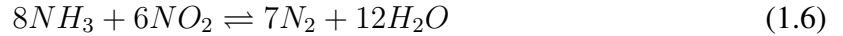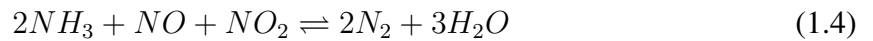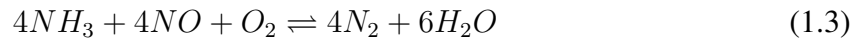
Even if these chemical mechanisms and related issues are put aside, a number of challenges arise from the complex physical UWS preparation and ammonia mixing process upstream of the SCR-catalyst in transient automotive applications:

The efficiency of tailpipe NO_x-emission reduction during any driving cycle is directly connected to an as early as possible start of UWS injection. However, the conversion from ammonia to urea is not taking place at significant rates below $180\,°C$ and the NO_x-reduction reactions on the catalyst not below $200\,°C$ (catalyst light-off). To prove the relevance of those limits, Figure 1.4 shows the transient exhaust temperature development and the temperature frequency of occurrence in a typical passenger car SCR system during the NEDC test cycle [1].

As the graphs reveal, for a significant period of the driving cycle (during UDC) the exhaust gas temperature in the region of the SCR system (UWS injector to SCR catalyst) is well below or close to $180\,°C$. On the calibration side, intelligent thermomanagement measures to realize a fast heat-up of the complete system with minimum fuel economy penalties are therefore necessary. On the SCR system development side, the efficiency of UWS preparation has to be extended to as-low-as possible temperature ranges. At higher engine loads (during the EUDC), high exhaust gas volume flows lead to extremely short UWS spray residence times in the mixing section, which might also result in insufficient preparation of UWS within the
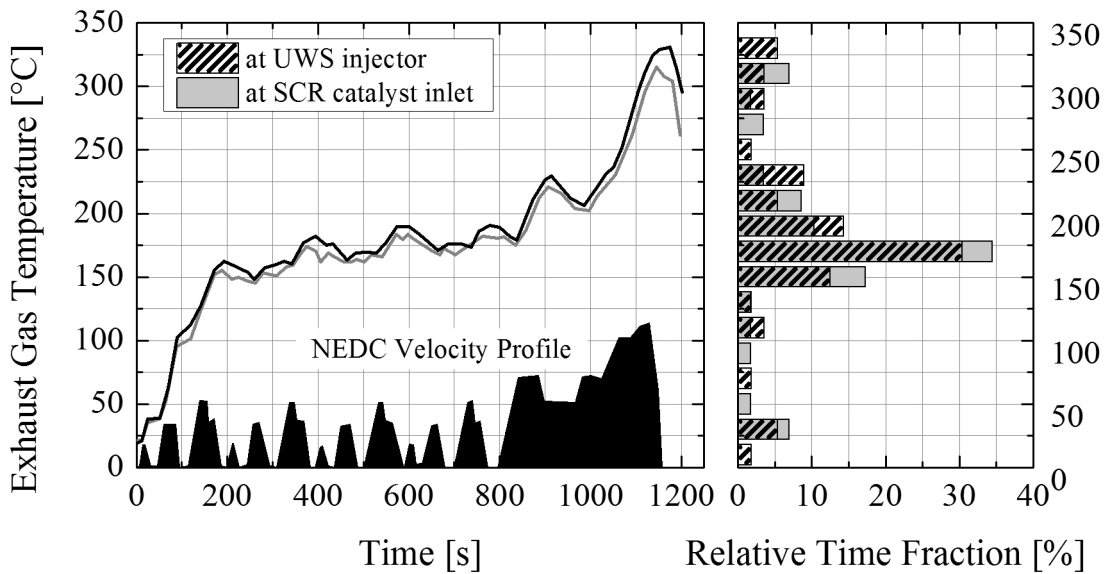
Figure 1.4: *Transient exhaust temperatures (left) and duration of temperature ranges (right) in a typical passenger car SCR system during NEDC, data taken from [1]*

SCR system. This may lead to a misuse of SCR catalyst volume for the UWS decomposition instead of the desired NO_x reduction [6].

An insufficiently fast preparation of UWS may lead to liquid film formation and - in a worst case scenario - solid deposits in the SCR system or on the catalyst brick. As an example Figure 1.5 shows typical deposits that result from undesired chemical reactions of unprepared urea.
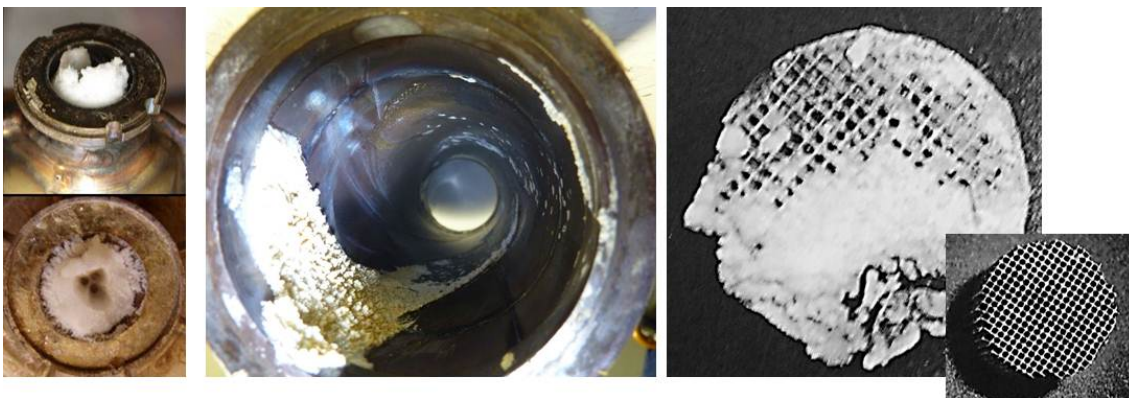
Figure 1.5: *Undesired solid deposits in an SCR system resulting from poor thermal- and flow management in the mixing section, from left to right: at the UWS injector tip [7], in the exhaust pipe [8], on the catalyst surface [9]*

The formation of intermediate liquid film means a temporal buffering of the reducing agent,

permanent solid by-products may even mean a loss of it. Both phenomena make any controlled injection strategy impossible. Moreover, solid deposits often results in increased back pressure of the system or even material deterioration [10]. For obvious reasons avoiding failures of UWS preparation by intelligent SCR system design is an imperative.

A sufficient ammonia preparation and -mixing is however related to measures (e.g. mixing elements) that increase the system's back pressure even under regular operation. Again, a trade off between CO_2-emissions (i.e. fuel economy) and NO_x-emission reduction arises, which demands for an optimum SCR system layout.

Another challenge is the minimization of UWS consumption, in order to to stretch refill intervals to a maximum and optimize usage economy. In order to gain customer acceptance in the passenger car sector, refills have to be retarded to the service interval. At the same time, the integration of extended UWS tanks is a packaging issue [1].

Resulting from those demands, four significant criteria for an efficient SCR-system can be derived: first, a fast mixture preparation of the UWS; second, a high ammonia uniformity at the SCR-catalyst; third, both of them realized under a wide range of engine operating conditions with; fourth, minimum back pressure. Only if those criteria are fulfilled, a sufficient reduction of NO_x-emissions can be achieved with minimum UWS-consumption and CO_2-penalty, minimal catalyst volumes and without ammonia slip into the atmosphere.

In passenger car applications, the challenge is even more pronounced due to the transient engine operation conditions and the stringent packaging limitations, leading to short preparation and mixing pipes. To meet all those challenges, a carefully designed mixing section including adequate mixing facilities and a corresponding UWS injection system is an imperative. In spite of the successful market launch of the SCR technology [2], there still exists a high potential for its optimization. However, a thorough understanding of all sub-processes that are included in the formation of gaseous ammonia from the UWS is a precondition.

The present work describes a methodic approach to understand and predict the complex processes of SCR mixing systems by numerical CFD simulation combined with experimental investigations to validate the model. On the basis of a validated model, multiphase CFD simulation is able to support the development of SCR systems in a very efficient time- and cost-saving way. However, the complexity of the UWS preparation process leads to a number of challenges that a CFD model has to cope with. First, it requires the correct description of the chemo-physical decomposition of the UWS. Moreover, droplet dynamics in the turbulent flow field have to be understood and predicted in detail and models for simulating the droplet wall-interaction have to be adapted to SCR-CFD-simulation. Finally, a precise simulation of ammonia vapor mixing in the turbulent exhaust gas upstream of the SCR-catalyst is necessary.

2 Literature Review

The process chain of UWS preparation and ammonia homogenization upstream of the catalyst is in its major steps well understood. However, significant uncertainties remain with respect to details of the involved subprocesses and their relevance to the overall SCR process. The following section gives an overview on the state of knowledge on the UWS decomposition, spray dynamics, including spray-wall contact and the mixing of ammonia vapor in the turbulent flow. Relevant experimental studies and modelling approaches of those steps are reviewed and available CFD-simulations of the processes are presented. Uncertainties that demand further numerical and experimental research to implement a predictive CFD-model of the SCR processes upstream of the catalyst are pointed out. In accordance with the present work's focus, the review is limited to the processes upstream of the SCR catalyst, while the chemical reduction of nitrogen oxides in the catalytic converter is not discussed in detail here.

2.1 Decomposition of Urea-water-solution and Modelling Approaches

It is commonly accepted that the decomposition of UWS from spray droplets happens basically in two separate steps. In a first stage, water evaporates from the solution, which leads to an increase of urea concentration within the droplet. During the end of this drying process, the droplet temperature increases and urea decomposes to ammonia and isocyanic acid in a thermolysis reaction, see Equation 1.1 [11]. However, there exists uncertainty in literature on the physical state of UWS when urea decomposing sets in: Proposals range from a direct sublimation from pure solid urea [12], via melting and subsequent evaporation [13, 14], to a decomposition from a highly concentrated UWS [15]. A study that gives some insight has very recently been published by Abu-Ramadan et al. [11] and will be discussed in Section 2.1.2. It is further not clarified, if gaseous urea exists for a significant time as an intermediate state before the thermolysis sets in [16]. Most studies indicate that the thermolysis takes place at a much higher rate than the urea evaporation, leading to the model assumption that it occurs instantaneously from the urea liquid/solid state [17]. However, a few works alternatively suppose the thermolysis to be taking place in the droplet's boundary layer, i.e. in the gas phase [11, 16].

Consensus exists that isocyanic acid is converted to ammonia in a hydrolysis with water vapor available from the UWS and the exhaust gas from the combustion process according to Equation 1.2. This reaction however is much slower than the thermolysis for typical exhaust

gas temperatures, but becomes very rapid in the presence of the SCR catalyst [6, 18].

2.1.1 Experimental Studies

Several experimental studies have been carried out to better understand the mechanisms of UWS decomposition and quantify the relevant timescales of ammonia release. Basically three types of experiments can be distinguished. The first type aims at analyzing the shrinkage of single UWS droplets by video-analysis under the variation of ambient gas conditions [19, 20]. In a second type of experiments the UWS decomposition has been studied by injecting a UWS spray into a hot (exhaust) gas flow and measuring the concentrations of its products, ammonia and isocyanic acid as a function of pipe length, i.e. spray residence time [21, 18]. The last type of experiments focuses on the principle chemical decomposition mechanisms including incomplete decomposition and deposition formation. Those studies analyze the products of UWS- or pure urea-decomposition in a heated reaction chamber by spectroscopy methods or gravimetric measurements [22, 23, 24]. Similar methods are used to determine the composition of deposits observed in engine test bench experiments [25, 9, 26].

Single UWS droplet decomposition experiments

In independent experiments Musa et al. [19] and Wang et al. [20] have analyzed the evaporation of single UWS droplets in a quiescent atmosphere at different ambient temperatures by digital video analysis. The droplet is suspended on a thin quartz glass fiber and the temperature of the evaporation chamber is maintained constant during each experiment by an electric heater. Temperatures range from, $473\,K$ to $773\,K$ [19] and $373\,K$ up to $873\,K$ [20], respectively. Figure 2.1 shows the droplet decomposition process for selected ambient temperatures in terms of the temporal evolution of the droplet diameter measured by Wang et al. [20].

The experiment by Musa et al. [19] reveals qualitatively the same trends. Both studies prove the separated two-step-decomposition of UWS. The initial stage of water evaporation follows the well known D^2-law for droplet evaporation [27]. A comparison to the evaporation of a pure water droplet proves that the water evaporation from UWS is nearly unaffected by the existence of urea within the solution until drying is nearly completed [19]. Only a slight decrease in the evaporation rate occurs due to the partial pressure reduction by urea. As shown by Birkhold et al. [14] vaporization cooling of the droplet leads to an adiabatic wet-bulb temperature [28] during water evaporation at around $340\,K$, for which the partial pressure of urea can be neglected. Once drying is reaching its final stage, the droplet temperature increases to a higher quasi-steady temperature and urea melts and decomposes. For the resulting urea decomposition stage, the D^2-law is only fulfilled at moderate ambient gas temperatures according to the data by Wang et al. [20] and Musa et al. [19]. For temperatures around $600\,K$ and above, disturbances of the second stage by micro explosions have been reported, leading to oscillating droplet diameters (see Figure 2.1, right). In consequence, the D^2-law remains only valid in a rough estimation for elevated ambient temperatures.
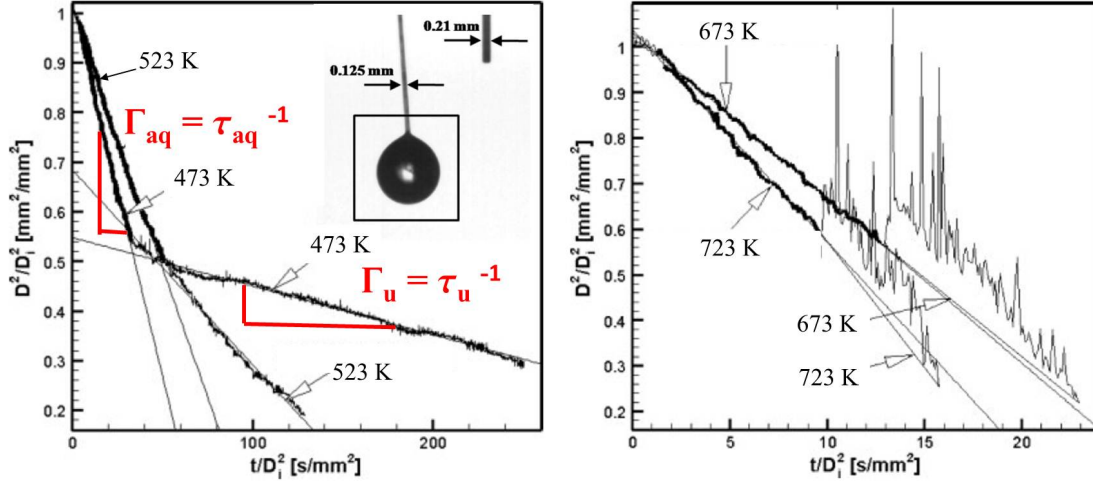
Figure 2.1: *Measured UWS droplet shrinkage in a quiescent atmosphere, for low (left) and high (right) ambient temperatures [20]*

In any case, both authors observed a crystallization of urea at the end of the second stage. The resulting solid deposit remained on the fibre for ambient temperatures below $573\,K$ but was completely evaporated at $673\,K$ or $773\,K$ and above in the experiments by Musa et al. [19] and Wang et al. [20], respectively.

Excluding the formation of depositions, the diminishing rates for water evaporation and urea thermolysis can be quantified as a function of ambient temperature from the experiments. Following the D^2-law, the diminishing rates (or characteristic time scales) can be expressed in terms of the squared diameter reduction slope (or its inverse), see Equation 2.1 [27]:

$$\tau = \Gamma^{-1} = \left(\frac{d(D^2)}{dt} \right)^{-1} = \left(\frac{d(D^2/D_0^2)}{d(t/D_0^2)} \right)^{-1} \tag{2.1}$$

Figure 2.2 shows the inverted diminishing rates, i.e. the characteristic timescales for both stages extracted from the experiments.

As can be seen from the graphs, severe differences occur in the time scales measured by Musa et al. [19] and Wang et al. [20]. The data of Musa et al. [19] shows an up to four times faster water evaporation and urea thermolysis over the complete temperature range. To base any decomposition model on the experimental data, an analysis of these discrepancies is a necessity. Several potential error sources occur:

Firstly, a distortion of the spherical droplet and heat transfer through the thin fibre into the droplet cannot be excluded [29]. Significant effects from the fibre are reported at lower gas temperatures ($490\,K$) and low droplet- to fiber-diameter ratios D_0/D_f. The impact is reduced with higher ambient temperatures ($750\,K$), as the the fibre needs more time to heat up while
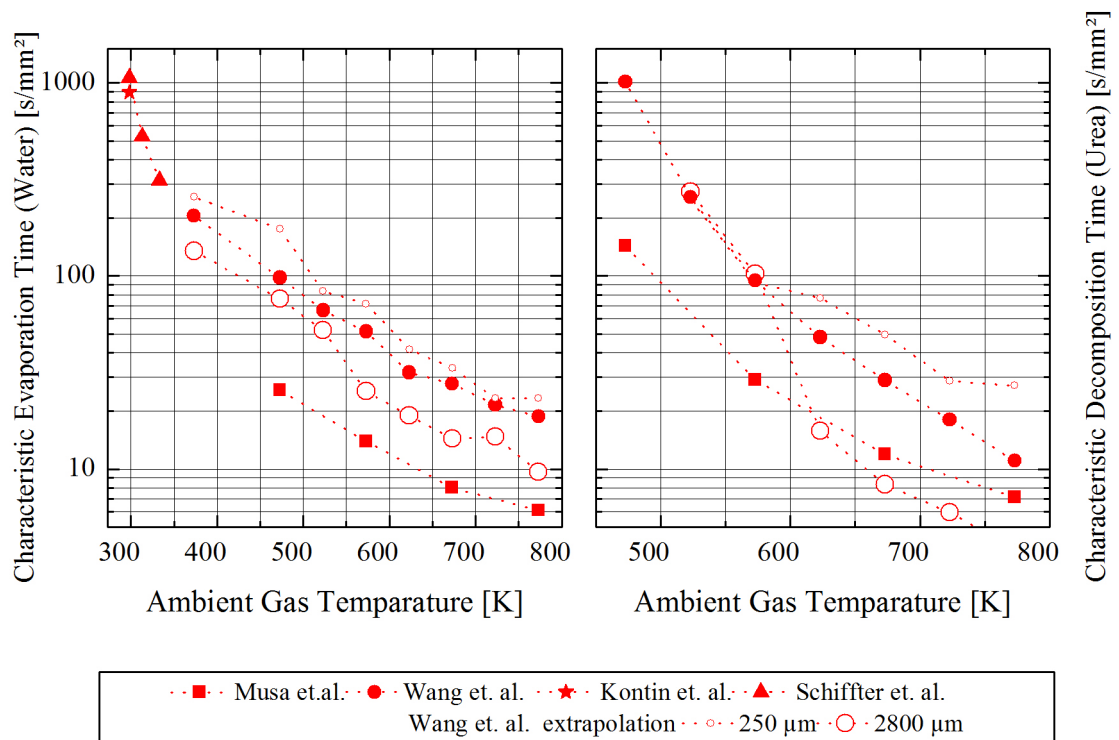
Figure 2.2: *Measured characteristic water evaporation- and urea thermolysis- timescales assuming a D^2-behaviour [19, 20], open symbols from an extrapolation of measured data by Wang et al. [20] to higher and lower initial droplet diameters*

at the same the droplet diameter diminishes faster in that case [29]. For a fiber diameter of $150\,\mu m$ and a droplet initial diameter of $1000\,\mu m$, similar to the experimental conditions of Wang et al. [20], Yang and Wong [29] report an enhancement in evaporation time around $20\,\%$ at $490\,K$ and $10\,\%$ for $750\,K$. A similar estimation of the effect holds for the data by Musa et al. [19]. Taking the findings by Yang and Wong [29] into account, the significant lower characteristic droplet diminishing times in the experiment of Musa et al. [19] cannot be blamed solely on the fiber conduction effect.

Another impact on evaporation timescales is heat transfer from the furnace to the droplet by thermal radiation. In a similar setup Yang and Wong [30] observed that at $450\,K$ the decomposition rate is nearly unaffected by radiation for an n-heptane droplet with $D_0 = 700\,\mu m$, while it enhances the evaporation by approximately $20\,\%$ at $740\,K$. Their study further proves that radiative heat absorption gradually decreases with diminishing droplet surface (initial diameter). Both observations are in agreement with radiation theory, see e.g. Abu-Ramadan et al. [31]. Wang et al. [20] report a decrease of the characteristic time scale with the droplet's initial diameter ($D_0 = 700 - 1450\,\mu m$)) for both UWS decomposition stages. Their data further

implies an increase of the effect with rising ambient temperature. The authors explain these deviations from the D^2-law with the transient nature of the multicomponent droplet evaporation process, without going into detail [20]. However, both observations indicate that it is more likely that - despite the thermal shield that is integrated by Wang et al. [20] - thermal radiation may affect the evaporation process according to the findings of Yang and Wong [30].

An extrapolation of the diminishing timescales found by Wang et al. [20], to bigger droplet initial sizes, as analyzed by Musa et al. [19] ($D_0 \approx 2600 \, \mu m$)), further underlines the possibility of radiation effects in both experiments, see additional data in Figure 2.2. The extrapolation leads to a narrowing of the characteristic evaporation times of both experiments. Still, the evaporation rate remains higher in case of the experiment by Musa et al. [19]. This may be the result of the absence of a radiative shield in their setup.

Another source of uncertainty is the assumption of a quiescent and constant temperature environment around the droplet. Wang et al. [20] state that a flow of ambient air into the evaporation chamber at the beginning of the experiment might affect the constant temperature condition. The effect is particular pronounced at higher gas temperatures in the chamber. A similar effect is very likely in the setup by Musa et al. [19]. As a consequence natural- or even forced convection might influence the concentration gradients in the droplet boundary layer, enhance the heat- and mass transfer and therefore reduce the timescales of evaporation from the droplet, see e.g. Zaitone and Tropea [32].

To estimate the relevance of those impact factors and check the reliability of the data by Wang et al. [20] and Musa et al. [19] the experiments by Kontin et al. [15] and Schiffter and Lee [33] are helpful. In their setup, the droplet is levitated in an acoustic field during evaporation and ambient conditions are carefully controlled. Effects of the acoustic field on the evaporation process are compensated by a very low airflow according to the theory of Yarin et al. [34] and the analysis of Zaitone and Tropea [32]. Droplet evaporation can be regarded as driven solely by a diffusive transport through the droplet boundary layer ($Sh = 2.0$). As a drawback, available data is limited to temperatures well below typical engine exhaust conditions ($298 \, K$ and $333 \, K$) and the water evaporation stage. Despite these limitations, the data included in Figure 2.2 indicates that the evaporation timescales determined by Wang et al. [20] match, at least at their low temperature edge, well with the trend resulting from the levitator experiments. The data by Musa et al. [19] in contrast seems to be less consistent and an underestimation of the timescales is very likely.

It has to be concluded that for the data produced by Musa et al. [19], the assumption of an isolated droplet in a quiescent atmosphere has to be regarded as questionable. This has already been noticed by Birkhold [17] and Kontin et al. [15]. For the data of Wang et al. [20] the possible impacts by radiation in the high temperature regime and fiber conduction for low temperatures has at least to be beard in mind as a possible source of error.

11

Flow reactor UWS spray decomposition experiments

Kim et al. [21] have analyzed the conversion of a UWS to ammonia and isocyanic acid by injecting a UWS spray into a straight pipe reactor and measuring product concentrations by FTIR-spectroscopy for different gas temperatures and -velocities. Spray targeting allows for a study of the decomposition process with minimized droplet-wall interaction effects. The main findings are that the thermolysis is much faster than the hydrolysis and the latter is nearly completely inhibited at gas temperatures below $573\,K$ in the gas phase. However, both reactions speed up with gas temperature. The ratio of isocyanic acid- to ammonia concentration moderately increases from one (see equimolarity in Equation 1.1) when the temperature exceeds the $623\,K$. This indicates the existence of a appreciable gas phase hydrolysis for elevated temperatures.

Very similar findings are published by Yim et al. [18], who analyzed the UWS decomposition process in a fixed-bed flow reactor. The authors also find the dominance of thermolysis over hydrolysis rate, but prove that the hydrolysis can occur without catalysation if the temperature is sufficiently high ($> 673\,K$). In addition to that, the decomposition process in the non-catalytic reactor was compared to the process in a similar layouted catalytic converter: While the thermolysis is unaffected by the presence of a catalytic coating of the pebble-bed, the hydrolysis reaction is significantly enhanced for all gas temperatures. The latter observation has also been reported by Koebel et al. [12].

Koebel and Strutz [6] have measured unprepared urea, ammonia and isocyanic acid concentration at the catalyst entrance on a Diesel engine test bench. UWS spray injection occurs $3\,m$ upstream of the SCR catalyst. Exhaust gas temperatures were varied from $528\,K$ to $713\,K$. The average residence time of droplets for the high temperature case is given to be about $90\,ms$. Even at highest exhaust temperatures, this time is not sufficient to fully decompose the UWS spray before the catalyst. $30\,\%$ of urea remain unprepared at the catalyst intake. At $528\,K$ the decomposition efficiency is even lower and $85\,\%$ of liquid urea hit the brick face. In contrast to the observations of Yim et al. [18] and Kim et al. [21], similar amounts of ammonia and isocyanic acid where found at the catalyst entrance for all temperatures, indicating a kinetic inhibition of the hydrolysis reaction.

To quantify the UWS decomposition and reaction rates from the cited experiments, several challenges occur. First, the evaporation of water occurring prior to the urea thermolysis has to be taken into account but is not experimentally captured. Second, the overall preparation speed is significantly influenced by the spray quality, i.e. the droplet size distribution. Third, uncertainties remain regarding the enhancement of preparation by droplet-wall heat transfer, which cannot be avoided completely. Therefore an extraction of correct evaporation-, thermolysis- and hydrolysis timescales can only be performed indirectly by simulating the experiment with multiphase CFD and fitting decomposition law parameters to meet the measured decomposition behaviour. An overview on those attempts from literature will be discussed in Section

2.1.2.

Incomplete decomposition experiments: deposition, polymerization

Several authors have reported the occurrence of undesired depositions in SCR-mixing systems [25, 35, 36, 10, 26]. It is commonly accepted that those solid deposits result from an incomplete thermolysis of urea from the UWS. It is further generally understood that the formation of deposits is related to insufficient thermal- and flow management within an SCR system.

Zheng et al. [10], Strots et al. [35] and Salanta et al. [36] have analyzed the formation of solid deposits under the variation of SCR system factors. They varied the system geometry (pipe bending, with and without mixing elements), UWS spray targeting, -injection rate and exhaust gas temperature, and measured the resulting deposit weight after a fixed operating time for each setup. In addition to that Strots et al. [35] have analyzed the impact of ambient temperatures down to $-3\,°C$. The authors all prove that wall wetting at low surface temperatures is a major precondition for the formation of deposits on system walls. Strots et al. [35] report a conversion of $65\,\%$ of injected urea mass to solid deposits under worst case conditions ($T_g = 473\,K$, $T_{amb} = 270\,K$, no mixing element). In contrast, less than $1\,\%$ of solid deposition was observed at temperature above $623\,K$ by Strots et al. [35] and Zheng et al. [10], for typical injection rates. However, Zheng et al. and Strots et al. further proved that deposits can be removed if the exhaust temperature is raised above $823\,K$.

All of those authors state, that intelligent spray targeting, avoiding spray cooling of system walls, insulations of pipe walls and the integration of mixing elements or wire meshes exposed to the hot exhaust gas for evaporation enhancement, can significantly reduce the risk of wall wetting and as a consequence deposition formation. Seo [26] for example identifies the injector mounting recess as a potential deposit location. By geometry modifications in this region, the recirculating flow volume and in consequence the formation of deposits was minimized.

In all cases, those phenomenological observations indicate that the formation of deposits is linked to liquid film formation as a precursor. However, Seo [26] and Zheng et al. [10] have observed that liquid urea deposits, i.e. liquid film, do not necessarily lead to crystallization or the formation of insoluble solid deposits. By contrast, the droplet evaporation studies by Wang et al. [20] prove, that liquid film is not a necessary but a sufficient condition for the formation of solid deposits, at least for large droplets. The following section therefore focuses on the chemical mechanisms that give a detailed insight in the transfer from urea to solid deposits. Details on liquid film formation due to spray wall contact will be discussed in Section 2.2.1.

Schaber et al. [22] studied the thermal decomposition of pure urea in an open reaction vessel under laboratory conditions. They analyzed the evolved gases transported from the probe by a constant sweep gas flow and the residuals in case of an incomplete decomposition as a function of linearly increasing temperature. To further understand secondary reactions, the decomposition of pure biureth and CYA was additionally studied in separate experiments. Figure 2.3 shows a schematic sketch of the major reaction scheme that has been postulated

by Schaber et al. from their findings. A number of alternative reaction routes to the desired
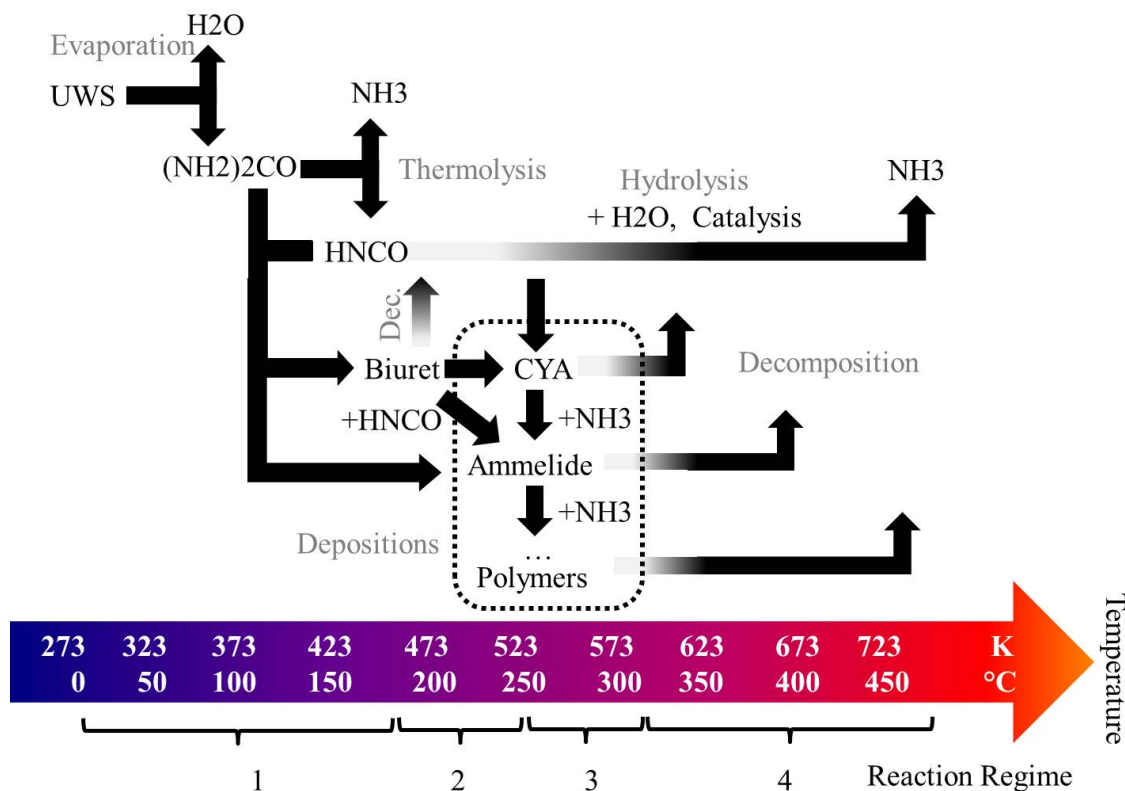
Figure 2.3: *UWS decomposition mechanism scheme including undesired deposit formation reactions proposed by Schaber et al. [22]*

urea thermolysis and hydrolysis exists. Extracting the relevance of each route as a function of temperature, Schaber et al. distinguish four reaction regions for urea decomposition, see markers in Figure 2.3. Up to $463\,K$ the process is dominated by urea thermolysis and the production of biuret. The desired primary reactions, thermolysis and hydrolysis, lead to the release of the reducing agent ammonia. Undesired reactions based on available biuret and remaining urea with isocyanic acid occur on a very low level at this stage. Between $463\,K$ and $523\,K$ biuret becomes unstable and starts to decompose again. At the same time, the undesired reactions of CYA and ammelide formation reach significant rates and compete with the biuret decomposition. Further undesired higher molecular products (ammeline, melanine) begin to form. Once the temperature exceeds $523\,K$ those solid deposits again become successively unstable and sublimate. The higher the compounds' molecular weight, the higher the onset temperature of its decomposition. A complete elimination of the solid products has been observed for temperatures above approximately $653\,K$ for CYA, $873\,K$ for ammelide and $973\,K$ for ammeline.

Lundström et al. [24] analyzed the urea reaction mechanism in a similar manner. As an ex-

tension, they compared the results from an open vessel setup, similar to Schaber et al. [22], to the ones gained from a monolith that was impregnated with UWS. The latter imitates the conditions for UWS *spray* decomposition, by providing a higher surface-to-volume ratio, which leads to enhanced heat- and mass transfer. The authors approved the validity of the *qualitative* reaction mechanism suggested by Schaber et al. [22]. However, they have shown, that the experimental conditions, i.e. vessel or impregnated monolith, significantly affect the *quantitatively* dominating paths of decomposition. In case of the cup experiment, the direct polymerization of HNCO to CYA deposits is the most probable reaction route following the thermolysis. This pathway is nearly insignificant in case of the monolith experiment, where the decomposition is dominated by the thermolysis followed by an intermediate formation and decomposition of biureth. The formation of higher molecules, like CYA is less pronounced in that case. Lundström et al. conclude that the concentration of possible reactants in the melt's surrounding is another important factor that determines the pathway of decomposition in addition to temperature. As can be seen from Figure 2.3, the formation of biureth, CYA and ammelide is directly linked to the availability of isocyanic acid (HNCO) in the ambience of the melt. As the hydrolysis reaction is not taking place at an appreciable rate in the gas phase below $400\,K$, the only HNCO sinks are either a fast transport from the melted urea surface by the sweep gas or the undesired secondary reactions. Especially in the case of the cup experiments, increased local concentrations of HNCO at the surface or even within the urea melt may be expected. In combination with an unfavorable temperature level, in the range of stage 1 and 2, this enhances the possibility of the formation of deposits in the former case.

A study that confirms the relevance of HNCO concentrations on deposit formation, has been conducted by Fang and DaCosta [23]. They analyzed the decomposition of urea powder, with and without mixing SCR active catalytic powder to the probe. Taking into account that a significant enhancement of the hydrolysis reaction is achieved by the catalysis [6], less HNCO will be available for undesired reactions in the latter case. Accordingly, the presence of the catalyst in combination with an increased sweep air humidity reduced the occurrence of undesired deposit reactions in their experiment.

Those laboratory observations indicate, why the existence of a UWS liquid film is very likely a major factor promoting the formation of undesired deposits. The conditions within the liquid film can be regarded as very similar to the ones in the cup experiment by Lundström et al. [24]. First, an unfavorable surface to volume ratio hinders the fast sweeping of decomposition products in this case. This effect is even more pronounced if deposition occurs in recirculation zones, like described for the injector mounting recess by Seo [26]. Second, wall temperatures allowing for liquid film formation, as determined by Zheng et al. [10] ($463\,K$ to $483\,K$), coincide with reaction regime 1 and 2 extracted by Schaber et al. [22]. As discussed above, this allows for the formation of biureth as a precursor and further undesired deposit reactions. Seo [26] analyzed the composition of deposits, formed from liquid film in an SCR system engine test. The TGA analysis revealed approximately $14\,\%$ of the total deposit mass to be urea, $4\,\%$ biureth, $73\,\%$ CYA and higher products as the remainder. In accordance Nishioka

et al. [25] reported CYA as the main content and urea and melamine as additional components of engine test deposits. Both studies approve the reaction mechanism proposed by Schaber et al. [22] in order to explain deposit formation in SCR systems.

2.1.2 UWS Decomposition Models

Various approaches to model the decomposition of UWS have been proposed. Basically the descriptions of the liquid-vapour mass transfer can be classified into the following types: Evaporation models that regard both stages of UWS decomposition as an vaporization process [14, 17, 37, 38, 31]. Chemical kinetics models that describe the urea decomposition in an Arrhenius type expression [39, 40, 41, 42, 43] and more sophisticated models including detailed chemistry, solidification and the internal formation of by-products [44, 15]. More simplified approaches include a heat transfer limited urea decomposition [40] or a turbulent mixing controlled mass transfer [13]. Prior to any of those phase change descriptions, the internal droplet transport has to be modelled.

Modeling Internal Droplet Transport

Theoretically, heat- and mass transfer within the droplet affects the species concentrations and temperature in the droplets boundary region and therefore the time scales of the decomposition process, see e.g. [17, 31]. As water evaporates at a higher rate than urea decomposes, an increased relative urea concentration at the droplets surface is promoted during decomposition. Internal transport mechanisms counteract against this concentration gradient across the droplets radius.

Three approaches are common in literature to model the urea concentration and temperature distribution in a spherical UWS droplet [17]. The Rapid Mixing Model (RM) postulates infinite diffusion rates for the components' concentrations and the temperature within the liquid. As a consequence no spatial distribution of those quantities is present in the droplet in this approach, i.e. urea mass fraction and temperature is uniformly distributed and homogenized at an infinite rate. The decomposition timescales are therefore determined by the concentration gradients across the liquid-gaseous surface boundary and the partial pressures of urea and water resulting from the space averaged droplet composition. At the other extreme, the Diffusion Limit Model (DL) assumes that internal water-, urea- and heat-transport is exclusively driven by diffusion processes. Depending on the timescales of internal mixing, relative to the ones of mass transfer at the surface, elevated urea concentrations at the droplet boundary and trapping of water within the droplet may arise. This in consequence decreases the partial pressure of water, hinders the evaporation of the more volatile water component and therefore the overall droplet depletion rate. The Effective Diffusion Model (ED) lies between the two extreme cases of RM and DL regarding the mixing timescale. The model considers, in addition to diffusion, internal convection forced by an external flow.

Birkhold analyzed the dependency of the UWS droplet evaporation rate on the internal transport model (RM, DL, ED). The author reports a systematically increased urea concentration at the droplet surface for the ED and DL model.

Nevertheless, Birkhold reports that the water evaporation rate is nearly unaffected by the choice of model, even for extremly fast evaporation conditions, i.e. high external temperatures and relative droplet velocities. This result correlates with the experimental observation by Musa et al. [19] that the water evaporation from UWS is very similar to the one of pure water. For these reasons Birkhold suggested that the RM is sufficient to describe the UWS droplet decomposition with a reasonable degree of accuracy. However, Birkhold only analyzed the effects of the internal transport model on water evaporation and not on the transition to the urea decomposition stage.

Abu-Ramadan et al. calculated the *complete* depletion of single UWS droplets with the RM and DL model [31]. Basically the authors come to the same conclusion as Birkhold [17], considering the RM as a suitable model for the UWS decomposition in SCR system design studies. They prove that the underestimation of the overall droplet decomposition time is lower than $10\,\%$ for the RM in comparison to the DL model in case of a $70\,\mu m$ droplet at $573\,K$. It is further decreasing with the initial droplet diameter and with increasing ambient gas temperature. This has been regarded as a reasonable degree of accuracy, taking the computational effort into account, that arises from an internal description of each single droplet of a complete UWS spray.

Nevertheless, the detailed study by Abu-Ramadan et al. with the more complex DL model has given some additional insight in the depletion mechanisms of UWS. It especially allows for the explanation of the secondary effects during decomposition, observed by Wang et al. [20] and Musa et al. [19]: Wang et al. [20] suggested that the observed diameter fluctuations during the second stage of UWS decomposition, see Figure 2.1, right, can be explained by the sudden gasification of entrapped water in the droplet's center. In contrast to this postulation, Abu-Ramadan et al. found with the DL model that hardly any water remains after a short transitional internal gasification stage and a pure urea droplet remains in the second stage. Based on this finding, the authors explain the rapid droplet diameter fluctuations by the intermediate formation of a solid crust and an internal pressure build up due to *urea-* (not water-) vaporization. Once the internal pressure exceeds the surface tension of the solid crust, it cracks, gaseous ammonia and isocynaic acid is released, the droplet size instantaneously decreases and the process starts over. Abu-Ramadan et al. explain this solidification at the droplets surface by the formation of biureth, CYA and finally ammelide and ameline in accordance to the reaction mechanism of Schaber et al. [22]. The DL model results indicate that the ideal conditions for the formation of those species in the droplet boundary layer are present: A quiescent ambient air, i.e. slow HNCO transport, high urea concentrations and an adequate temperature level support the formation of the solid crust. Also the remainder of solid deposits up to $673\,K$ and $773\,K$, observed by Musa et al. [19] and Wang et al. [20] respectively, can be explained by the chemical decomposition mechanism by Schaber et al. [22] in combination with the DL model [31].

It is worth to emphasize, that the droplets in the cited experiments are one to two orders of magnitude bigger than for a typical UWS spray in automotive applications (SMD around $50 - 100 \, \mu m$). A much smaller initial diameter leads to much shorter absolute droplet lifetimes in the application case. Moreover, isocyanic acid is very likely swept away faster from the droplets surface. The effects of crust formation and diameter fluctuations are therefore expected to be less pronounced in the application case. As Birkhold [17] already pointed out, the formation of deposits within *droplets* of an application type UWS spray is very unlikely.

Despite those detailed insights, most authors have based the UWS depletion on the RM model, following the pragmatic suggestion by Birkhold and Abu-Ramadan et al.. If not stated otherwise this is the case for the following model descriptions.

Evaporation Model for UWS Droplet Mass Transfer

An established approach to simulate the mass transfer from UWS to its gaseous reaction products is the evaporation model, first proposed by Jeong et al. [45] and Birkhold et al. [39]. The basic idea is to model the vaporization of water and the decomposition of urea as an evaporation process. Assuming equilibrium conditions in the near droplet boundary layer, the mass transfer of each component from the UWS droplet is determined by the partial pressures p_i^s of its components i (water and urea) at the surface, see Equation 2.2 [17, 16, 31, 46].

$$\frac{dm_{d,i}}{dt} = -\pi D_d \Gamma_{i,g}^s Sh \rho_g^s \frac{\nu_i M_i}{\sum_{j=1}^n \nu_j M_j} \ln \left[\frac{\nu_i p_g - p_i^\infty}{\nu_i p_g - p_i^s} \right] \tag{2.2}$$

For the determination of the Sherwood number Sh, see corresponding works, e.g. [17, 16, 31, 46]. A major point with respect to UWS evaporation models is, that different approaches have been proposed to determine the partial pressures of urea and water from the current composition of the UWS droplet and the vapor pressures of the pure components.

The most simplified approach has been used by Zheng et al. [47]. They model pure water instead of UWS and consider water vaporization only. It is obvious that this can be regarded only as a very crude approximation to describe UWS behaviour. Jeong et al. [45] have used an emulsified mixture approach, meaning the two components do not influence each other during their vaporization.

Several authors use Raoult's law to determine the partial pressures of water during the first stage of UWS decomposition, assuming an ideal mixture [41, 42, 43], i.e.:

$$p_i^s(T_d) = x_i^l \cdot p_i^0(T_d) \tag{2.3}$$

Birkhold, Ström et al. and Lundström et al. use a correlation by Perman and Lovett [48] for the partial pressure of water in UWS, which is very close to the ideal mixture assumption [17, 40, 37].Ebrahimian et al. [49] determine the partial pressure of water taking into account the non-ideality of the UWS mixture. However, these authors prevent urea from decomposing before water is completely evaporated from the droplet, assuming a well defined distinction

between the two depletion stages. The second stage is modelled as a pure urea evaporation in case of Birkhold et al. and Lundström et al. [39, 17, 37]. The remaining authors use an alternative model instead of the evaporation approach for the urea decomposition stage, see subsections below.

Evaporation models that do not make any assumption about the droplet water content for the onset of urea decomposition have been proposed by Bhattacharjee and Haworth [38] and Abu-Ramadan et al. [31]. They use Raoult's law throughout the whole decomposition process for both, water and urea.

While consistency exists throughout literature regarding the water vapor pressure description, very different saturation pressure curves have been proposed for urea, see Figure 2.4.
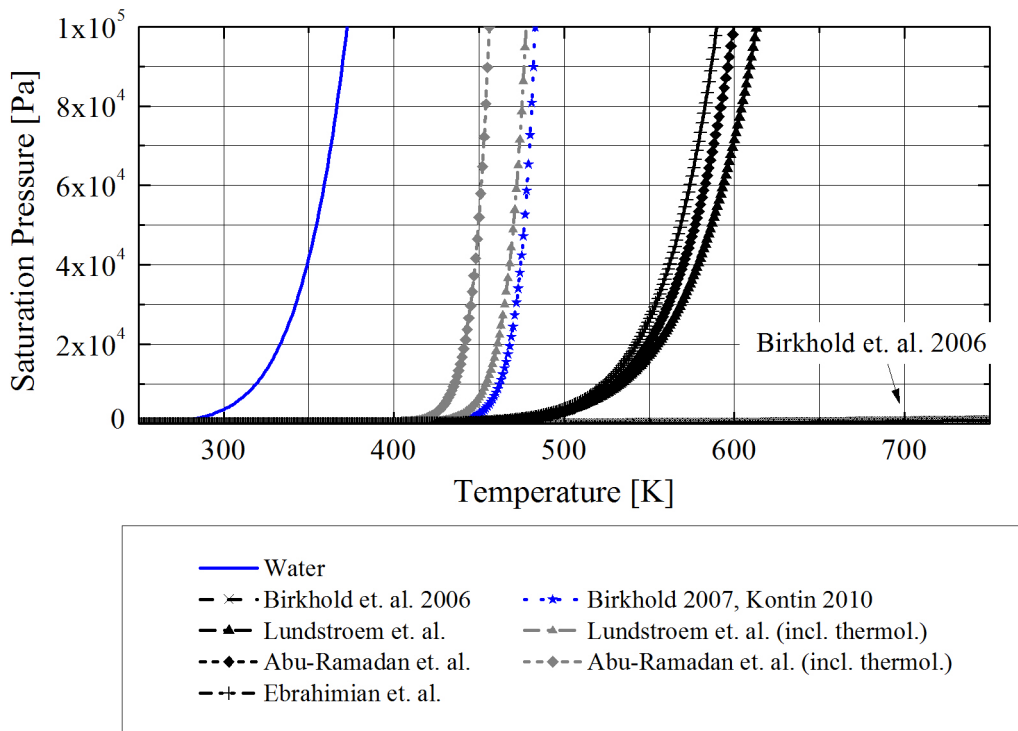
Figure 2.4: *Saturation pressure curves proposed for the decomposition description of urea [39, 17, 44, 37, 31, 49]*

Birkhold has proposed two correlations that significantly differ. The first one is determined from CFD-simulations of the experiments by Kim et al. [21, 39]. As an alternative, Birkhold measured the standard melting- and boiling point of pure urea and fitted an exponential function to determine the saturation pressure curve [17]. The latter correlation has also been used by Kontin et al. [44, 15]. Lundström et al. and Abu-Ramadan et al. derived the vapour pressure above liquid urea theoretically using the Clausius-Clapeyron equation [37, 11, 31].

Ebrahimian et al. employs the sublimation pressure curve rather than a vapor pressure curve, based on the DIPPR database [49, 52].

Generally, each of the proposed urea vapor pressure curves has a reasonable justification. However, as the range of the curves in Figure 2.4 indicates, there is a strong uncertainty regarding an adequate description. The model *first proposed* by Birkhold et al. [39] is very likely the most unrealistic description. The procedure of fitting the urea pressure curve to UWS spray decomposition data is related to a high degree of uncertainties, as already discussed. The curves derived from first principles [37, 11, 31], as well as the database curve by Ebrahimian et al., lie quite near to each other. However, they propose a relatively high boiling point of urea in comparison to the *second proposal*, i.e the measured one, by Birkhold [17].

The major reason for these differences is the following: Lundström et al. and Abu-Ramadan et al. do not (necessarily) assume the decomposition process from liquid urea to ammonia and isocyanic acid as one single step. Calculating the saturation pressure curve, both authors regard the evaporation ($h_{vap}^{urea,l} \approx 1.46 \, kJ/kg$ [31, 16]) as one step happening in the droplets boundary layer, but the thermolysis of gaseous urea ($h_{therm}^{urea,g} \approx 1.63 \, kJ/kg$ [31, 17]) as a separated step occurring outside this layer. They therefore neglect the thermolysis enthalpy in the Clausius-Clapeyron equation, which induces a less steep saturation pressure curve of urea. As an alternative, Lundström et al. take the combined evaporation-and-thermolysis-approach into account. However, though integrating the thermolysis enthalpy into the droplet heat balance, they do not modify the vapor pressure curve accordingly, which has to be regarded as inconsistent. For a comparison, Figure 2.4 includes the saturation pressure curves, if one took the thermolysis enthalpy into account ($h_{therm}^{urea,l} \approx 3.09 \, kJ/kg$) in the derivations of Abu-Ramadan et al. and Lundström et al.. As can be seen from the graphs, this leads to a narrowing of the models proposed by Abu-Ramadan et al., Lundström et al. and Birkhold.

Birkhold has noticed that no experimental evidence for stable gaseous urea, providing the two-step approach, has so far been published [17, 22]. In contrast, Abu-Ramadan et al. have argued that Birkhold [17] overestimates the saturation pressure in comparison to measurements by Emelyanenko et al. [53]. Indeed, due to the interdependency with the thermolytic decomposition and secondary chemical reactions, the phase change and especially the onset of boiling may be very difficult to define for urea. This may be regarded as an error source in the approach by Birkhold [17].

The majority of the described evaporation models can be or have been evaluated by a comparison of simulation results to the experiments by Wang et al. [20] or Musa et al. [19]. A discussion of the results will be given, together with a validation of the decomposition model of the present work, in Section 5.2.

Chemical kinectics Arrhenius-model

The second group of decomposing models, proposed in literature, pays pronounced respect to the chemical nature of the urea thermolysis process. Common to all of those models is an

evaporation approach for water, as discussed in the previous section, but an Arrhenius type expression (see Equation 2.4) for the mass transfer due to urea decomposition. If not noted otherwise, the evaporation and thermolysis is again regarded as one single combined step by the following authors.

$$\frac{dm_{d,urea}}{dt} = -\pi \left(D_d\right)^n A_{th} \exp\left[\frac{-E_{th}}{RT_d^s}\right] \tag{2.4}$$

A principal difference arises from whether the reaction is regarded as concentration-, volume- or surface based. Yi [41] use a classic single step Arrhenius model. No direct dependency of mass transfer on the droplet size is postulated, i.e. the droplet diameter exponent in Equation 2.4 is zero ($n = 0$). Birkhold et al. [14] has proposed an extended Arrhenius approach with a first order dependency on the droplet diameter ($n = 1$). This is in accordance with the evaporation model assumption, see Equation 2.2. Munnannur and Liu [42] postulated a volume based single kinetic reaction rate expression, i.e. $n = 3$, based on a concept originally developed for for pulverized coal particles. Those authors prevent urea from decomposing, until water is fully evaporated. In contrast, Abu-Ramadan et al. [31] allow urea to decompose before complete drying and account for the remaining water content at the droplets surface in the urea mass transfer rate expression $Y_{urea} \leq 1$. In addition to the evaporation approach discussed previously, the authors also analyzed the Arrhenius type model. They considered both, a volume based mass transfer ($n = 3$) and surface reaction based decomposition ($n = 2$) [31].

Beside those principal differences, the particular implementations differ by the proposed kinetic parameter sets for the activation energy E_{th} and the frequency factor A_{th}, and the source for determining them. In any case, the factors are based on flow reactor UWS spray decomposition experiments, as explained in Section 2.1.1. Common to all those proposals are therefore the uncertainties that have previously discussed for flow reactor experiments.

In this context Abu-Ramadan et al. [31] conclude from a single droplet evaporation study that modelling urea depletion as a vaporization process is superior to the Arrhenius type approach. The same has been stated by Birkhold [17]. As a main argument against the Arrhenius type model, both authors advert to the uncertainties that arise from the determination of the Arrhenius parameters from flow reactor experiments. Despite this insecurity, any non-linear droplet diameter dependency ($n \neq 1$) in the Arrhenius approach has in any case to be regarded as insufficient to describe the surface related mass transfer.

Models including Crystallization and Undesired Reactions

It is well known that urea has a limited solubility in water. Commercially available UWS for automotive application therefore contains only $32.5\,\%$ of mass urea, to avoid crystallization at regular storage conditions. Though the amount of urea soluble in water is increasing with temperature, an oversaturated status may be reached during the preparation of UWS in the

exhaust system.

A numerically efficient approach to consider a possible formation of a solid urea crust at the UWS droplet surface has been proposed by Kontin et al. [44]. The authors have extended the evaporation model proposed by Birkhold [17]. They account for the effect of urea crystallization on the water evaporation rate by the introduction of an empirical mass transfer reduction coefficient. The modification becomes only relevant if urea reaches an oversaturated concentration within the UWS mixture. The empirical coefficient was adopted to match the results from the accoustic levitator experiments, see Section 2.1.1 [44]. The model adoption has so far only been undertaken for room temperature. The urea decomposition stage was not modified and left as proposed by Birkhold [17]. Therefore urea thermolysis sets in, once water is fully evaporated and remains unaffected by the crust model.

Kontin et al. analyzed the impact of the model extension on the predicted UWS preparation time in a numerical sensitivity study. A single UWS droplet evaporation process in quiescent ambience was calculated for different ambient gas temperatures (from $473\,K$ to $873\,K$). Results from the extended model were compared to the basic evaporation model without crust formation. The study proved that an oversaturated state is only reached, and the model extension becomes relevant, at the end of the water evaporation stage. As a consequence of the crust, the evaporation of the remaining water is successively slowing down. This leads to a delay for the onset of the urea decomposition, which is - by definition - then again unchanged by the crust model. The overall effect of the crust on the total droplet lifetime is less than $2\,\%$. The rates determined for both D^2- stages remain unaffected in a very good approximation.

It is worth emphasizing that this urea crust formation is a purely *physical* phenomenon and is not related to the formation of solid deposits from undesired *chemical* urea reactions. As pointed out by Abu-Ramadan et al. [31] the possible urea crust formation due to oversaturation is *not* responsible for the droplet diameter fluctuations observed by Wang et al. [20], during the urea thermolysis stage. This is in agreement with not considering crust effects in this stage in the model by Kontin et al. [44]. The idea is reasonable, as the droplet temperature exceeds the urea melting temperature once water is fully released.

A model that considers the *chemical* formation of by-products during urea decomposition has been developed by Ebrahimian et al. [49]. The physical impact of solved urea on the evaporation of water was considered in the first stage model, see section on evaporation models. To model the urea decomposition stage, the authors proposed a detailed chemical reaction mechanism according to the findings by Schaber et al. [22] and Lundström et al. [37]. All major alternative reactions and the thermolysis reaction were taken into account. Chemical kinetic parameters were fitted to the experimental data available from urea-, biureth- and CYA- decomposition experiments. The authors proved a very good agreement between the tuned model and measured off gas concentrations from several different experiments with one single parameter set. On this basis, the model allows for a detailed insight into the main and alternative routes during urea decomposition and approves the proposals by Lundström et al. [37]. It for example predicts the formation of solid depositions and explains the differences

between the cup and the monolith experiments by Lundström et al. [37], see section on incomplete decomposition experiments.

The mechanism has been implemented in a commercial chemical kinetics code and coupled to a commercial CFD-code. However, the authors do not report any information on the computational effort resulting from the chemical kinetics solver. Though the model gives a detailed insight and approves the experimental findings on alternative decomposition routes, its practical value for the development of SCR-systems depends severely on this factor.

Droplet-Gas Heat Transfer

Unlike the choice of mass transfer description, heat transfer between the UWS droplet and the ambient air / exhaust gas is modelled by a standard heat transfer description in all of the cited studies, see Equation 2.5:

$$\frac{dQ_d}{dt} = \pi D_d^2 \cdot h \cdot (T_d - T_g) \tag{2.5}$$

In case of the ED or DL model T_d is equal to the droplet surface temperature, otherwise it corresponds to the average droplet temperature. The heat transfer coefficient h is in all cases related to the gas phase heat conductivity and the Nusselt-number Nu, see e.g [55]:

$$h = \frac{\alpha_g Nu}{D_d} \tag{2.6}$$

An extended version, based on the formulation by Wakil et al. [56], accounts for the effect of mass transfer on the heat transfer coefficient by a correction factor $Z(\dot{m}_d)$. In this case h reads:

$$h = \frac{\alpha_g Nu}{D_d} \frac{Z}{e^Z - 1} \qquad \text{with} \qquad Z = \frac{-c_p \dot{m}_d}{\pi D_d \alpha_g Nu} \tag{2.7}$$

The latter is implemented in Star-CD, used in the study at hand, see [46] for details.

2.2 UWS Spray Interaction with SCR System Walls and Exhaust Gas

Once a UWS spray is injected into the SCR system, its dynamics are affected by the turbulent exhaust gas flow, which determines the location of ammonia source terms. In addition, the interaction of the UWS spray with exhaust system wall is generally unavoidable due to packaging limitations and affects the SCR performance. On the one hand, thermal droplet-wall contact may enhance the UWS preparation process due to increased heat transfer from the hot solid surface to the liquid droplet. Spray wall impact may further lead to a break-up of droplets, which results in a better surface to volume ratio after impingement and therefore enhances the evaporation rate [39]. Spraying on a mixing element, integrated to the SCR

system and exposed to the exhaust gas flow, has therefore become a state-of-the-art technical solution, not only to enhance turbulent mixing of ammonia, but also to speed up the evaporation of UWS. On the other hand, especially at low exhaust temperatures, the formation of an intermediate or persistent liquid film has been observed that may lead to solid deposits.

2.2.1 Theory and Lagrangian Model

Dynamics of Droplet-Wall-Interaction

A number of multi-regime impingement models for a Lagrangian framework that cover a droplet's behavior during wall impact have been developed and implemented in commercial CFD codes, e.g. [57, 58, 59]. All of those models are based on the reduction of the phase space of regime-determining parameters (e.g. droplet diameter, impact velocity, -angle, liquid properties, wall temperature and -roughness, etc.) by the introduction of (dimensionless) characteristic numbers. Based on the determined regime for an impinging droplet, secondary droplet properties are then assigned according to measurement-based correlations.

In the CFD code Star-CD, used in the study at hand, the Bai-Model is available as a typical multi-regime impingement model [60]. A schematic overview of the regimes is given in Figure 2.5. Relevant characteristic numbers to distinguish between different impingement regimes are the wall temperature T_W and the dimensionless droplet Weber- and Laplace- number. The former is evaluated relative to a Rebound Temperature T_s^* and the Sliding Temperature T_L^* to determine the predominant impingement regime. Those regime limits are linked to the Boiling Temperature T_{sat} and the Leidenfrost Temperature T_L respectively by an empirical direct proportionality factor, see Equations 2.8:

$$T_s^* = B_s^* \cdot T_{sat} \tag{2.8}$$
$$T_L^* = B_L^* \cdot T_L \tag{2.9}$$

In order to distinguish between regimes, depending on the droplets stability, the dimensionless droplet Weber- and Laplace number are employed. Two critical Weber-numbers are defined that in turn depend on the droplet Laplace number occur, see Equation 2.10:

$$We_s = A_w \cdot La^{-0.18} \tag{2.10}$$
$$We_a = A(r_s) \cdot La^{-0.18} \tag{2.11}$$

We_s is valid for wetted walls (liquid film present), We_a for dry walls. Again, two empirical constants $A(r_s)$, which are correlated to the wall's surface roughness r_s, and A_w occur. For high wall temperatures two additional stability regime limits We_1 and We_2 are present. Those numbers are regarded as constants.
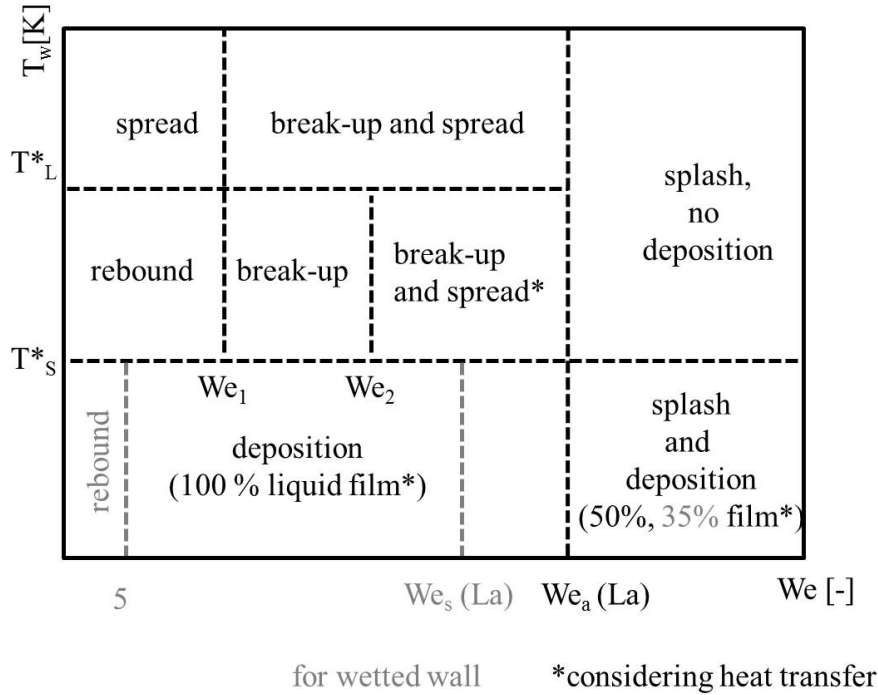
Figure 2.5:   *Regime distribution for a droplet with Weber-number We and Laplace number La impinging a solid wall of temperature T_w according to Bai and Gosman [58, 46]*

The major regimes, separated by those characteristic numbers, are as follows: At low temperatures ($T < T_s^*$) a deposition / liquid film formation- and a droplet splashing regime are distinguished, depending on droplet stability. Above T_s^*, no liquid film is formed, considering the instant formation of an insulating vapor film (Leidenfrost effect). In addition to splash, thermal break-up regimes with rebounding droplets or droplets sliding along the wall are distinguished. For the particular distribution, see Figure 2.5, for further details [58, 46].

In an analogous manner the modelling frameworks proposed by Stanton and Rutland [61, 59] and Kuhnke [57] account for droplet deposition, droplet break-up, -rebound and -splash. Despite some deviations in the particular characteristic number formulation and secondary droplet correlations, all of those alternative multi-regime models, employs the same regime transition criteria measures (wall temperature, droplet stability, presence of liquid film) and a similar regime distribution.

The major point with respect to the CFD-simulation of SCR systems is that the exhaust gas conditions (temperature, mass flow) cover a range such that nearly any impingement regime from massive wall wetting to the Leidenfrost phenomenon may occur during operation, see also Figure 1.4. As a consequence any multi-regime impingement model that claims to be

predictive, may require an adaptation of the impingement regime limits in the whole regime phase space. The latter depend on the solid-liquid combination and all of the available models have - in their original formulations - been validated and parameterized for gasoline or Diesel spray injection purposes. For the Bai-model application to SCR-systems all regime boundary numbers ($We_a, We_s, B_s^*, B_L^*, We_1$ and We_2) have therefore to be adapted for the pairing of UWS and stainless steel. To cope with this challenge a sound experimental data base and validation is unavoidable.

Liquid Film Dynamics

The major physical impact factors on a UWS liquid film that is formed in the exhaust system are shown in Figure 2.6 [59].
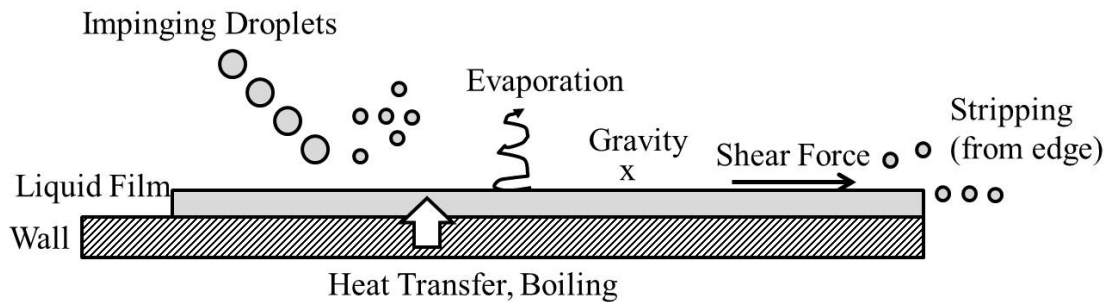
Figure 2.6:   *Major physical phenomena determining liquid film dynamics, according to [59]*

Keeping evaporation out of consideration until later, the dynamic behavior is generally determined by shear- and gravimetric forces. Additional momentum- (and mass- and heat-) transfer occurs during spray impingement. All models available in literature and implemented in CFD codes captures those impacts [60, 59, 46, 62, 63] in an analogous manner. A common assumption is that the film is thin enough to maintain the boundary layer approximation, see e.g. [46]. Nevertheless, effects of shear induced film surface roughness on the turbulent boundary layer are taken into account, see e.g. [17]. Moreover, the internal velocity profile across film thickness is assumed to be laminar (i.e. parabolic) and the temperature profile piecewise linear [46]. Conservation equations for liquid film mass, -momentum and -energy are formulated on a two dimensional grid by integrating film across the film thickness for any wetted surface cell. Therefore, all conservation equations are reduced to a two-dimensional formulation of the film attached to the wall.

In addition to this basic transport description, additional submodels include the effect of contact angle on the film movement and stripping effects [46, 64, 65]. The former mimics the typical stick-and-slip movement, resulting from the temporal cumulation and sudden

relaxation of liquid on the leading/upstream edge of the film. The latter describes the re-entrainment of liquid from the film into the flow in form of droplets. Mechanisms leading to this film stripping can be divided into shear induced surface instabilities [65] and film break-up on sharp edges [64, 46]. The relevance of those effects in particular and of liquid film dynamics in general for SCR systems (and its simulation) is as yet unclarified.

Thermal Contact between Liquid Film and Solid Walls

Thermal liquid-solid contact has to be modelled to simulate impinging droplets' and liquid film's evaporation behavior. A challenging point is a non-linear dependency on boundary conditions, especially on wall temperature. Moreover, for thin liquid films ($O(d) \simeq 10\,\mu m$) and surface temperatures beyond the boiling temperature of the liquid, as they typically occur in SCR systems, limited knowledge on the details of thermal contact is available.

The most promising approach to nevertheless describe the thermal contact of a thin liquid film with hot walls is based on the Nukiyama pool boiling correlation [66], see Figure 2.7. The latter has originally been observed for liquids filling a deep vessel with a heated bottom or thin heated fibres surrounded by a liquid. The graph shows the heat flux from solid to liquid as a function of the wall's excess temperature, defined as the difference between wall surface temperature and the liquid saturation temperature. Based on this measure, a distinction between different boiling regimes is undertaken [66]. The images in the lower part of Figure 2.7 give an impression of the physical mechanism underlying the heat transfer process in the different regimes [68]. Below the saturation temperature, natural convection dominates the internal heat transfer. At low excess temperatures, vapor bubbles are formed in the near wall region, which support the heat transport within the liquid (nucleate boiling regime). With increasing excess temperature the vapor bubbles merge to slugs and columns, further supporting heat transfer, until a maximum value of heat flux (critical heat flux) is reached at T_{CHF}. At even higher temperatures the local boiling spots collapse to a vapour film now increasing at the interface between fluid and solid (transition boiling). This reduces the heat transfer. Finally, a continuous insulating vapour cushion is formed between wall and liquid which reduces the heat flux to a local minimum at T_L (Leidenfrost phenomenon). Beyond this point, heat flux is more and more dominated by thermal radiation through the gaseous cushion and is therefore only increasing at a small gradient with rising surface temperature (film boiling).

It is worth emphasizing that the Leidenfrost temperature as defined in the Nukiyama curve is a reasonable criterion to distinguish between wall wetting (i.e. deposition) and non-wetting regimes for liquid attached to the wall. However, if the process becomes dynamic, like for impinging droplets, the value of T_L will not necessarily coincide with the critical deposition limit temperature (which is the sliding temperature T_s^* in case of the Bai-model). This will be discussed in the next subsection.

For each boiling regime, empirical correlations between the excess temperature and the resulting heat flux have been established [66]. The qualitative characteristics of the depicted
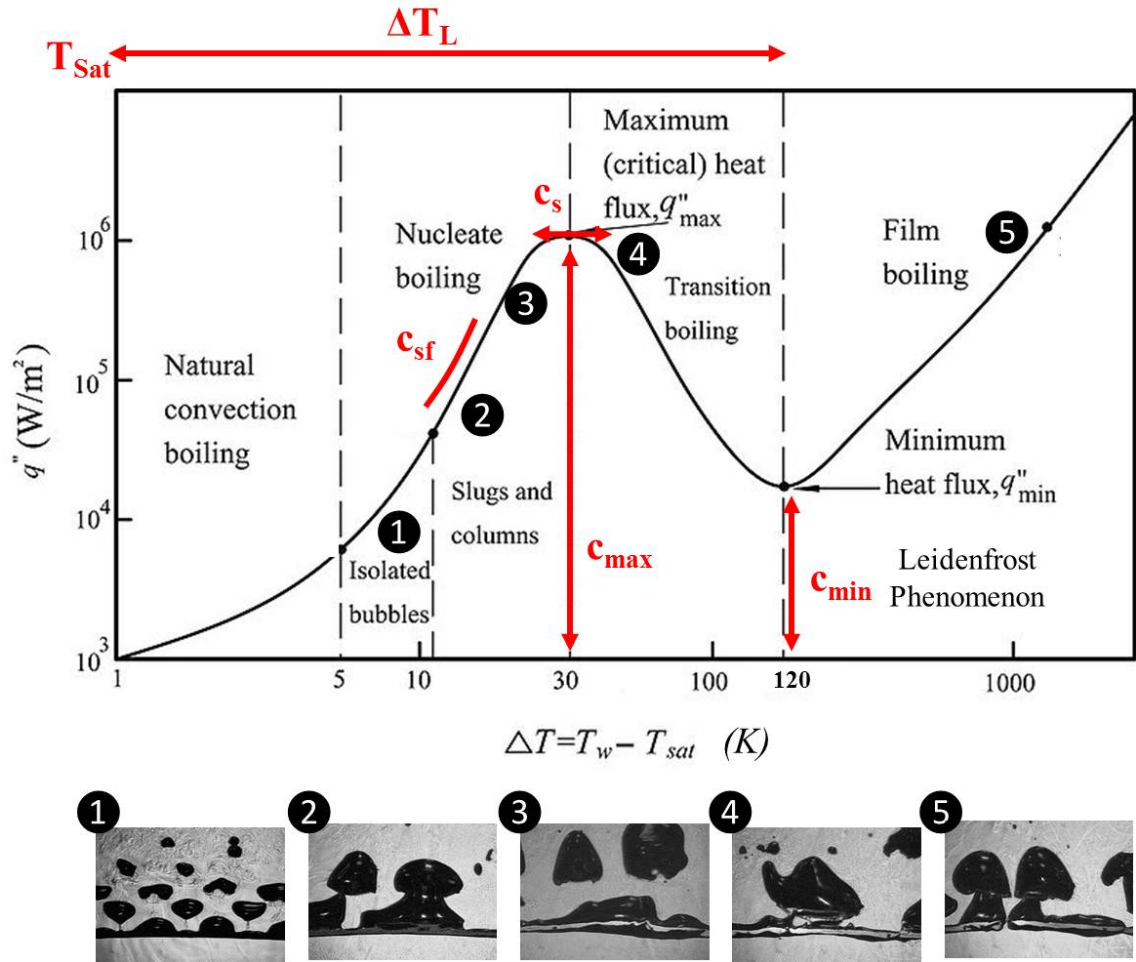
Figure 2.7:   *Solid-Liquid heat transfer as a function of surface excess temperature according to the Nukiyama-pool boiling model (upper picture [67]) and underlying heat transfer mechanisms (lower picture series [68])*

Nukiyama curve in Figure 2.7 are valid for any pure liquid. However, its quantitative development can vary significantly, depending on the liquid and wall properties. Impact factors include the liquid viscosity, surface tension, density, specific heat, heat of vaporization and Prandtl number and the solid surface roughness [66]. Those dependencies are covered intrinsically by the general heat transfer correlations. As a consequence for binary mixtures, like UWS, the Nukiyama curve becomes concentration dependent via the concentration dependency of fluid properties. Most obvious, due to the variable saturation temperature of a binary liquid (see Section 5.1, Figure 5.1) the root point of the Nukiyama curve becomes a function of the liquid composition. According to experimental findings (e.g. [69, 70]), Yagov [71] derived theoretically, the critical heat flux of a binary mixture may be either higher or lower than the corresponding values of its pure components, depending on the particular mass fractions.

Additional dependencies of the Nukiyama curve on the geometric setup have been observed empirically. Relevant parameters include the heater or vessel size [72, 73] and the direction and strength of gravity [66, 72]. This is of particular interest for the applicability of the model to arbitrary located thin liquid films in the exhaust system. In order to capture those effects, the Nukiyama curve has been parameterized by empirical constants in addition to its intrinsic dependencies on fluid properties, see red tuning constants in Figure 2.7 [46].

An implementation of the Nukiyama pool boiling model according to White [66] is available in Star-CD [46]. As the previous description indicated, a successful application of the model to UWS, relies on a sound fluid property database for both urea and water and a reasonable adaption of the empirical parameters ($c_{max}, c_{min}, c_s, c_{sf}, \Delta T_L$). To date, an adaptation to thin UWS liquid films cannot be found in literature.

Thermal Contact between Impinging Droplets and Solid Walls

Thermal contact between impinging droplets and hot walls is further complicated by the interdependency with the kinetic aspect of the process. Below the Leidenfrost temperature the heat flux according to Nukiyama can be regarded as a reasonable approximation for impinging droplets [17]. However, even beyond the Leidenfrost temperature, droplet dynamics may result in a direct thermal liquid-wall contact at the early stage of impingement, as the formation of the insulating vapour cushion sets in with a delay (boiling retardation), see e.g. [74]. According to Pischinger [75] and Wruck [76] the heat flux density during this early stage of direct thermal contact, is several orders of magnitudes higher than proposed by the Nukiyama curve, i.e. after the vapor film has formed.

An elaborate heat transfer model has been proposed and implemented in the CFD simulation tool FIRE by Birkhold [17, 63]. Based on the works by Wruck [76] and Meingast [78], the author employs a one dimensional thermal contact model between impinging droplets and walls for wall temperatures beyond the Leidenfrost value. The description leads to an increased heat flux to impinging droplets during the direct contact phase. After this phase, heat flux is set to zero, mimicking the following insulating vapor film. For regimes below the Leidenfrost temperature, i.e. wall wetting droplets, Birkhold utilizes the Nukiyama curve for pure water to describe the heat transfer. This has to be regarded as a simplification, considering the dependency of the Nukiyama curve on the liquid's composition.

The total transferred heat for an impinging droplet is calculated from the heat flux density, transferred during direct thermal contact time and on an effective contact area. Thermal contact time is defined as the minimum of the dynamic contact time proposed by Wruck [76] and the additionally introduced, physically motivated parameter, boiling retardation time (see discussion above). The effective contact area results from droplet deformation from a spherical to a more cylindrical shape during impingement. For the maximum spreading diameter, determining the effective thermal contact area, numerous correlations have been proposed.

Birkhold utilizes the one by Akao et al. [79].

An alternative, more simplified, thermal contact model has been implemented in Star-CD, based on the method by Eckhause and Reitz [80]. For any droplet that leaves the wall immediately after impingement, i.e. any non-sliding or non-sticking droplet, see regime distribution in Figure 2.5, the model regards thermal contact time as zero. For temperatures beyond T_L, even droplets that are sliding along the wall are regarded to have no thermal contact with the wall. In this case the underlying assumption is an immediate formation of a perfectly insulating vapor film [46].

Thermal contact between liquid and solid is in this formulation only taken into account in two cases (provided the liquid film and Nukiyama pool boiling model are active), see markers in Figure 2.5. First, liquid film is formed at wall temperatures below the sliding temperature T_s^*. The thermal contact is then described by the Nukiyama curve, as discussed in the previous section. Second, the impinging droplet is within the 'break-up and spread-regime' and the wall temperature between T_s^* and T_L^*. In this case, boiling- like heat transfer is considered employing the Rohsenow correlation [81], similar to the nucleate boiling regime in the Nukiyama model. For thermal contact time with the wall, the residential time of the sliding droplet at the corresponding solid cell is taken. It is therefore resulting from the sliding velocity of the droplet. Droplet deformation during impingement is calculated by a similar We-number dependency as proposed by Akao et al.[79, 46].

2.2.2 UWS-Impingement and Liquid Film Experiments

Some experimental investigations in literature provide an insight into the impingement of single UWS droplets or -sprays and wall film formation on SCR system walls.

Wall Wetting and Secondary Spray

Birkhold [17] reports results from a visualization of UWS droplet chains hitting a metallic wall under well defined conditions (droplet diameter, impact velocity and -angle, wall temperature), see Figure 2.8, right. In a first experiment the urea concentration within the UWS droplets was kept constant at its standard value of $32.5\,\%$. As a reference, the same experiment was conducted with pure water. In both cases, the impingement process has been analyzed under the variation of the wall temperature and the droplet stability number K, used in the model by Kuhnke [57], see Equation 2.12:

$$K = We^{1/2}Re^{1/4} = We^{5/8}La^{1/8} = \frac{(\rho D)^{3/4}u^{5/4}}{\sigma^{1/2}\mu^{1/4}} \qquad (2.12)$$

The latter is an alternative droplet stability measure to the We- and La-number used in the Bai-model. In comparison to We, K has the advantage of further reducing the phase space on the droplet dynamics axis. According to Kuhnke the splash/deposition limit becomes independent of La in this case [57].

Based on the camera analysis the impingement regime limits on the wall-temperature- and droplet-stability-axis have been determined for standard UWS and water. The resulting regime map for UWS is depicted in Figure 2.8, taken from [17].
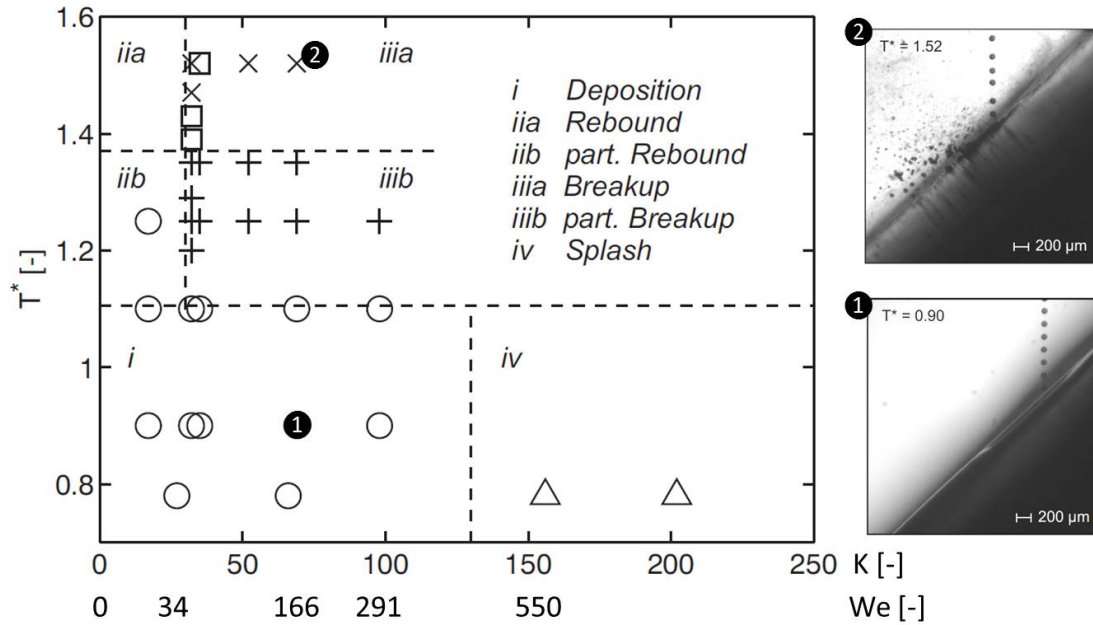
Figure 2.8: *UWS droplet-wall interaction regimes as a function of impact and wall temperature conditions, determined from droplet chain experiments [17]*

The qualitative regime distribution determined by Birkhold is in wide ranges in agreement with the one proposed in the the model frameworks by Bai and Gosman [58, 46], Kuhnke [57, 63] and Stanton and Rutland [59, 62]. A difference to the Bai-model is the existence of changeover regimes near the region limits (partial rebound, partial break-up) in the experiment, which are not covered by the model. Birkhold reports that there is no difference between the critical splash/deposition limit K-number between pure water and UWS. This is however only valid within the (relatively crude) measurement resolution, which allows a determination of the limit between $K = 98$ and 156. Due to the formation of a thin liquid film in the droplet chain experiment, the reported limit has to be regarded as valid for a wetted wall.

The critical temperature, which is separating the deposition from non-deposition regimes has been determined in an additional impingement study with varying urea content. Birkhold proposes the following relation between deposition limit temperature and the droplet's urea mass fraction:

$$T^*(Y_{urea}) = 1.19 + 0.56 \cdot Y_{urea} \tag{2.13}$$

Below this limit, the droplet mass is completely depositing on the wall and forming a liquid film. Above the limit, a successive transition to a thermal break-up can be observed. Absolutely no wall wetting occurs above $T_w \approx 1.4 \cdot T_{sat} = 522\,K$ for pure water and at

$T_w \approx 1.45 \cdot T_{sat} = 546\,K$ for standard UWS.

The impingement of a UWS spray from a state of the art UWS injector on a flat stainless steel wall has been investigated by Birkhold [17] and Li et al. [82]. A spray chamber has been used to maintain constant standard ambient conditions of the surrounding gas phase. Both authors use high speed video analysis to analyze the penetration behavior of secondary droplets from spray-wall-interaction. Parameters in both experiments are the injection angle ($45\,°$ to $90\,°$) and wall temperature. Experiments are conducted at constant values between $338\,K$ to $573\,K$ [17] and $350\,K$ to $650\,K$)

The major finding from both studies is that wall temperature most significantly affects the secondary spray shape. Both studies reveal that the radial penetration length, i.e. the secondary spray extension parallel to the wall, is increasing with increasing wall temperature. Birkhold additionally shows the inverse trend for the axial, i.e. normal to wall, penetration depth. The finding underlines that the relevance of the Leidenfrost phenomenon is not limited to heat transfer, but is also affecting momentum transfer: The levitation on their own vapour film beyond the Leidenfrost temperature leads to a high mobility of the droplets along the wall. Impinging droplets predominantly lose their momentum normal to the wall in this non-ideal collision. This effect is captured by the sliding regimes in the Bai-model, see Figure 2.5.

The deposition limit temperature for pure water and standard UWS, revealed from the spray impingement experiment by Birkhold [17], is $423\,K$ and $508\,K$ respectively. Those values are systematically below the ones for the the single droplet impingement experiment, which indicates a dependency of the deposition limit temperature on the particular spray/droplet characteristics.

Thermal Contact between Liquid UWS and Walls

A direct measurement of the heat transfer between liquid UWS and heated walls has not been published yet. However, some experiments allow an indirect insight into the process.

Musa et al. [19] have analyzed the decomposition behavior of single UWS droplets ($30\,\%$ of mass urea) dispensed onto a heated steel block. As a reference, similar experiments have been conducted for pure water droplets. For each experimental run the surface temperature has been kept constant by a controlled heater. A single droplet of a well defined diameter ($D \approx 2.7\,mm$) has been released from a dispenser placed approximately $15-20\,mm$ above the solid. An estimation yields impact Weber-numbers between $We \approx 11$ and 16, i.e. well below the splashing and the thermal break-up limit. In addition, the geometric setup of a bowl shaped surface, normal to the gravity direction, forces the droplet to keep in contact with the heated surface until its complete depletion.

For surface temperatures beyond the Leidenfrost spot, the post impingement droplet oscillates on a vapor cushion. Below this point, wall wetting can be observed. As the major output, the authors measured droplet lifetime as a function of the surface temperature, see Figure 2.9.

The measured curves reveal an inverse correlation between droplet lifetime and the Nukiyama
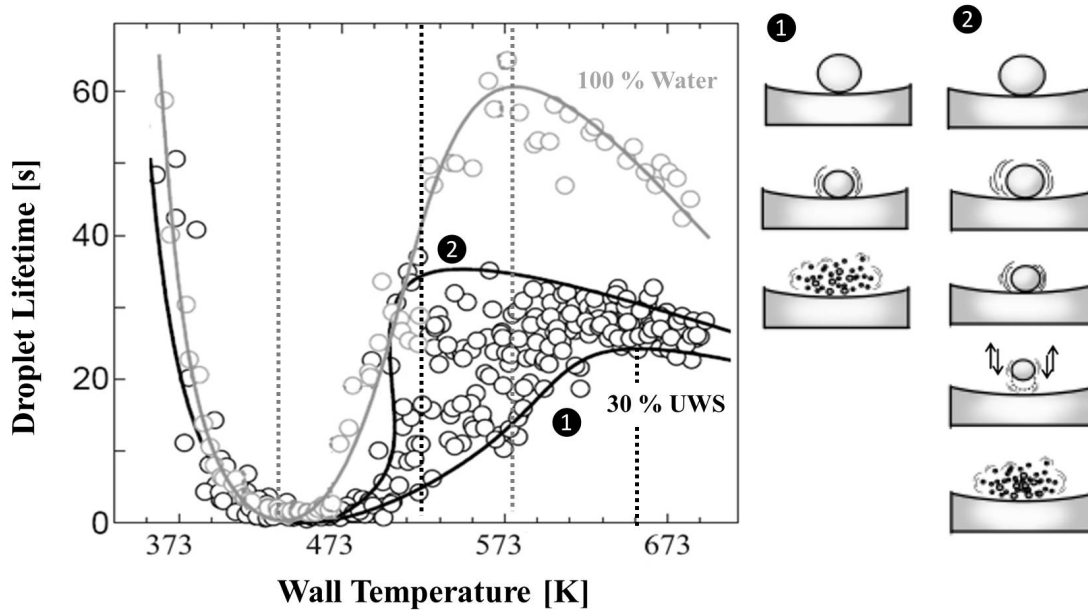

Figure 2.9:   *Lifetime of UWS and water droplets, dispensed onto a heated steel block (left), alternative decomposition mechanisms at elevated temperatures (right) [19]*

heat flux correlation, see Figure 2.7. However, the curve extracted for water droplet lifetime reveals that the particular regime limits seem to be shifted towards higher (excess) temperatures in comparison to the pool boiling values. The critical heat flux excess temperature is $\Delta T_{CHF} \approx 50\,K$, in the latter case, in comparison to $30\,K$ for pool boiling conditions. The Leidenfrost excess temperatures are $200\,K$ and $120\,K$ for attached droplet and standard pool boiling, respectively.

For UWS droplets, the correlation between lifetime and the Nukiyama heat flux curve becomes less definite. While it remains valid for surface temperatures below the critical heat flux temperature, a scattering of droplet lifetimes for the same boundary condition occurs beyond this point. In the latter case, Musa et al. [19] report two different evaporation scenarios, see numbering and illustrations in Figure 2.9, right. In the first case (1), a sudden diffraction of the droplet is described after a short foregoing levitation stage. In the latter case, the levitation phase is much longer, which enlargers the overall evaporation time significantly. Musa et al. deduce the differences to the complexity of the urea decomposition stage, without going into detail. A possible explanation for the disruptive fragmentation of the UWS droplet might be an internal gasification of water, possibly enhanced by the solid crust formation, described by Abu-Ramadan et al. [11], see Section 2.1.2. Moreover, the ongoing evaporation of water from the UWS is continuously changing the shape of the Nukiyama curve, which in return affects the boiling process and therefore the mass transfer.

Despite those uncertainties, the study allows for some conclusions with relevance for the modeling of solid-fluid heat transfer in SCR systems. First, the experiment reveals that the boiling mechanisms, originally observed for pool boiling experiments, remain in principle valid in the present droplet-on-surface experiment. A similar connection to the pool boiling correlation has been reported by several authors for the lifetime of droplets applied to a heated surface, see e.g. [83]. Additionally, boiling regime boundary temperatures can be roughly estimated from the experiment. For UWS the critical heat flux temperature ($T_{CHF} \approx 483\,K$, defined by minimum droplet lifetime) is slightly higher than for pure water. The Leidenfrost temperature (defined by minimum droplet lifetime) for UWS could at least be located between $T_L \approx 523\,K$ and $653\,K$.

The second type of experiments covers cases, where the wall temperature is not fixed by a controlled heater during the UWS impingement process. In those cases, a UWS spray affects the wall temperature due to spray cooling. By drawing the heat of vaporization and thermolysis enthalpy from the wall, the impinging spray cools down the wall with each injection event. Between two events, a temperature recovery occurs due to heat conduction within the solid. Both effects compete and determine the longtime evolution of wall temperature and the possibility of liquid UWS deposition. This is of particular relevance in automotive SCR systems.

In independent experiments Zheng et al. [10] and Birkhold et al. [39] analyzed the spray cooling by a standard UWS cone spray, injected into a straight exhaust gas pipe and targeting onto the opposite wall. Both groups have measured the wall temperature at the impingement position as a function of time for a series of injection events. Liquid deposition has been evaluated optically.

The transient wall temperature evolutions reported by Birkhold et al. reveal the transferability of the Nukiyama boiling concept to thermal spray-wall interaction. This finding is in accordance with previous studies on spray wall cooling for other liquids than UWS [83, 84, 85]. Starting from a surface temperature beyond the Leidenfrost point, the temperature is reduced at a low gradient due to a relatively low heat transfer coefficient in this regime. Birkhold et al. reports spray- and exhaust boundary conditions which in the long run lead to a cooling of the wall below the Leidenfrost temperature. Below T_L a permanent direct liquid-solid contact (i.e. wall wetting) sets in as the transient boiling regime is reached. Now the heat transfer is *increasing* with further *decreasing* temperature, see Figure 2.7. In accordance, the wall temperature drop in the experiment increases faster with decreasing temperature, i.e. the curvature of the $T_w(t)$-curve changes its sign. The data by Birkhold et al. allows a determination of the turning point, which theoretically coincides with the Leidenfrost point, around $T_L \approx 573\,K$. Despite this theoretic correlation, Birkhold et al. considers the point of maximum curvature of $T_w(t)$ for the onset of liquid film formation. This leads to $T_c \approx 538\,K$ to $553\,K$. From this point, a maximum gradient of $T_w(t)$ is reached within a short period, i.e. the curvature changes a second time, at T_{CHF}. This is again in accordance with the Nukiyama boiling concept. The temperature curves recorded by Birkhold et al. reveal a value of $T_{CHF} \approx 480\,K$. Further cooling is taking place in the nucleate boiling regime at a continuously decreasing gradient.

Finally a steady state temperature is reached, as the heat draw by spray cooling is balanced by heat conduction within the wall. The data reveals that any of the critical wall temperature values T_L, T_{CHF} is in good approximation independent on the particuar spray and exhaust boundary conditions.

Zheng et al. [10] report a critical wall temperature for the onset of massive wall wetting around $463\,K$ to $483\,K$. A very likely explanation for the deviations from Birkhold et al. 's data might simply be the definition for the onset of wall wetting. The temperature reported by Zheng et al. corresponds well with the temperature of maximum heat flux from the experiment by Birkhold et al. and Musa et al. [19]. This is probably the temperature where liquid film becomes the first time significantly obvious, though wetting might have already set in at even higher temperatures. Zheng et al. further report that the determined deposition limit temperature depends on droplet impact rate (spray mass per unit time) and impact density (spray mass per unit area), as well as the exhaust temperature and mass flow, which affects the heat flux within the pipe wall. These observations might again be a consequence of the wall wetting onset definition.

Similar experiments and findings have been reported by Nishioka et al. [25]. They have analyzed UWS spray interaction and deposition on a perforated impact plate exposed to an exhaust gas- and UWS spray flow. In addition to exhaust gas- and UWS mass flow and exhaust temperature, the authors varied the impact plate geometric parameters, including void rate, angle and distance from the injector. Nishioka et al. define an impact flux combining the UWS mass flow and effective spray impingement frontal area resulting from the intersection of the spray and plate geometric parameters. The authors also report a wall temperature drop coinciding with the onset of wall wetting. Moreover, they postulate the existence of a critical UWS impact flux for the occurrence of a permanent wall wetting, which increases with exhaust gas temperature. However, the provided data does not allow for a quantification of the deposition limit wall temperature.

2.3 Modelling Turbulent Exhaust Gas and Ammonia Mixing

Modelling the turbulent exhaust gas flow field is a precondition to evaluate the liquid UWS- and gaseous ammonia dynamics in SCR systems. The following section gives a theoretical overview on available turbulence models and the numerical description of scalar mixing. The survey is restricted to Reynolds Average Navier Stokes (RANS) formulations, as LES- or even DNS models currently cannot be regarded as practical for the computer aided system design of SCR systems due to their computational costs.

Among the RANS models, the major difference occurs between the standard two-equation-models (k-ε-models) and the Reynolds-stress-model (RSM). While the former solve a single

transport equation for each, the turbulent kinetic energy and -dissipation, the latter solves for all of the six components of the Reynolds stress tensor and one for the turbulent dissipation [86, 46]. The RSM therefore accounts for the anisotropy in velocity fluctuations that may be found between the main flow direction and the normal - i.e. secondary flow - directions in a turbulent field. As a consequence, the RSM is expected to be more expensive, but also more precise. It is commonly accepted that the consideration of anisotropy may especially be relevant in strong swirling flows, see e.g. [87]. The latter can be expected in SCR systems including swirl mixing elements. Despite these expectations, the impact of an elaborate turbulence model in SCR system simulation has not been analyzed yet.

Modelling gaseous scalar transport in a RANS formulation of the turbulent flow field, three mechanisms can be distinguished, see Equation 2.14 [86, 46]:

$$\frac{\partial}{\partial t}(\rho Y_m) + \frac{\partial}{\partial x_j}(\rho u_j Y_m + \rho \overline{u_j' Y_i'} + \rho V_{m,j} Y_m) = s_m \tag{2.14}$$

On the largest length scale a convective transport takes place, i.e. the scalar follows the direction of the mean flow field u_j. On the smallest length scale molecular diffusion, described by Fick's law with the diffusion velocity V_m, occurs. The scalar transport on intermediate length scales, due to small, unresolved, vortices of the turbulent flow, is - like the transport of momentum - based on the eddy viscosity hypothesis: The momentum coupling of neighboring flow sections by small scale vortices, is captured by the turbulent viscosity, see Equation 2.15:

$$\mu_t = C\rho\frac{k^2}{\varepsilon} \tag{2.15}$$

Considering scalar transport, a direct proportionality of turbulent diffusive momentum- and scalar transfer between sheering flow layers is assumed, Equation 2.16.

$$\overline{\rho u_j' Y_i'} = -\frac{\mu_t}{Sc_{m,t}}\frac{\partial Y_m}{\partial x_j} \tag{2.16}$$

The constant of proportionality Sc_t is the turbulent Schmidt number. For the k-ε-models, the turbulent viscosity, and therefore the turbulent scalar diffusion, can be directly calculated for a specified Schmidt number. For the RSM, an algebraic equation is employed to calculate the turbulent kinetic energy from the main diagonal Reynolds stress tensor elements. This energy is then, together with the dissipation, used to determine the turbulent viscosity and diffusion constant as for the two-equation models [46]. One has to bear in mind that this procedure implies the reduction of the RSM's anisotropic information regarding turbulent eddies to an isotropic mean turbulent energy - at least for the scalar transport. Currently, no anisotropic scalar transportation model is available in a commercial CFD code within a RANS formulation. Nevertheless, the turbulent diffusion is from a theoretic point of view indirectly affected by the RSM's anisotropic character through the resulting Reynolds stress dependency of the turbulent diffusion constant.

Another possible impact factor on scalar mixing simulations is the choice of numerical spatial discretization. Again, a trade-off between precision and cost occurs from a theoretical point of view. A first order differencing scheme (e.g. upwind differencing, UD) is less time consuming but has, by definition, a truncation error of second order [86]. For ammonia transport, the error with the UD scheme is therefore proportional to the gradient of the scalar and the mesh resolution Δx, see Equation 2.17 [86]:

$$f_{Y_m} = \rho u_j \frac{\Delta x}{2} \frac{\partial Y_m}{\partial x_j} \tag{2.17}$$

If the mesh resolution is not sufficiently small, the resulting numerical diffusion [86] might be of the same order of magnitude as the physical effect of turbulent diffusion, compare Equation 2.16 and 2.17. This can lead to severe misinterpretations of numerical homogenization predictions. A higher order scheme (second order or higher) shifts the truncation error to a higher order and does not show a second order effect of numerical diffusion. The solution becomes less sensitive to the particular mesh resolution. It therefore seems - though more expensive - from a theoretical point of view the better choice.

Though not in the context of SCR, there are a few works that allow a first estimate of the practical relevance of turbulence description and numerical discretization for scalar transport results:

In an early work on turbulence models, El-Tahry [87] has compared the results of a standard k-ε-model, a simplified constant diffusivity model and the more sophisticated Reynolds stress model to velocity measurements in an engine-like geometry. The main finding has been that both, the k-ε-model and the RSM, predict the mean velocities in good agreement. However, according to the study, only the RSM with its tensor character is able to predict realistic levels of anisotropy of turbulence components, in direction normal to the main flow. The two equation model was proved to be incapable of such calculations. El-Tahry underlines that this difference is especially pronounced, if strong normal stresses occur, e.g. in swirl flows. The author states that this might become especially important considering scalar diffusion.

Tominaga and Stathopoulos [88] review a number of CFD works on the diffusion of scalars in different types of turbulent flows, modelled by RANS equations. The reviewed cases include a scalar jet injection into a crossing flow and the dispersion of a plume from a single point source in an open field environment and around buildings. All cited studies undertake an adaption of the turbulent Schmidt number to better match the scalar's measured concentration distributions. This adaption can - according to the Tominaga and Stathopoulos - be regarded as a compensation of underestimated turbulent momentum diffusion, i.e. underestimated turbulent viscosities, by the turbulence models [88]. Accordingly an underestimated turbulent viscosity has therefore in all discussed cases been compensated by reducing the Schmidt number from its standard value $(0.7 - 0.9)$, see Equation 2.16.

2.4 CFD Studies of UWS based SCR Systems

A number of CFD studies and model descriptions of the UWS preparation in SCR systems have previously been published.

A common feature to all of the so far published numerical studies is the application of a two-equation RANS-model for the turbulent exhaust gas flow. In any case the gas flow is modelled in an Euler description. Droplet- and - if considered - liquid film-dynamics are described in a Lagrangian approach. Two way coupling between dispersed and gas phase is taken into account in any model. As a state of the art approach primary spray break-up from the injector is not modelled. Instead, droplet size distribution and injection velocity as well as cone angles are obtained from measurement and implemented as a spray boundary condition. Ammonia vapor is modelled as a scalar, released from UWS droplets according to one of the decomposition models discussed in Section 2.1.2. Despite these common features, the proposed setups differ significantly in submodel depth for the different preparation steps and the particular focus of results. Moreover, experimental validation is only available in selected studies and / or on selected topics.

UWS Droplet-Gas Interaction

With respect to a predictive CFD-Simulation it is necessary to capture all relevant forces that act on the UWS droplets within the turbulent flow field. A numerical sensitivity study that has focused on this topic has been published by Ström et al. [40]. The authors analyzed the impact of numerous forces, including drag, buoyancy, lift effects, thermophoresis and history effects on UWS droplet dynamics prediction in an Euler-Lagrange modelling approach for liquid gas interaction. A straight pipe configuration with injection of a typical UWS cone spray has been used throughout the study. The study proves that for typical SCR system configurations and exhaust gas conditions it is necessary to include drag force and gravity effects. Moreover, the study reveals that turbulent dispersion, represented by a stochastic particle tracking model, is one of the most crucial effects, to correctly capture the interaction with the turbulent eddies. This not only enhances the dispersion of droplets, but also the heat and mass transfer. However, the authors emphasize that the outcome of a stochastic turbulent dispersion model is directly affected by the predictions of the chosen turbulence model. In accordance to the theoretical considerations from the previous subsection, they noticed that a k-ε-RNG- model, which they employed throughout their study, might in that sense be critical, due to its inherent limitation of isotropic turbulence assumption. Ström et al. conclude that a more advanced turbulence model might be necessary, especially when analyzing more complex geometries including bends, diffusers, etc..

Despite this issue, CFD studies of SCR systems in literature have not yet focused on the relevance of turbulence modelling when predicting both turbulent droplet dispersion and ammonia homogenization. Numerous authors based the dispersed phase model on those findings by Ström et al., however limiting the turbulence description to k-ε descriptions.

Abu-Ramadan et al. [11], Munnannur and Liu [42] have considered aerodynamic drag and turbulent dispersion of the UWS spray, neglecting gravity effects. Bhattacharjee and Haworth [38] have additionally considered buoyancy and a pressure based virtual mass force (Magnus effect). Moreover, Bhattacharjee and Haworth have analyzed the sensitivity of spray predictions on the parcel number. They compared the results of the UWS spray dispersion and decomposition from a representation with 10^4 to one with 10^5 parcels. Sensitivity has been reported to be very moderate on this order of magnitude, while the effort scales linearly with the parcel number.

Impingement and Liquid Film Studies

Several authors have postulated a significant impact of UWS droplet impingement for correct modelling of the overall system chain and the SCR performance, see e.g. [47, 11, 38]. Despite this consensus, there is only a limited number of reports on the application of a detailed impingement model to the UWS preparation process. Available CFD results focus on selected aspects of the impingement process and / or are restricted to a limited range of relevant exhaust gas conditions. Thus, the overall impact on the system performance, in particular on UWS decomposition timescales and ammonia homogeneity, has not yet been conclusively examined. However, taken together, the published CFD studies reveal important aspects for a predictive description of the UWS preparation process.

Ström et al. [40] have limited the impingement analysis to a postprocessing estimate of the extent of wall impact. Droplets hitting the wall are categorized, based on the impingement regimes proposed by Kuhnke [57]. Despite the simplified approach, the authors were able to prove that turbulent dispersion significantly enhances the fluid-wall contact probability, due to repeated impingement of droplets in the near wall boundary layer. This phenomenon is driven by small vortex structures captured by the turbulent dispersion model. Ström et al. report that this significantly affects the evaporation efficiency.

Bhattacharjee and Haworth [38] compared a single regime droplet-rebound model (referred to as 'no-interaction' due to the non-ideal reflection of droplets without any thermal wall contact), to the multi-regime Bai-Model [58] and the more simplified multi-regime MPI-Model [89, 46]. The analysis has been carried out on a simplified straight pipe configuration. The UWS injector (SMD $76 \, \mu m$) is placed at the center of the inlet plane with the main spray axis parallel to the main flow direction. Sensitivity of the predicted UWS preparation efficiency to the impingement model has been evaluated by comparing the global rate of urea, released within the pipe, as a function of the submodel. The major finding is that the released ammonia mass fraction is two orders of magnitudes higher for the complex spray-wall interaction models (Bai, MPI) in comparison to the simple no-interaction model. The observation has been traced to a significant increase of UWS evaporation in the near wall-region for the complex impingement model [38].

The authors postulate that the thermal droplet-wall contact, in comparison to droplet-gas

heat transfer, dominates the overall evaporation process. They therefore generally recommend the inclusion of an elaborate impingement model. Based on the moderate differences, found between the Bai- and the MPI-model, the authors conclude that the particular choice of the submodel is of secondary interest. However, a generalization of the latter statement has to be regarded as doubtful for the following reason: The sensitivity study has been restricted to a single operating point (exhaust gas temperature $668\,K$, -mass flow $231\,kg/h$), despite the expected dependency of impingement outcome on the particular wall boundary condition (surface temperature). The authors are well aware that the chosen adiabatic thermal wall boundary condition implies the neglecting of spray cooling effects, which affects heat- and mass transfer during impingement. In addition, no remarks have been made on the particular parametrization of the impingement models, i.e. regime boundaries.

Yi [41] employs the multi-regime impingement model based on the works by Stanton and Rutland [59, 62]. The analyzed geometry consists of a straight pipe, leading into the catalyst inlet cone under a small angle. The UWS injector is located at the pipe wall in an unspecified distance (approx. $0.5\,m$) upstream of the catalyst, releasing the UWS spray in a $45\,°$- angle relative to the main flow, targeting on the opposite pipe wall. Calibration of the impingement submodel to UWS is not reported and the study is limited to a single operating point (exhaust gas temperature $723\,K$, -mass flow $1080\,kg/h$).

Yi reports that the trapped amount of liquid on the wall is very small in that particular case ($\ll 1\,\%$). Taking the high gas temperature into account, this is very likely a consequence of the Leidenfrost phenomenon covered by the impingement model.

In contrast to Bhattacharjee and Haworth [38], Yi finds that the evaporation from liquid film is much slower than from droplets within the gas phase. From a theoretical point of view this might, like the low extent of liquid on the wall, be consequence of an insulating vapor film. However, the author does not report the application of any liquid film boiling model. A more likely explanation for this controversy are the different simplifications introduced by the authors to model the thermal wall boundary condition. While Bhattacharjee and Haworth [38] assume an adiabatic wall (perfect insulation), Yi [41] models the wall by specifying an external temperature and heat transfer coefficient assuming natural convection. In the former case, the wall temperature is by definition unaffected by the liquid evaporation, in the latter, a significant overestimation of wall cooling is possible as neither heat conduction within the solid pipe nor its heat capacity is captured. As the observation from the different authors indicate, both extremes may very likely affect the outcome of liquid film evaporation.

Despite those modelling details, Yi reports some general impacts of the impingement process on the UWS mixture preparation. The author compares the no-mixer geometry to two configurations, each with a different mixing element. The numerical study reveals that both mixers enhance the droplet atomization due to the impingement process. Though not explicitly stated, it is very likely that a thermal break-up occurs on the mixers for the particular operating conditions reported by Yi [41]. Due to the resulting better surface-to-volume ratio of the droplets, the impingement enhances evaporation. This reduces the amount of liquid UWS at the catalyst and improves the ammonia homogeneity at its inlet [41].

Very similar observations have been reported by Munnannur and Liu [42], who have analyzed UWS spray preparation in a straight pipe system with a blade-mixer. The authors have employed the same impingement model as Yi. Like Yi they state that splashing at the mixer plays a key role in enhancing decomposition. Downstream of the mixer, most droplets were found to consist of pure urea, but nevertheless some droplets reach the catalyst $0.8\,m$ downstream of the mixer. Again the (single) analyzed operating point was in the high temperature regime (exhaust gas temperature $661\,K$, -mass flow $824\,kg/h$).

An elaborate UWS liquid phase model has been employed in CFD simulations by Birkhold et al. [39, 17]. The authors have adopted the Kuhnke impingement model [57] to UWS behavior based on single droplet impingement experiments, see Figure 2.8. Heat transfer from walls beyond the Leidenfrost temperature to impinging droplets is taken into account according to a contact model [76], see Section 2.2.1. For liquid films, heat transfer from walls beyond the boiling temperature is modelled by the Nukiyama boiling correlation. The urea concentration dependency of the boiling behavior is neglected and instead the correlation for pure water employed. Liquid film is modelled with a two-dimensional finite volume method considering shear-, gravity-, pressure gradient forces.

The described CFD simulations and results focus on a basic evaluation of the employed submodels. Primary spray dynamics and propagation have been found to be in good qualitative agreement with PDA measurements and visualization [39]. With respect to impingement model validation, the authors simulate the spray cooling experiment described in Section 2.2.2. They prove that the simulated wall cooling curves are in good agreement with measurements. The model is capable to describe the transition from non-wetting surface temperatures, i.e. above the Leidenfrost temperature, to a deposition regime leading to wall wetting and a further massive wall cooling. In order to cope with the comparably long time scales for spray induced wall cooling ($O(10^1 - 10^2\,s)$ [39]), Birkhold et al. propose a two-dimensional parallel heat conduction wall model, modified by the introduction of a speed-up factor. The latter is used to numerically reduce the solid wall thickness and therefore the wall's thermal mass. This reduces the calculated timescales of the cooling process, as less enthalpy per unit time is necessary to obtain the same local wall temperature reduction. Simulated cooling time is then again stretched by the inverse correction factor in the postprocessing procedure for validation purposes.

Though this approach is proved to allow for a correct description of the wall cooling, it remains unclear, how the corresponding liquid film mass (-transfer) is treated. In particular it remains open, how the authors deal with liquid film dynamics, which also occur on comparably long time scales. Despite these uncertainties Birkhold et al. state that the simulated liquid film shape is in qualitative agreement with the one optically observed in experiment. However, the authors notify that they simplify the description of film properties by using viscosity- and surface tension correlations for pure water instead of a UWS concentration based values.

Apart from the above investigations, the literature lacks further attempts to simulate a long-

time UWS liquid film formation. At the current state its relevance for the overall SCR process therefore remains unclarified. Several authors name the time scale discrepancy between fast droplet dynamics $O(10^{-4}\,s)$ and slow liquid film evolution $O(10^1 - 10^2\,s)$ as a major challenge preventing CFD from covering the latter with reasonable computational effort [39, 38].

Ammonia Homogenization Simulation

Based on liquid UWS dynamics and decomposition submodels of varying depth, some publications have described the CFD-simulation of ammonia vapor homogenization. A direct comparison between numerically predicted and measured uniformity can however rarely be found. Interestingly, all of the cases that have been validated regarding homogenization [17, 38] - underestimate the measured ammonia uniformity to some extent.

In addition to the impingement relevance study, described previously, Bhattacharjee and Haworth [38] have conducted a sensitivity study of ammonia homogenization predictions on mesh resolution. Again they employ a simplified straight pipe geometry. They state that differences of ammonia concentrations predominantly appear in the near wall region. The effect is described to be extremely small for intermediate and fine meshes (cell edge sizes $10\,mm$, $5\,mm$) and only relevant for a very coarse mesh ($20\,mm$).

In a more complex geometry they analyze the sensitivity of ammonia mixing to the porosity index, for the widely used porous medium approach for the SCR brick. Major result is that the effect is very small, concluding that any resistance different from zero will be adequate to leave homogenization predictions upstream of the catalyst unchanged.

In a further study they compare the basic straight pipe to a modified straight pipe configuration with a $90\,°$-bend upstream of the injector. The modification leads to a distinct swirl flow downstream of the injection. The velocity magnitudes, normal to the main flow are nearly equal the axial ones. As a consequence, ammonia homogeneity at the catalyst intake is significantly enhanced. A quantification of the effect is however not presented. Finally, the authors describe the experimental validation of the ammonia homogenization prediction for a heavy duty vehicle SCR system. The proposed model covers general trends in the ammonia distribution at the catalyst inlet correctly. A quantitative comparison is regarded as difficult and not conducted, due to the limited number of measurement locations.

The work by Birkhold also offers some validation results regarding ammonia homogenization. Based on the elaborate liquid phase model (see previous subsection) the author simulates the homogenization of ammonia in a straight pipe setup, with a $45\,°$ spray injection angle relative to the main flow direction, targeting on the opposite wall. The predicted ammonia distribution at the downstream catalyst is compared to concentration measurements at nine discrete locations for two engine operating conditions. The agreement is described as sufficient, with a good correlation of ammonia maxima locations. Nevertheless, Birkhold reports substantial quantitative deviations in the predicted ammonia distributions, without quantifying them [17]. From the distribution figures, an overestimation of concentration gradients in

the catalyst intake plane can be observed. As a probable explanation the author identifies the neglect of real pipe features, like welded seems and small kerbs. Regarding model insufficiencies, he considers the impingement model as an error source [17].

Gehrlein et al. [90] compare different mixing elements and a no-mixer setup in a straight pipe with respect to back pressure and uniformity of ammonia. Though the publication focuses on experimental data and methodology, they briefly describe a CFD-model and a validation case. Again, a standard k-ε-high Re model is used [90]. For the validated mixer case, the simulation yields a uniformity index (see Equation 7.2 for UI-definition) of 0.90 at the catalyst, in comparison to a measured value of $\overline{UI} = 0.93$. The simulated ammonia distribution is qualitatively correct, but reveals steeper gradients from rich to lean ammonia regions.

Further publications are limited to numerical sensitivity studies without offering validation data:

Jeong et al. [45] analyze the relevance of UWS injector position, -hole number and -pressure on the ammonia uniformity at the SCR catalyst with the CFD method. Their setup consists of an s-bend type pipe with tangential injection and a diffuser leading into the catalyst. They employ a k-ε-RNG turbulence model with a second order differencing scheme (MARS) for the gas phase flow. A major result is that increasing the distance between injector and catalyst leads to a rise of the ammonia uniformity index. The uniformity changes from $UI = 0.55$ to 0.82 (i.e. $+61\%$) by increasing the injector-catalalyst distance from one times the pipe diameter to seven times. They describe a saturation of the effect at a distance of five times the pipe diameter ($+58\%$, $UI = 0.81$).

Yi [41] analyzes the effect of two different mixers on the homogenization. Like Jeong et al. [45] Yi uses a k-ε-RNG for turbulence and an evaporation law for the release of ammonia vapor. Without a mixer the straight pipe setup leads to an impingement of droplets on the opposite wall, which in turn results in a strong local asymmetry in ammonia release. As a consequence, the author observes a poor uniformity of ammonia at the catalyst inlet face of $UI = 0.41$. Integrating a helix swirl mixer into the - in other respects unchanged - setup leads to an improvement to $UI = 0.61$, while the integration of a small plate mixer (no swirl) results in a less improved value of 0.56. In addition to ammonia gas phase mixing enhancement by the mixing elements the author emphasize the importance for spray atomization, see previous subsection. As an explanation for the relatively low overall homogeneity, the author suggests that the injection position is not compatible with the exhaust pipe geometry.

In a very similar manner, Zhang et al. [91] numerically analyze the impact of a static mixing element on the ammonia homogenization in a straight pipe exhaust systems. They vary the mixer position relative to the injector (upstream, downstream), mixer blade number, -shape and blade twisting angle. In contrast to all other works cited here, they use a simplified gaseous ammonia injection. The gaseous injection is placed in the radial pipe center. The turbulent flow is described by a standard k-ε-high Re-model.

Without mixer the ammonia uniformity increases smoothly along flow direction. The straight blade mixer leads to a jump in the UI right behind mixer from 0.54 to 0.67 within $20\,mm$. Further downstream a significant smaller gradient in uniformity ($UI = 0.92$ at $320\,mm$) is observed. The major enhancement is therefore predicted within a very short distance from the straight blade mixer. Employing the twisted blade mixer they find an additional swirl generation, with the swirl flow being less intense in turbulence, but showing a slower dissipation than the straight blade mixer flow. Therefore, the effect on mixing of ammonia vapor is observed to last further downstream, but to be less intense on a short scale. This observation is in agreement with Yi's results [41]. The authors explain the simulated behavior as a result of a trade-off between small scale turbulence and large scale swirl [91].

Krenn et al. [92] describe a CFD simulation for a passenger car SCR system, with the UWS spray injector targeting on an integrated blade mixer. Urea decomposition is simulated with an evaporation approach, and ammonia vapor treated as an active scalar. The Bai-model is employed for droplet-wall interaction. Details on calibration are not specified. Turbulence is modeled with k-ε-RNG. For transport equations of turbulence and scalars a first order upwind scheme (UD) is used, while momentum is discretized with a second order scheme (MARS).

The authors optimize the mixers rotational position, in order to maximize the ammonia uniformity at the catalyst. In their numerical study the authors observe a $6\,\%$ increase in uniformity at the catalyst inlet plane by an optimized rotational mixer positioning.

3 Research Objectives

The general task of the present work is the implementation of a **CFD simulation method** that meets the demands for an efficient optimization **of urea-water solution (UWS) based automotive SCR mixing systems**. The model should predict the behavior of UWS and ammonia mixing for a wide range of exhaust gas conditions with a single integrated physically-motivated model. Therefore, the relevant modelling depth to describe each subprocess upstream of the catalyst with sufficient precision but minimum effort is determined by numerical sensitivity studies and comparison to experimental data.

In a first step, an efficient thermodynamic **UWS decomposition model** will be implemented and validated based on available literature data. In addition, the study aims at further insights into the urea thermolysis process and its description.

Though attempts have been published to understand and cover UWS spray-wall interaction and related wall film formation by simulation, there is still a lack of knowledge on their particular impact on UWS preparation time scales and on the ammonia homogenization. Therefore, the present work aims at a predictive multi-regime model of the **UWS spray impingement and liquid film model**. In this context, the relevance of a detailed thermal **wall boundary description** for the prediction of wall wetting phenomena will be analyzed. A calibration of relevant liquid phase submodels is carried out and CFD predictions are validated by experimental studies on a simplified straight pipe geometry. Based on the validated liquid phase model, the **effect of liquid film formation on the ammonia release** will be analyzed in detail.

The **impact of turbulence modelling and the numerical discretization on the ammonia homogenization** prediction is yet unclarified. Arising from uncertainties in literature, a systematic study on the relevance of those factors on the prediction of the turbulent mixing process of gaseous ammonia will be conducted. To meet the demands that are valid for automotive SCR system development in an industrial process, those studies are carried out for a state-of-the-art SCR-mixing section geometry with swirl mixing element. A **best practice Reynolds Averaged Navier Stokes (RANS) description** of the turbulent flow to predict ammonia mixing will be determined by a comparison to ammonia uniformity measurements. The gained liquid phase model from the previous implementation stage will be applied to study the **correlation between UWS liquid phase dynamics and the ammonia preparation and -mixing process** in the production type SCR system.

4 Analysis Methodology

In order to reduce interdependencies of relevant subprocess to a minimum, the CFD model implementation and validation is performed in a hierarchic strategy. In a first stage, a UWS decomposition model is implemented and validated by analyzing single droplet decomposition with the CFD method in comparison to experiments from literature. In the next stage, liquid phase dynamics are studied for a realistic UWS spray injected into a simplified straight pipe geometry. Mass transfer from droplets and film to the gas phase is modelled in accordance to the thermodynamic description from the first implementation stage. The third stage model is based on the previous findings on mass transfer description and liquid phase dynamics. A complex production type geometry is examined, focusing on gaseous ammonia mixing and its correlation to liquid phase dynamics in a turbulent swirling flow.

4.1 Operating Conditions and Exhaust Gas States

In all implementation stages, a common ensemble of exhaust gas conditions is analyzed. The selected operating points (OPs) are representative for typical test cycle conditions during the NEDC and analogue international test cycles, see Figure 1.4. They cover a wide range of exhaust gas flow and -temperature states, see Table 4.1.

Each operating point is characterized by an exhaust gas mass flow and -temperature, as well as by the NO_x engine raw emission, that determines the UWS injection mass flow. As UWS is injected as an intermittent spray, the average mass flow is determined by the injection interval (time between two injection events) and the duration of each injection event (time that the nozzle is open).

Table 4.1: Analyzed Operating Points, 1*: Modified in production type system, Section 7

OP	0	1	1*	2	3
Exhaust Gas Temperature $[K]$	200	250	250	350	450
Exhaust Gas Mass Flow $[kg/h]$	75	100	130	200	350
UWS Mass Flow $[g/h]$	20	20	43.2	90	90
Injection Duration $[ms]$	5.0	6.35	5.76	9.5	9.5
Injection Interval $[ms]$	900	1000	385	333	333

At the engine test bench, the conditions are realized by adapting load and engine speed, in the simulation, the mass flow (i.e. inlet velocity) and exhaust temperature are implemented as an inlet boundary condition. For the single droplet decomposition studies, spray conditions are not relevant for obvious reasons and flow conditions are implemented in accordance to the particular experiment. In this case, the droplet initial conditions (diameter, temperature) and ambient gas temperature are implemented in correspondence to the experiment.

4.2 General Model Features and Simulation Procedure

All simulations are carried out with the commercial CFD code Star-CD [46]. Each simulation set consists of a steady state calculation of the stationary exhaust flow field and a transient simulation of the OP, including the UWS injection. The steady state run is performed until a convergent state is guaranteed. The convergent solution is then used as an initialization for the transient calculation.

In both, transient- and steady simulation, the Simple algorithm is used for temporal discretization. Residual tolerances are set to 0.01 for momentum, turbulence, enthalpy and scalars and to 0.001 for the pressure equation. Spatial discretization is set to upwind (first order) and MARS (second order) for enthalpy and pressure, respectively, under all circumstances. Further discretization scheme selection (for momentum and scalars) is a matter of research of the work at hand, see Section 7. It is set to MARS as a reference, if not specified otherwise, in the following.

The transient UWS spray behavior in the exhaust gas is modelled in an Euler-Lagrange approach with two way coupling [40, 46]. In order to precisely capture droplet dynamics, reasonable Courant-numbers are achieved with a time step of $0.2\,ms$ while droplets are present in the domain. In order to nevertheless cope with the gap in timescales of fast droplet dynamics and relatively slow liquid film dynamics, the time step is changed to $1\,ms$ once all droplets have left the domain by evaporation, impingement or through the outlet. This allows for long time studies and multiple injection events with a more moderate computational effort.

Depending on the modelling stage, and therefore the CFD mesh cell count, calculations are carried out on up to 24 cores (i.e. 3 nodes, each with two quad core processors) on a Linux Cluster. Postprocessing is based on user defined macros, implemented in the Star-CD (Pro-Star) programming language [46] and a Linux-shell script based extraction of results from simulation log files (awk-method).

A detailed description of further physical models, involved in each implementation stage of the CFD simulation, and corresponding validation experiments will be discussed in the following sections.

5 Thermodynamic Model of UWS Decomposition

5.1 UWS Evaporation- and Decomposition-Model

UWS is described as a two component miscible liquid, composed of water and urea. Thermodynamic properties as a function of temperature are taken from literature for the two components or the mixture as far as correlations are available. An overview is given in Table 5.1.

The property correlations are implemented in a user defined subroutine. Specific heat, saturation pressure and the latent heat of vaporization are defined as temperature dependent component properties. Mixture properties, resulting from those correlations and the current composition of the UWS (mass fractions of water and urea), are internally calculated by the CFD code during runtime. Density, viscosity, surface tension and thermal conductivity have to be defined as bulk-, i.e. mixture properties, in the current Star-CD modelling framework. In those cases, an explicit calculation of bulk properties or an approximation is undertaken for describing the UWS. The mixture density is taken for standard UWS, justified by the nearly unchanged value during UWS decomposition. The mixture thermal conductivity is approximated by the correlation for pure water for a lack of data on urea. UWS viscosity is taken from [95] according to the mixtures current temperature, which allows for an estimation of its current composition, see next subsection. As no measurement data is available in literature for the surface tension of urea, it is calculated from the Parachor theory for Polymers and the Eötvös's Rule [96]. The necessary parachor for urea is taken from Roseman and Jencks [97]. The mixture's surface tension is again modelled explicitly by a temperature-composition correlation.

The decomposition of UWS droplets is modelled as follows: Internal droplet mixing is described with the more efficient Rapid Mixing model. The choice is based on the small impact, resulting from more complex descriptions (DL, ED), see Section 2.1.2 [14, 11]. Thus, a droplet's internal species concentration- and temperature distribution is neglected. In accordance to the findings by Abu-Ramadan et al. [11], an evaporation approach is preferred over an Arrhenius type model, to describe the mass transfer of both, water and urea. The saturation pressure curve for urea is taken from Birkhold's latest setup [17] (see Figure 2.4, blue curves. The major reasons for this choice are its origination from a boiling point determination and its consistency with the instant thermolysis assumption. Water vapor pressure is described with the Wagner equation [93]. Raoult's and Dalton's law are employed to determine the partial

Table 5.1:   Thermophysical properties of urea, water and UWS

Property [Dimension]	Liquid			Comment
	Urea	Water	UWS	
Specific heat $[J/kg \cdot K]$	[17]	[93]	implicit	-
Saturation pressure $[Pa]$	[17]	[93]	implicit	Raoult's law
Heat of vaporization $[J/kg]$	[17]	[93]	implicit	single step thermolysis
Density $[Pa \cdot s]$	-	-	[94]	std. UWS
Viscosity $[Pa \cdot s]$	-	-	explicit [95]	-
Surface tension $[N/m]$	[96, 97]	[93]	explicit	-
Thermal conductivity $[W/m \cdot K]$	-	[93]	[93]	pure water

pressures and total vapor pressure from the components saturation pressure curves. Boiling is considered, if the mixture's vapor pressure exceeds the ambient pressure. The resulting standard boiling temperature $T_{sat}(1\,bar)$ as a function of the mixtures urea mass fraction Y_{urea} is shown in Figure 5.1.

Below T_{sat} mass transfer is modelled by the vaporization model according to Equation 2.2 [98, 46]. If the boiling criterion is fulfilled, a heat transfer limited mass transfer correlation is applied [46]. Heat- and mass transfer coefficients are determined from the correlations by Wakil et al. [56] and Ranz and Marshall [55] respectively [46].

No assumption is made for the water content to define the onset of urea thermolysis, i.e. the model is predictive with respect to the transition from water evaporation to urea decomposition. Melting, evaporation and thermolysis of urea is modelled as a single step process, considering an instantaneous dissociation of gaseous urea in the liquid-gas boundary layer [17]. Therefore, the thermolysis enthalpy is lumped together with melting and evaporation enthalpies and affecting the droplet energy balance [17]. No temperature dependency of this total latent heat is taken into account.

The decomposition of UWS leads to active scalars for water and an ammonia vapor representative. Isocyanic acid is not modelled explicitly, i.e. no explicit thermolysis reaction is simulated. The hydrolysis reaction and further gas phase chemistry is also ignored during simulation. This procedure is based on the assumption that the transport of ammonia and isocyanic acid in the turbulent flow can be regarded as identical, so that the former is representative for both and the latter has not to be considered explicitly. Local FTIR concentration measurements of both species approve the validity of this assumption [99]. The actual conversion of isocyanic acid to ammonia is therefore considered in the post processing only, assuming a very fast hydrolysis at the catalyst. Gas phase properties of the species water vapour and the ammonia representative are taken from the Star-CD database, with exception of the binary diffusion constants. The latter are modelled as temperature and pressure dependent properties
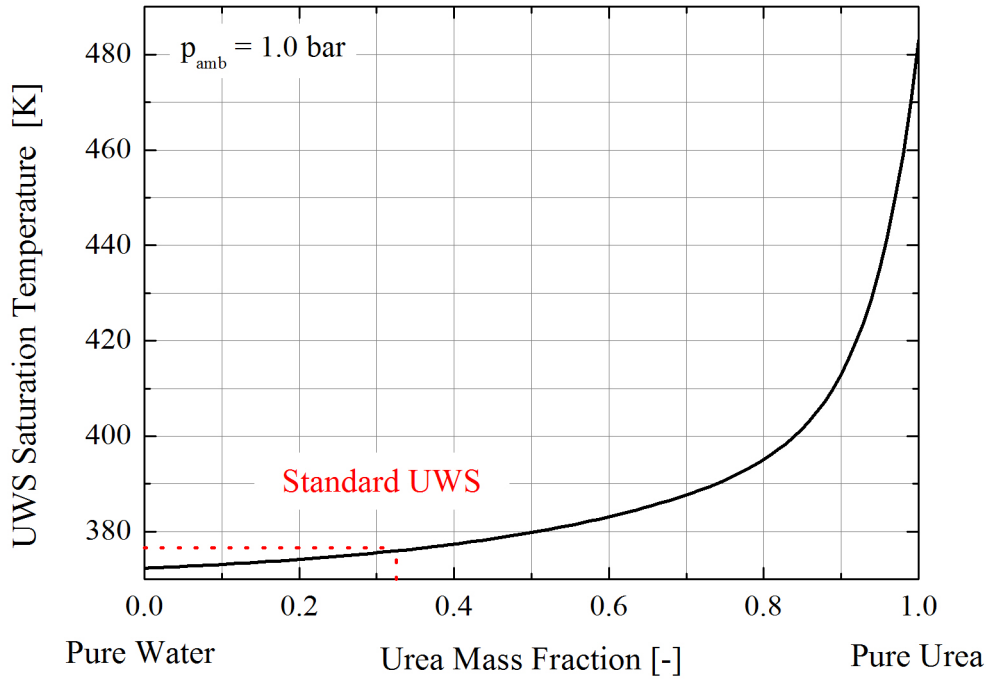
Figure 5.1: *UWS saturation (boiling) temperature at standard conditions ($1\,bar$) as a function of urea content, based on the urea saturation pressure curve proposed by Birkhold [17]*

on the basis of the theory presented in [93], see Equation 5.1:

$$\Gamma_i^g(T_g) = 1.013 \cdot 10^{-7} \frac{\sqrt{\frac{M_i+M_g}{M_i M_g}}}{\Omega_{i,g}} \frac{T_g^{1.75}}{p_g} \tag{5.1}$$

The effective collision diameter correlations $\Omega_{i,air}$ are taken from [93] for water and ammonia in air. The resulting values are in good agreement with the measurements presented for water vapor and ammonia in [100].

The chemical formation of undesired by-products, see Sections 2.1.1 and 2.1.2 is not considered in the present model. A prognosis of undesired depositions is therefore currently limited to a rough estimate of reaction regimes according to Schaber et al. [22] on the basis of predicted UWS temperature and composition, as well as the formation of liquid film. Correctly covering the latter is in any case a precondition to the prediction of chemical deposits. Once ensuring a correct liquid film prediction and temperature level, the present model structure allows for an extension to a chemical model of deposit formation.

5.2 Model Validation

In order to validate the UWS decomposition model a numerical single droplet evaporation experiment has been carried out with the CFD method in a small cubic CFD mesh ($\approx 10^4$ cells, cell base size ($\approx 3\,mm$). In each numerical run, the evaporation of a single UWS droplet of a well defined initial diameter (D_0 between 20 and $1000\,\mu m$) has been studied for a constant ambient gas (air) temperature. Specific heat, and heat conductivity of the background fluid are implemented in a user defined subroutine as polynomial correlations for dry air, taken from [93]. Molecular viscosity of the background is calculated from the Sutherland equation [46]. Ambient gas velocity has been initialized at $0\,m/s$ and no source term for momentum (inlet flow) has been considered. Therefore, convection is avoided and it can be postulated that the droplet evaporation process is limited by the diffusive motion ($Sh = 2$) and heat transfer ($Nu = 2$) in the boundary layer.

As an example Figure 5.2 shows the temporal droplet diminishing process, as predicted by the UWS decomposition model, for a $250\,\mu m$ droplet at different ambient gas temperatures.
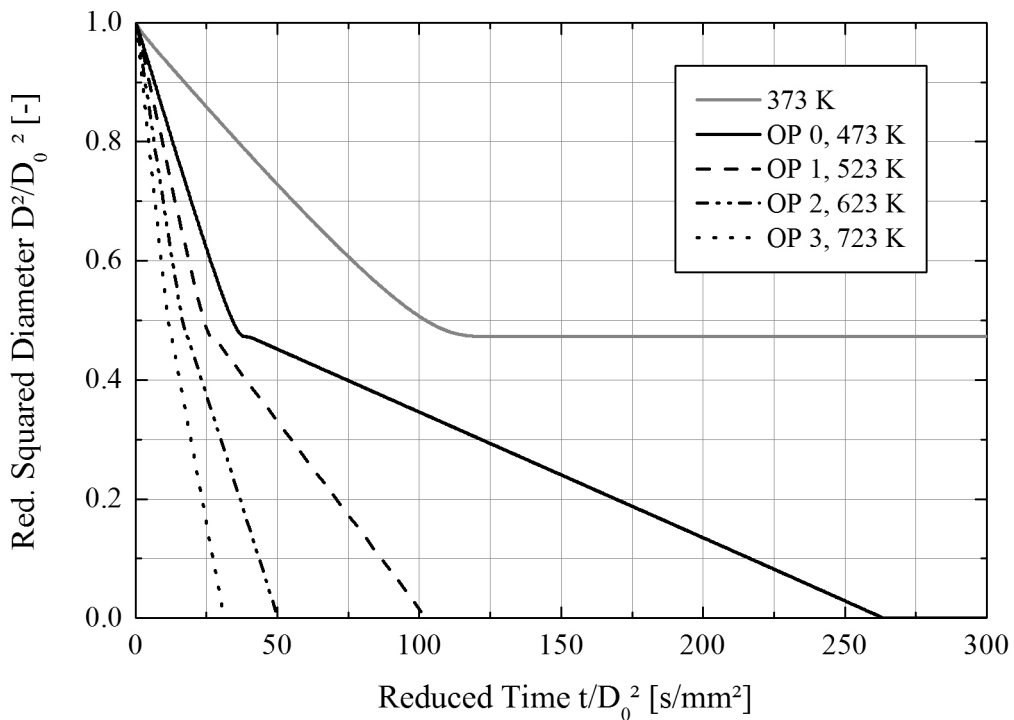
Figure 5.2:   *Transient UWS droplet diminishing process from the evaporation model for different ambient gas temperatures*

All qualitative features of a regular (no undesired secondary reactions) UWS decomposi-

tion process as reported in literature are captured by the model: the sudden change of slopes indicates the commonly accepted two-stage decomposition of water evaporation and subsequent urea thermolysis. The linear droplet surface area reduction reveals the implicit coverage of the D^2-law. In accordance with the literature, the total diminishing time of the droplet is significantly shortened with increasing ambient temperature. As described by Birkhold [17] and observed experimentally by Wang et al. [20] the differences in the diminishing rate between both stages decrease with increasing ambient temperature. At $373\,K$, urea thermolysis is completely suppressed and the droplet size reduction stagnates after the water evaporation stage. This is due to the extremely low saturation pressure of urea at those temperatures.

In accordance with the D^2-law, no dependency of the diminishing rate on the initial droplet size ($D_0 = 20 - 1000\,\mu m$) has been observed with the present model. The resulting droplet diminishing timescales for both stages as a function of ambient temperature are shown in Figure 5.3.
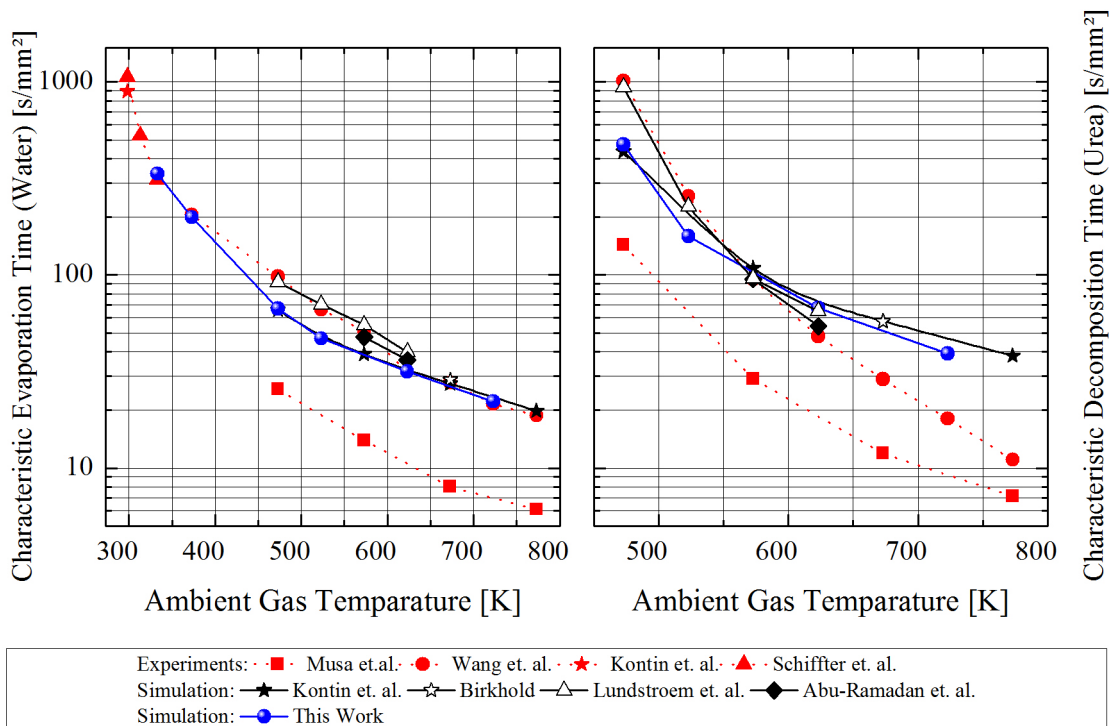

Figure 5.3: *Single UWS droplet depletion timescales of water evaporation (left) and urea thermolysis (right) as a function of ambient gas temperature: Comparison of available literature data to the present UWS evaporation model*

Results are compared to the single UWS droplet evaporation experiments discussed in the review section [19, 20, 44, 15]. As discussed there and indicated by the initial-diameter-dependent timescales reported by Wang et al. [20], the fibre experiments' outcome may be

distorted by external flows, radiation or heat conduction through the fibre. The validation of the present model is therefore extended to a comparison to available simulations of the single droplet test case [16, 31, 44, 15, 17]. The selection of considered alternative models is limited to evaporation models, as the Arrhenius type description of thermolysis is commonly regarded as less appropriate. From the proposals made by Lundström [16] only the consistent one with the thermolysis taking place in the droplet surrounding is taken into account, see discussion of Figure 2.4. The data by Kontin et al. [44] is extracted from the saturated case setup [44, 15]. From the simulations by Birkhold, only a single external temperature case ($T_{amb} = 673\,K$) could be reasonably included into the comparison. In case of Abu-Ramadan et al. [31], reviewed simulation data is limited to the temperature-independent heat of vaporization for urea and external thermolysis model, as it has been reported to be the best practice. Moreover, in the latter case only the DL model results are accounted for, for a lack of report on the RM outcome. All remaining simulation data has been gained from RM approaches. For further details, see Section 2.1.2.

Figure 5.3 reveals a general consensus in the determined trend of decomposition timescales. The significant decrease of characteristic droplet evaporation times for both decomposition stages with increasing ambient temperature is obvious. Significant quantitative deviations of the experimental data reported by Musa et al. [19] from all remaining results occur. Possible explanations for the systematic enhancement of decomposition speed in the former study have already been discussed in Section 2.1.1.

The water evaporation rates of the present model compare well with the predictions by Kontin et al. [15] and Birkhold [17] in the whole temperature range. For the remaining experimental and numerical studies a good correlation appears in the high and low temperature range. For intermediate temperatures ($473 - 573\,K$), a deviation of approx. $20\,\%$ occurs in comparison to those works. A possible explanation in case of Abu-Ramadan et al. [31] is the internal transport model. The employed RM mixing model in the present work may reduce the timescales in comparison to the DL approach. However, this explanation does not hold for a comparison to Lundström's results, who also employed a RM model. A factor that may explain the latter is the description of the background fluid heat conductivity, see Equation 2.5. Despite those deviations the overall prediction of the water evaporation stage can be regarded as sufficient for an application to UWS sprays.

The urea decomposition timescales are shown in Figure 5.3, right. In this case, the measurements by Wang et al. [20] significantly differ from available simulation data in the high temperature range and tend to the data by Musa et al. [19]. Again, the uncertainties of experimental boundary conditions have to be taken into account. Especially the reported microexplosions, see Figure 2.1, right, very likely affect the resulting thermolysis timescales in the high temperature range. The latter have not been captured by any of the considered models, but are very unlikely in significantly smaller UWS spray droplets [16].

Deviations of the present model from the data by Kontin et al. [15] are well below $10\,\%$ in the whole temperature range. This is consistent with the fact that Kontin et al. [15] employ a very similar urea thermolysis description to the present model (same saturation pressure

curve and thermolysis enthalpy based on [17]). In comparison, deviations from Lundström's data become significant for low ambient gas temperatures ($473\,K$, $523\,K$). This indicates the principle differences in thermolysis description, resulting from the insecurities of thermolysis location (at the droplet surface, like assumed in this work and by [15, 17] or in the boundary layer as proposed by [16, 31]).

Further insight into the UWS decomposition process and those model related differences can be gained from the transient droplet composition and temperature evolutions, see Figure 5.4.
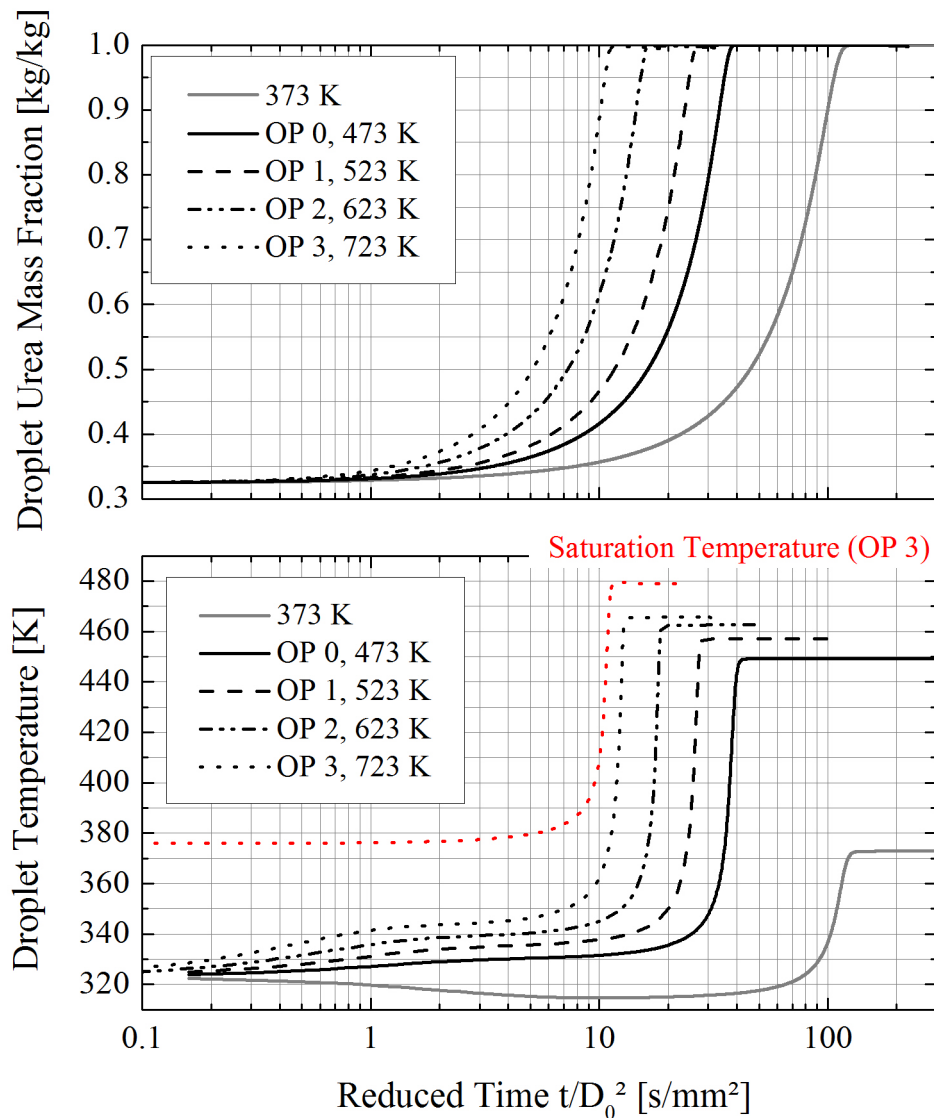
Figure 5.4:   *Simulated UWS droplet drying process (upper subfigure) and -temperature evolution for different ambient gas temperatures (lower subfigure)*

According to the present model, the droplet temperature at no time during decomposition exceeds its current boiling temperature. This can be seen from the transient saturation temperature evolution, additionally shown in Figure 5.4 for the OP3 droplet evaporation. As the saturation temperature results from the current composition of the UWS droplet, see Figure 5.1, it increases with the successive evaporation of water. At the very beginning, the standard UWS has a saturation temperature of $380\,K$, which is well above the droplet temperature during the first stage. During thermolysis, when the droplet consists of pure molten urea T_{sat} has raised to $483\,K$ [17], which is again above the current droplet temperature. Even in the transitional stage, when water has not yet fully evaporated, but the droplet temperature monotonically raises, no boiling occurs according to the present model.

Another important feature is the predicted adiabatic wet-bulb temperature, which results from a balance between heat transfer to the droplet and enthalpy loss by the vaporization / thermolysis process, see Equation 5.2:

$$\dot{m}_d^{wb} \cdot h_{vap,d} = \alpha_g \cdot (T_g - T_d^{wb}) \tag{5.2}$$

As Figure 5.4 reveals, a quasi-steady stage, where water evaporation enthalpy balances the heat flux to the droplet, is reached within a very short period of droplet heat-up or cool-down. Depending on external gas conditions, the adiabatic temperature is maintained for a certain period and ranges between $330\,K$ and $350\,K$, which is accordance to the values reported by Birkhold [17], Lundström [16] and Abu-Ramadan et al. [11]. After the drying stage, the droplet temperature increases to the higher quasi-steady value for urea thermolysis. The value ranges from $449\,K$ to $467\,K$, with an analogue monotonic increase with ambient temperature. During this stage, the adiabatic temperature is slightly above the simulation results by Birkhold [17]($\approx 455\,K$ at $T_g = 673\,K$), but well below the value predicted by the evaporation model proposed by Abu-Ramadan et al. [11] ($\approx 510\,K$ at $T_g = 573\,K$) and Lundström [16], see also Figure 5.5.

Two major model impacts explain these differences. First, in the present formulation, the thermolysis reaction enthalpy directly affects the droplet's energy balance, assuming a single step urea decomposition process. Abu-Ramadan et al. [11] and Lundström [16], in contrast, separate the urea vaporization enthalpy from the thermolysis enthalpy, assuming the latter to happen in the *gas phase* boundary layer. Second, the present model differs from the one by Abu-Ramadan et al. [11] and [16] in the vapor pressure curve assumed for urea, see Figure 2.4. Both factors affect the heat- and mass transfer, leading to a different temperature level, i.e. adiabatic wet bulb temperature, to maintain an energy- and mass transfer balance, see Equation 5.3:

$$T_d^{wb} = T_g - \frac{\dot{m}_d(p_{sat}(T_d^{wb})) \cdot h_{vap,d}}{\alpha_g} \tag{5.3}$$

As experimental temperature data of decomposing UWS droplets is not available at present, validation of the present model's predictions and the related question of thermolysis location,
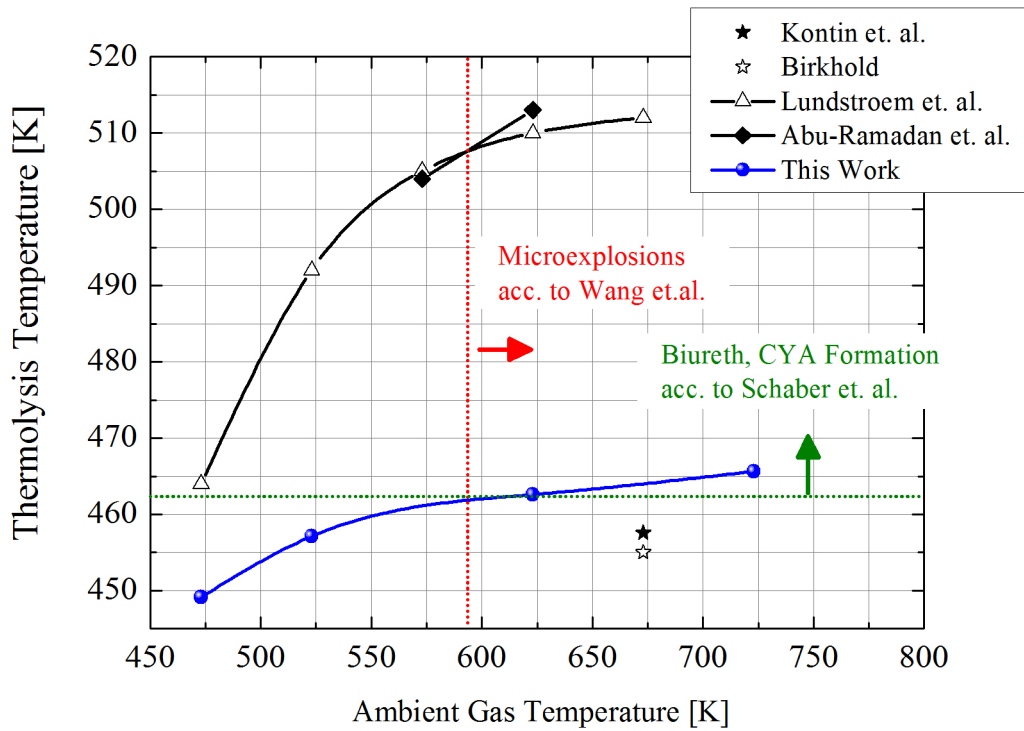
Figure 5.5: *Adiabatic droplet temperature during thermolysis as a function of ambient gas temperature: Comparison of available literature data to the present UWS evaporation model predictions*

is limited to indirect considerations:

Abu-Ramadan et al. comments that the adiabatic thermolysis temperature has to be at least $463\,K$, in order to explain the crust formation and diameter fluctuations observed in the experiments by Wang et al. [20] by the formation of biuret, see Figure 2.3 and the discussion in Section 2.1.2. Though no solidification-induced diameter fluctuations in the urea thermolysis stage can be simulated by the present model, Figure 5.5 proves, that it is capable of distinguishing between ambient gas temperatures, that should lead to crust formation (if it was modelled), and those that do not. The simulated adiabatic temperature crosses the critical value of $463\,K$, for an ambient temperature around $600\,K$. The latter corresponds to the value for the onset of significant diameter fluctuations, reported by Wang et al. [20]. This allows one to conclude that the bulb temperature predictions of the present model can be regarded as reasonable, and on this basis even allow for an extension to chemical deposition modelling.

However, it remains a matter of research to finally clarify the different predictions by Abu-Ramadan et al. [11] / Lundström [16] and the present model / Kontin et al. [44], based on the proposals by Birkhold [17].

A factor that in any case relativises the deviations observed in the single droplet decomposition studies is related to ambient conditions: The (numerical) experiments have been performed for a purely diffusive gas phase transport of evaporated species ($Sh = 2$) and heat to the droplet ($Nu = 2$), as a result of the quiescent ambience. This is no longer valid in the UWS spray application case in the SCR system. Here, convection can be expected in the droplet's surrounding due to a relative velocity between the exhaust gas and the UWS spray/droplets. The latter leads to a faster evaporation ($Sh \gg 2$, $Nu \gg 2$) and less sensitivity to the diffusive transport description in the application case.

Taking these results together, the present model offers an efficient, but sufficiently precise description of UWS droplet decomposition.

6 Simulation of UWS Liquid Phase Dynamics and Validation

Based on the validated UWS decomposition model, the liquid phase behavior and its interaction with exhaust gas and system walls is analyzed in the next modelling stage. The research aims at a validated description of spray- and liquid film dynamics and an adequate model of thermal boundary conditions. The study is limited to OP1 to OP3 from Table 4.1.

6.1 Analysis Geometry

An overview of the employed geometry that has been used in CFD simulation and, for validation purposes, on an engine test bench is shown in Figure 6.1. The figure additionally includes the measurement techniques employed, which will be discussed in Section 6.3.
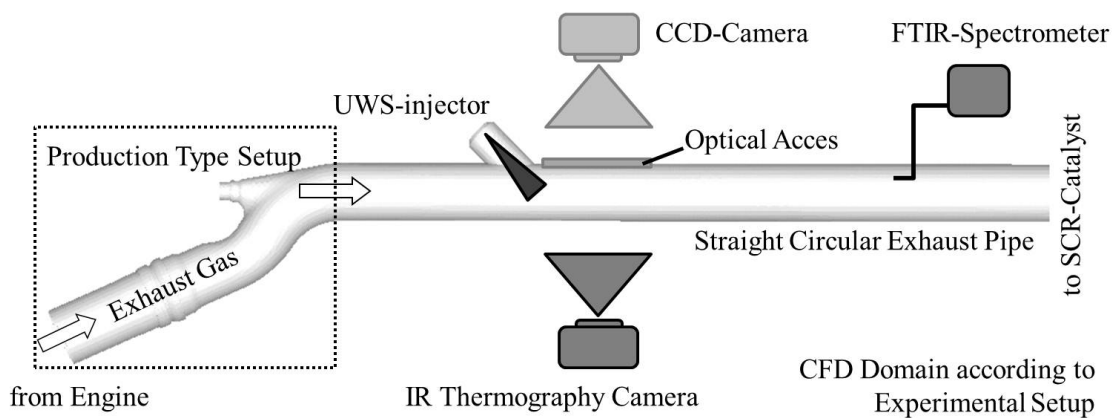
Figure 6.1: *Simplified SCR system geometry (CFD domain) and employed measurement techniques to study UWS liquid phase dynamics*

The analyzed system consists of a simple uninsulated straight exhaust pipe, which is mounted to a production type exhaust system after an s-type bend downwind of the DPF. The stainless steel pipe has a circular cross section with an inner diameter of $60\,mm$ and a wall thickness of $1\,mm$. The UWS injector position is modified from its production-type tangential injection position, to an injection in a $45\,°$- angle relative to the main flow direction. This arrangement allows for a study of spray-wall interaction, which occurs on the pipe wall facing the injector.

<u>Table 6.1:</u>   UWS spray injector specification

Property	Value	Source
Injector Type	3-hole-nozzle, jets full cone	Manufacturer
Spray Jet Half Cone Angle	$4\,°$	Manufacturer
Angle (Spray Jet - Injector Centerline)	$6\,°$	Manufacturer
Injection Pressure	$5\,bar$	Manufacturer
Average Injection Velocity	$24\,m/s$	High Speed Camera
Droplet Size Distribution	Rosin-Rammler $(x = 150, q = 2.0)$	Laser Diffraction
Spray SMD	$112\,\mu m$	Laser Diffraction

The distance between the injector position and the end of the mixing pipe is $550\,mm$.

A commercial type UWS injector has been used throughout the present study. An overview on major spray parameters is given in <u>Table 6.1</u>. The spray is released in three separate jets from a three-hole nozzle. Geometric parameters of the spray pattern are taken from the manufacturer's manual. The pin-holes are distributed uniformly (angular distance between two holes is $120\,°$) on a circle (radius $1.9\,mm$). Each spray jet has a half cone angle of approximately $4\,°$. The angular distance between the injector centerline and each spray cone axis is $6\,°$. Further spray characteristics are measured for injection into a quiescent atmosphere. The average spray injection velocity is determined with a high speed video camera. The droplet size distribution is gained from laser diffraction measurements and is in good accordance with a Rosin-Rammler distribution, see <u>Equation 6.1</u> and Table 6.1.

$$\psi(D) = 1 - \exp[-(\frac{D}{x})^q] \tag{6.1}$$

6.2 CFD Model Description

For CFD studies a computational grid of the previously described domain is created. The mesh consists of approximately $200,000$ polyhedral and hexahedral fluid cells, with a cell base size of approximately $3\,mm$. According to the mesh sensitivity studies by Bhattacharjee and Haworth [38], this grid resolution is sufficient to regard mesh impacts on the solution as negligible. Along the pipe walls, a prism layer of three cells thickness is created to capture the turbulent boundary layer. In order to model the solid pipe wall (Conjugate Heat Transfer), an additional three layer structured prism mesh of $1\,mm$ thickness surrounds the fluid domain. The upwind edge of the domain is defined as an inlet boundary, the downwind end as a pressure boundary with ambient pressure of $1\,bar$. Wall boundary conditions will be explained in

Section 6.2.4.

6.2.1 Exhaust Gas Description

Throughout the following CFD studies, the exhaust gas is represented by hot air, assuming minor differences between those fluids due to the dominance of omnipresent nitrogen. Temperature dependent fluid properties of the exhaust are therefore considered to be similar to the ones of dry air, see also implementation stage one, Section 5.2. Inlet boundary conditions for the gas flow are specified according to the exhaust mass flow and -temperature for each operating point from Table 4.1. Inlet gas density is estimated from those values assuming the ideal gas equation. Inlet velocity results from gas density, the particular mass flow and the inlet cross section.

Apart from water vapor, no additional chemical species resulting from the combustion process are considered as part of the exhaust for computational efficiency reasons. As the present decomposition model of UWS leads to active scalars for water and an ammonia vapor representative, there are only two additional scalar equations to be solved. Water vapor concentrations to specify the initial- and inlet boundary conditions to the domain are gained from FTIR-measurements [99]. An overview on boundary values is given in Table 6.2.

<div align="center">

Table 6.2: Inlet Boundary Conditions

OP	1	2	3
Exhaust Gas Inlet Temperature $[K]$	250	350	450
Exhaust Gas Inlet Velocity $[m/s]$	10	33	68
Water Vapor Mass Fraction $[\%]$	5.1	6	9

</div>

6.2.2 UWS Injection and Droplet-Gas-Interaction

As already discussed, all dispersed phase dynamics throughout the following CFD studies are modelled in a Lagrangian framework with a Discrete Droplet Model (DDM) [86]. Primary break-up of the spray is not considered due to the lack of predictivity of available models. Instead, all spray properties are defined as boundary conditions and are specified in a user defined subroutine. Geometric spray parameters are implemented according to Table 6.1. The initial velocity magnitude is regarded as identical and constant for all droplets. The initial UWS temperature is taken from [101]. Injection strategy (timing, duration, frequency) and the resulting injected spray mass is specified in accordance to the particular OP, see Table 4.1. Transient effects on the UWS mass flow and spray velocity during nozzle opening and closing are neglected.

The spray is represented by parcels of randomly chosen diameter's ($D_0 = 10 - 400 \, \mu m$), with spray mass fractions assigned to each parcels to maintain measured size distribution. The number of parcels is set to 300 per timestep ($0.2 \, ms$ during injection), leading to a spray representation with approximately $10,000$ to $15,000$ parcels per injection event, depending on the OP. The parcel number can be regarded statistically valid according to the sensitivity studies by Bhattacharjee and Haworth [38].

Interaction between the dispersed- (droplets) and continuous phase (exhaust gas) is simulated with two-way coupling for momentum and heat. Considered forces, acting on the droplets, are in agreement to the findings by Ström et al. [40]: The model accounts for drag and gravity effects on droplet trajectories. Turbulent dispersion of droplets is modelled with a state of-the art random walk model [102, 46].

6.2.3 Droplet-Wall-Interaction and Liquid Film Model

Bai Impingement Model

Droplet wall-interaction is modelled by the multi-regime Bai-model, see Figure 2.5 in Section 2.2.1 [58]. Its particular parametrization (We_a, We_s, T_s^*, T_L^*, We_1 and We_2) to capture the behavior of UWS under all operating conditions is a major task of the present work. Therefore the following study aims at a separation of the relevant regime boundaries from the less important ones and a correct calibration of the former.

Some aspects for a first calibration of the Bai-model can already be derived from current state of knowledge, for details see Section 2.2.2:

Numerous studies have indicated, that a key quantity for a predictive impingement model and liquid film prediction is the critical temperature for the onset of wall wetting (T_s^* in case of the Bai-model). Table 6.3 gives an overview on the UWS deposition limit values that have been reported from different experiments.

Table 6.3:   Standard UWS Deposition Limit Temperature (T_s^*) from Literature

Type of Study	Method	$T_s^*[K]$	Source
Droplet chain on heated Aluminium plate	optical	$516 - 546$	[17]
Spray on heated Aluminium plate	optical	508	[17]
Spray on Stainless Steel plate	temperature drop	$538 - 553$	[39]
Spray on Stainless Steel outer wall	temperature drop*	$463 - 483$	[10]
Spray on Stainless Steel mixer	temperature drop*	478	[10]
Spray on Aluminium plate	temperature drop	$528 - 533$	[17]
Attached droplet on heated Stainless Steel	droplet lifetime	$523 - 653$	[19]

Limiting the observed temperatures to impingement on stainless steel, there still remains a range from $463\,K$ to $553\,K$. Considering Equation 2.8 and a saturation temperature of $376.6\,K$ for standard UWS (see Figure 5.1), this leads to a value of B_s^* between 1.23 and 1.47. A clarifying determination of B_s^* for the present conditions will therefore be carried out by a sensitivity study and comparison to accompanying experiments.

A first rough estimation of the splashing/deposition limits (We_a, We_s) for UWS is possible from the single droplet impingement experiment by Birkhold [17], see Figure 2.8 in Section 2.2.2. The study allows a localization of the transition between $K = 98$ and 156 for a wetted wall. From the specified boundary conditions, the corresponding critical Weber numbers can be estimated to $We_s \approx 290$ and 550, the Laplace numbers to $La \approx 7798$ and $La \approx 4126$, respectively. Based on Equation 2.10 this leads to a splashing limit prefactor for wetted walls A_w between 1302 and 2760. The former is very close to the standard setup value in Star-CD (1300). A more precise determination will be part of the sensitivity studies of the present modelling stage. For dry walls, Star-CD internally determines the prefactor A from an empirical correlation with the surface roughness r_s [46]. The latter has been set to $r_s = 10\,\mu m$ for the stainless steel pipe [103], corresponding to $A \approx 2600$ [46].

As discussed in Section 2.2, impinging droplets could even lead to wall cooling for surface temperatures beyond the deposition limit (Leidenfrost) temperature [76, 85, 84]. In the current Bai-model implementation this can be covered by the droplet break-up and slide-regime, see discussion in Section 2.2.1. The implementation of zero thermal contact above T_L^*, resulting from the assumption of an instantaneous formation of a perfectly insulating vapor film, is in that sense inappropriate. From a physical point of view, the Bai-model's regimes between T_s^* and T_L^* can be regarded as a better representation of the Leidenfrost phenomenon, than the mechanism implemented beyond T_L^*. Therefore, the latter has been effectively deactivated by setting its value to a relatively high temperature ($T_L^* = 800\,K$).

As a further consequence of a missing thermal contact time submodel, both We_2 and We_a, can be expected to play a dominant role, to nevertheless cover the extent of wall cooling for temperatures above the deposition limit. Thus, a specification of We_2 has to be regarded as an empirical approach to compensate the thermal contact model insufficiency. Indications for a realistic value for the break-up limit Weber numbers We_1 and We_2 for UWS have in any case not been reported yet. Their best practice calibration will be discussed in the results section.

Liquid Film Dynamics

The two dimensional, finite volume liquid film model outlined in Section 2.2.1 is used, considering shear force, impingement momentum impact and gravity effects on film movement [60]. Moreover, the contact angle effect on film movement is activated to cover a possible stick-slip behavior according to Foucart [46]. For the lack of knowledge, Star-CD's standard tuning of the critical radius for film movement onset is used. The ejection of droplets from the film due to stripping effects is considered on sharp edges only [64]. In the smooth straight pipe, the

activation my be unnecessary, but may become relevant on more complex geometries, e.g. on mixer blade edges. Stripping, due to wave and body-force instabilities by the adjacent gas flow and gravity, are not considered, as inducing forces are expected to be below critical values for the particular flow velocities and expected thin films [65].

Thermodynamic Film Model and Nukiyama Pool Boiling Model

All thermodynamic liquid film component- and bulk-properties are passed on to the film from the validated UWS (droplet) decomposition model according to Table 5.1. The Star-CD implementation for film heat- and mass transfer employs Raoult's and Dalton's law in an analogue manner to the droplets. In contrast to the droplet's RM description, liquid film's internal species transport is taken into account in the mass transfer equation for evaporation [46]. This demands a specification of the liquid binary diffusion constant of urea in water (and vice versa). The constant has been estimated to $D_l = 1 \cdot 10^{-9} \, m^2/s$ according to the values reported by Costantino et al. [104].

Heat transfer in the boiling regime is covered by the Nukiyama pool boiling model as described in Section 2.2.1. The major challenge is its adoption to UWS liquid films with the insecurities also discussed in Section 2.2.1.

In order to cope with the numerous impact factors determining the parametrization, the following assumptions and literature findings are advantageous: First, the pool-boiling correlation for pure water is well known and a parameter set available for water on stainless steel walls. Considering the high amount of water in standard UWS, this may be a good first approximation, see the modelling approach proposed by Birkhold [17]. Second, effects from the demixing of UWS as observed for droplets, which can also be expected in the liquid film, are intrinsically covered in the current implementation of pool-boiling in Star-CD, see Section 2.2.1. Third, the attached droplet lifetime experiments reported by Musa et al. [19], see Figure 2.9, give some indications on the boiling regime boundaries.

Based on these inputs, the setup summarized in Table 6.4 is used for the UWS pool boiling model. For further information on the parameter meaning, see Figure 6.4 and [46].

Table 6.4:   Pool Boiling Model Setup for UWS

Parameter	Value	Source	Comment
Rohsenow Exponent N	2.07	[105]	water on stainless steel
Rohsenow Surface Coefficient c_{sf}	0.015	[105]	water on stainless steel
Leidenfrost Temperature ΔT_L (rel. to T_{sat})	$110K$	[66, 46]	water
Critical Heat Flux Multiplier c_{max}	0.15	[66, 46]	Star-CD default
Critical Heat Flux Range Multiplier c_S	1.2	[66, 46]	Star-CD default
Leidenfrost Heat Flux Multiplier c_{min}	0.09	[66, 46]	Star-CD default

The resulting heat transfer correlation for selected mean urea mass fractions in the film as a function of the wall surface temperature is shown in Figure 6.2.
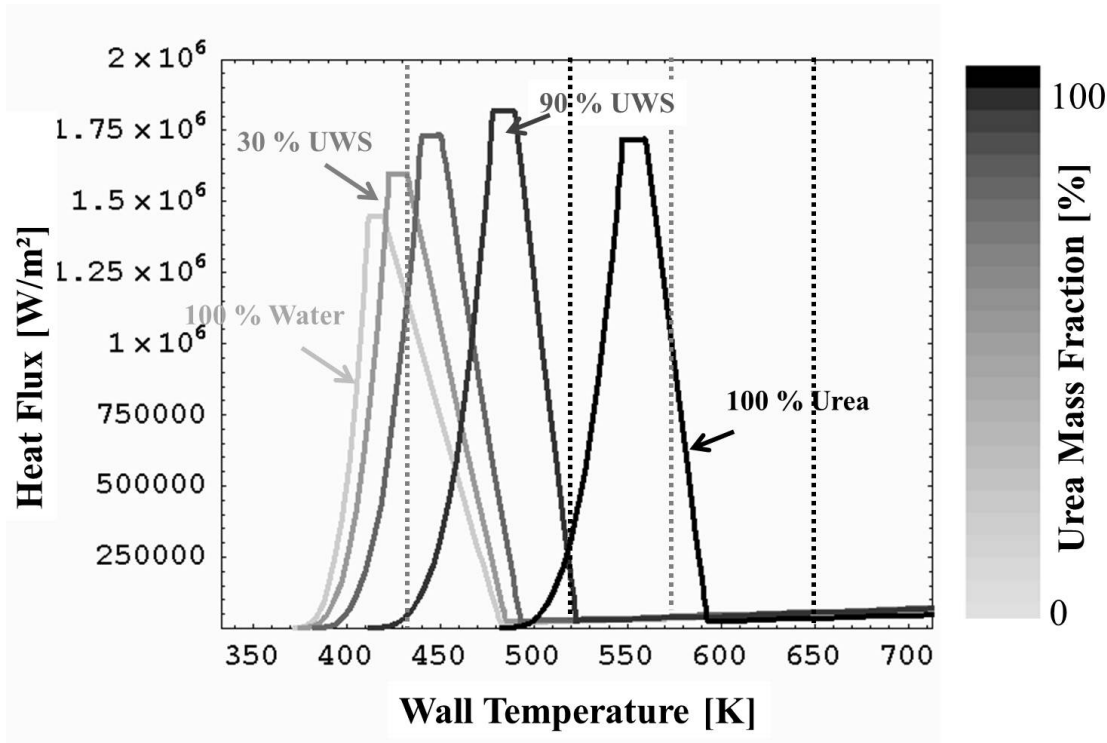
Figure 6.2: *Pool boiling correlation as a function of urea content in the UWS employed to model solid to liquid film heat transfer*

6.2.4 Thermal Solid Wall Model

As the wall temperature has to be determined correctly for a predictive droplet-wall-interaction model, the consideration of solid materials for pipes and mixing elements is necessary. In the current study, heat conduction within the solid, heat transfer from fluid to solid and the thermal mass of the solid are captured by a full conjugate heat transfer description [86]. For this purpose, the pipe walls - and in the production type system the mixing element - are covered by a solid cell mesh. In order to guarantee numerical stability, the interface between solid and fluid is meshed with a conformal grid, i.e. computational vertices coincide on both sides of the interface.

The outer wall boundaries are modelled with a free convection heat transfer coefficient, estimated according to [93] and a constant ambient temperature of $298\,K$.

6.3 Validation Measurement Techniques

Accompanying the CFD simulations, experiments have been carried out on the mentioned basic geometry to understand the behavior of UWS spray and film and validate the submodels. Optical measurements with a CCD-camera and recordings with an infrared camera are employed to analyze the wall cooling at the impact point of the spray jets. Concentration data from time resolved FTIR-spectroscopy is used to determine the reducing agent's releasing timescales from the liquid film [99].

6.3.1 Videoanalysis of Liquid Film Formation

Figure 6.3 shows the experimental setup for an optical analysis of the impingement process and possible wall film formation. The geometric setup is similar to the basic geometry from Figure 6.1, despite allowing for optical access to the impingement region. The latter is realized by reducing the pipes circumference by an angle of $150\,°$ on a length of $200\,mm$ on the opposite side of the impingement region. A high speed CCD-camera is used to record the process of wall-wetting and the dynamics of an optionally occurring liquid film for a defined time period ($120\,s$) - and therefore number of injection events - for each operating point.
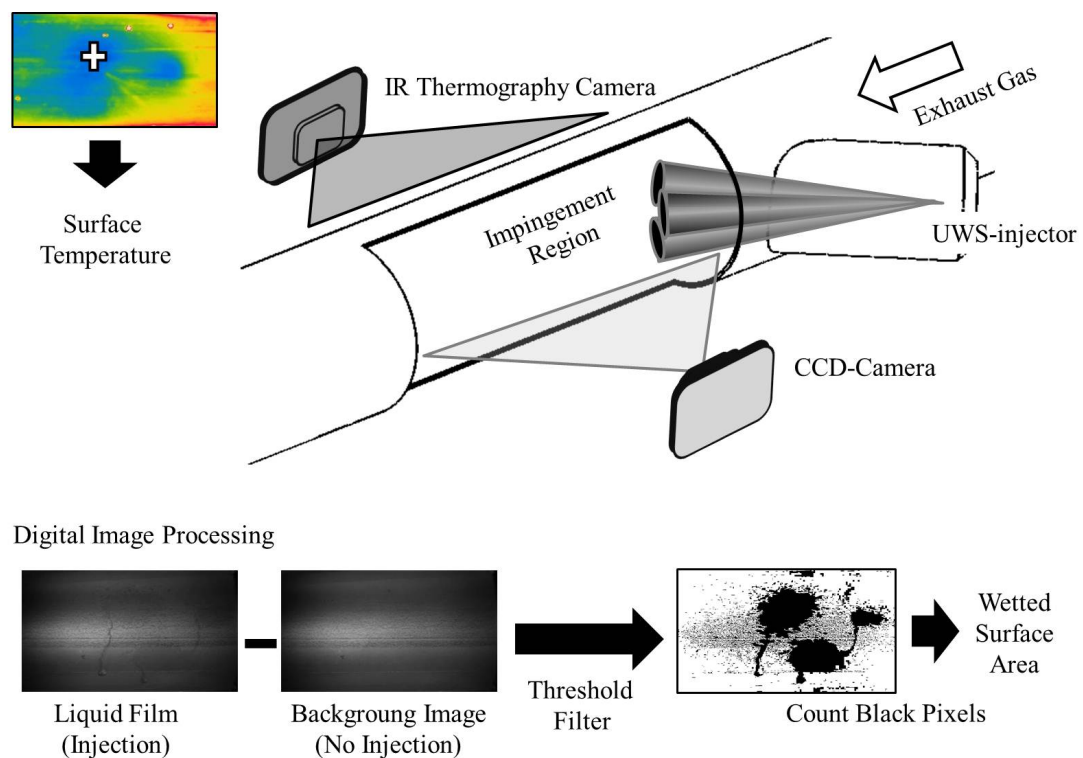
Figure 6.3:   *Experimental setup for the study of spray impingement and liquid film formation and principle of digital image postprocessing*

The records are post-processed with the digital image processing software ImageJ [106], see lower section of Figure 6.3. From each frame, the background image of the setup with dry wall, i.e. no UWS injection is subtracted. Then the wetted surface is extracted from the resulting image by a suitable threshold-filter and concerned pixels marked black. A count of marked pixels allows for an estimate of the wetted surface area - or at least its projection, as the curvature of the pipe is neglected as an approximation.

In addition to the latter, further error sources of the method result from the unavoidable noise and inhomogeneity in available light and the related particular choice of the threshold value. Especially due to the opacity of liquid film adequate illumination is a challenging task. Moreover, the flow field and therefore drag- and shear force on droplets and liquid film are very likely modified to a certain degree by the optical access. Despite these drawbacks, the procedure allows for a qualitative estimate of the wall wetting process as a function of time.

6.3.2 Infrared Thermography for Spray-Wall-Cooling

Infrared-thermography (IR-thermography) is used to simultaneously record the surface temperature at the outer pipe wall in the impingement region, see upper part of Figure 6.3. Due to the high heat conductivity and small wall thickness of the stainless steel pipe, the temperature gradient from its inner to its outer surface can be neglected to a good approximation on long time scales [17]. Therefore, the outer wall surface temperature can be regarded as a reasonable measure of the inner wall temperatures. Like the optical analysis, the wall cooling is analyzed for each operating point. Again, a defined number of injection events is performed until a steady state is reached and the subsequent recovery of wall temperature after the stop of injection is captured. To achieve a fast time-resolved recording, the thermal camera has been linked to a video system. A series of IR-Images is then extracted from the stream and the temporal wall temperature evolution determined for selected locations, especially the spot of maximum wall cooling, see white cross in thermography image of Figure 6.3.

6.3.3 FTIR-Concentration Measurements of Ammonia

Fourier-transformation infrared-spectroscopy has been used to determine the concentrations of ammonia and isocyanic acid resulting from UWS decomposition, as well as the water vapour content from combustion for inlet boundary conditions, see Table 6.2 [99]. The advantages of this method compared to dispersive infrared-spectroscopy, i.e. a spatial spectral-split by a mono-chromatograph, are the much shorter measuring times and an improved signal-to-noise quality. As a consequence, the employed device allows time-resolved measurements with a sampling rate of up to $1\,Hz$. This allows studying ammonia concentration evolution on long time scales. Upstream of the actual measuring cell, a conditioning device consisting of a pre-filter and a heating / cooling tube is assembled to maintain well-defined inlet conditions. The extraction of the exhaust gas sample stream is carried out with a probe at discrete points in the exhaust system. Each of those locations is successively analyzed by repeating the injection strategy according to the OP. By a uniform arrangement of five sampling points across the

outlet cross section of the pipe, the space averaged ammonia outlet flow can be measured as a function of time [99].

Difficulties arise from the sensitivity of the system to the presence of the liquid phase [99]. Though unprepared UWS droplets that reach the probe are separated at the prefilter and therefore do not harm the system itself, they very likely affect the data. In cases of massive liquid UWS reaching the probe, a distinction between ammonia, which is prepared within the SCR system and ammonia produced within the conditioning device, becomes impossible.

6.3.4 Probe Analysis of Liquid Film Composition

In order to determine the liquid film's water content, gravimetric and refractometric measurements have been undertaken for probes sampling from liquid film [99]. The film samples are extracted with an injection needle at different distances downstream of the primary spray impingement region. As urea is hygroscopic, immediate hermetical sealing of the probes is done to avoid the effects of the surrounding air humidity.

Gravimetry

After primary weighting, each probe is heated for $24\,h$ at $60\,^{\circ}C$, which is well below the urea thermolysis temperature, but leads to complete water evaporation. The subsequent cooling of the probes is performed in an exsiccator at underpressure conditions to avoid re-absorption of surrounding air humidity. Secondary weighting and subtraction from the primary allows for the determination of the probe's original water content. A validity check is undertaken with a pure urea probe.

Optical Refraction Index

For a cross check, analogously sampled liquid film probes are analyzed with refractometry. Reference binary UWS mixtures of well defined mass fractions are prepared and their optical refraction index is measured as a function of urea-/water-mass fraction. In order to determine the latter for the liquid film probes, they need to be redissolved with a well defined water content before the refraction measurements. This is due to the crystallization of the probes, taking place during the cooling down after extraction.

The refractive indices are then measured and compared to the calibration curve to determine the particular water content. The latter is then corrected with the known amount of water used in redissolution to determine the actual water fraction.

6.4 Results

6.4.1 Droplet-wall Interaction and Longtime Liquid Film Formation

The formation of liquid film can be expected to determine the overall UWS preparation process by an intermediate or even permanent storage of ammonia. In addition, droplets reaching the catalyst may reduce its reduction performance. Both scenarios may affect a controlled ammonia supply to the catalyst and are related to the impingement process.

Figure 6.4 shows a top view of the UWS spray simulation during injection and wall contact for all OPs. Depending on the OP, the dynamics of UWS spray changes and different wall wetting scenarios have been observed for the first UWS spray impingement event.
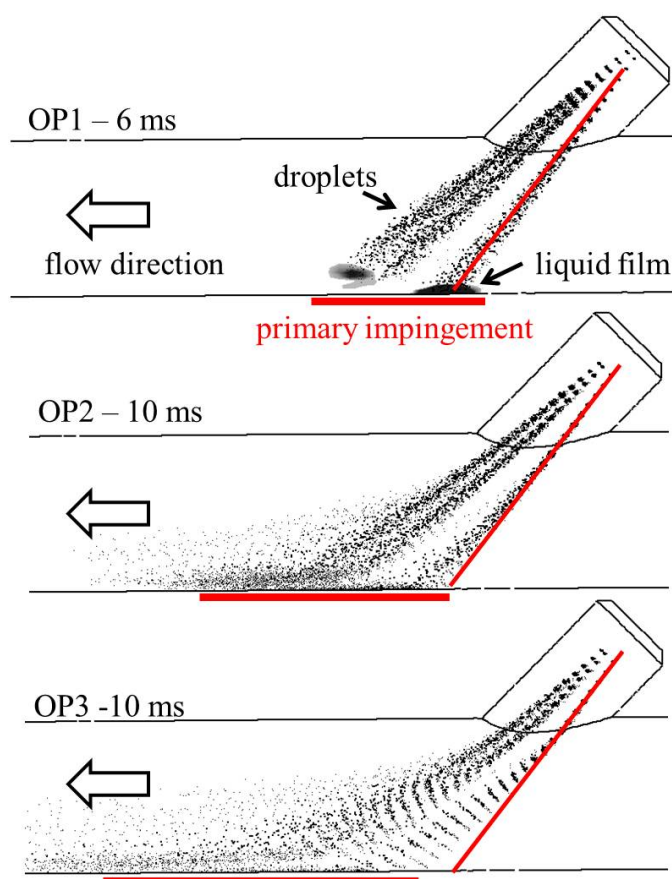
Figure 6.4: *Simulated UWS spray dynamics during injection and wall contact (Bai impingement model) for OP1 - OP3*

With increasing mass flow, i.e. exhaust gas velocity, from OP1 to 3, the three primary spray beams are carried further downstream before they hit the wall. As a consequence the impingement angle is successively reduced and the single spray beams are further spread in

the main flow direction. Moreover, the formation of a liquid film can be observed for OP1, while the formation of secondary droplets seems to dominate in case of the other OPs.

For validation purposes, Figure 6.5 shows the high speed video analysis result compared to the best practice simulation for OP1. Liquid film thickness from the CFD is grey-scaled to obtain the wetted surface in analogy to the digital image processing. In addition, secondary droplets, sliding along the wall, are included in the simulation evaluation. This allows for a better qualitative comparison, as the secondary spray leads to an intermediate shading in the image processing as it passes along the wall.

OP1,100 kg/h, 523 K, 5.6 mg/s
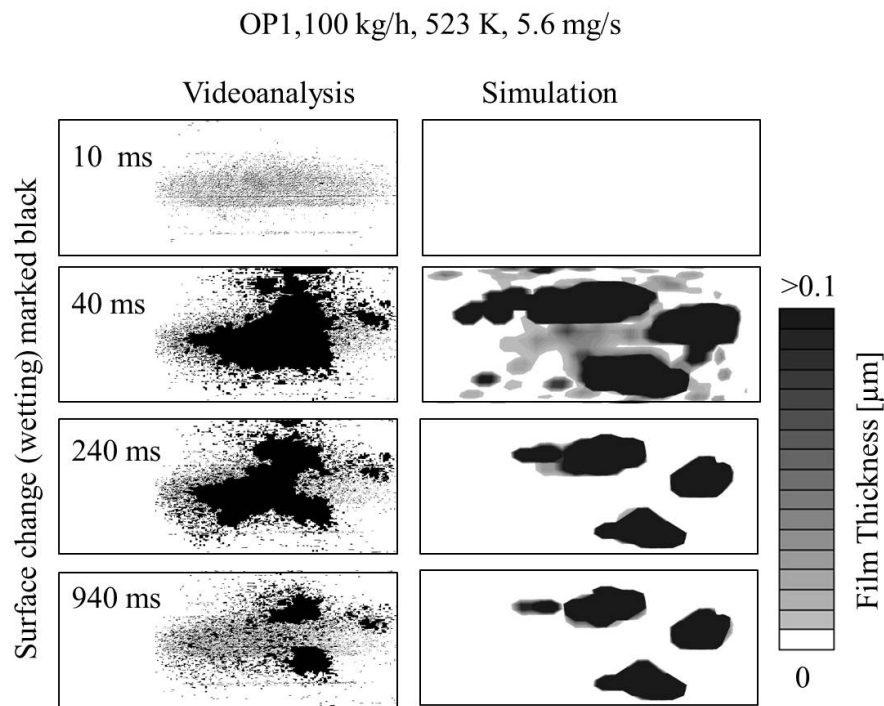
Figure 6.5:   *Measured and simulated liquid film formation at the impingement position for the first injection period of OP1*

As the figure reveals, there is a good qualitative correlation between CFD prediction and the video analysis. Immediately after the start of the injection, massive wall wetting can be observed in both cases. Three primary impingement spots, resulting from the three-hole geometry of the injector, can clearly be located. In contrast to OP2 and 3, see below, only a few secondary droplets can experimentally be observed downstream of the primary wetting spots. The same is valid for the simulation. Even at the end of the first injection period (1 *s*), the liquid film has not been completely removed by UWS decomposition from the wall, see last frame of Figure 6.5. As a consequence, the primary impingement spots are still wetted as the next injection burst hits the wall. This determines the efficiency of UWS preparation on long timescales, as will be discussed below.

Figure 6.6 shows the first impingement event for OP2 in a similar manner. In this case, experimental distinction between the spray hitting the wall without deposition and a deposited liquid film becomes difficult. In addition to wall wetting, the digital image processing detects a shading, resulting from the spray as it hits and moves along the wall.
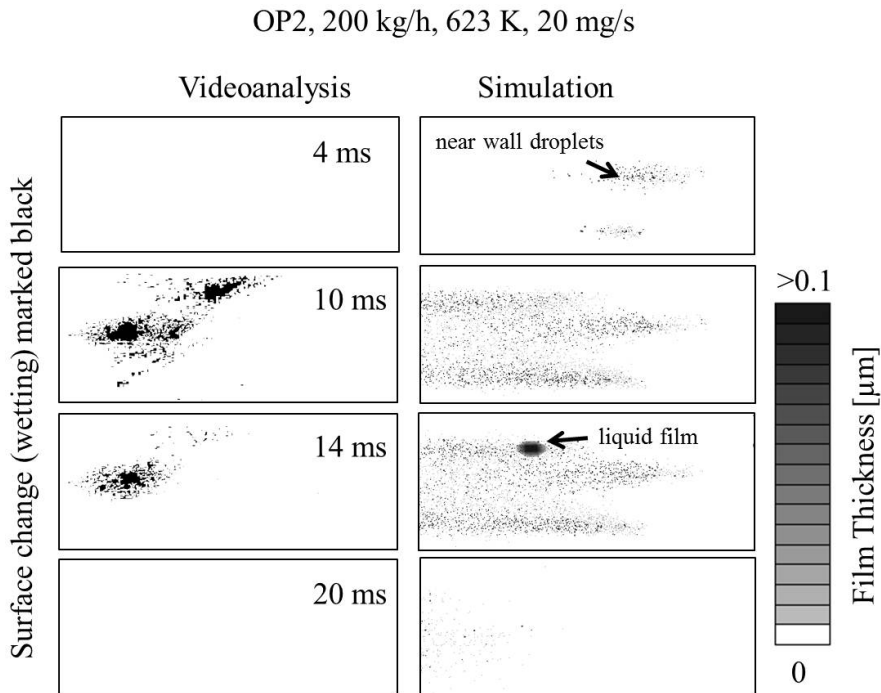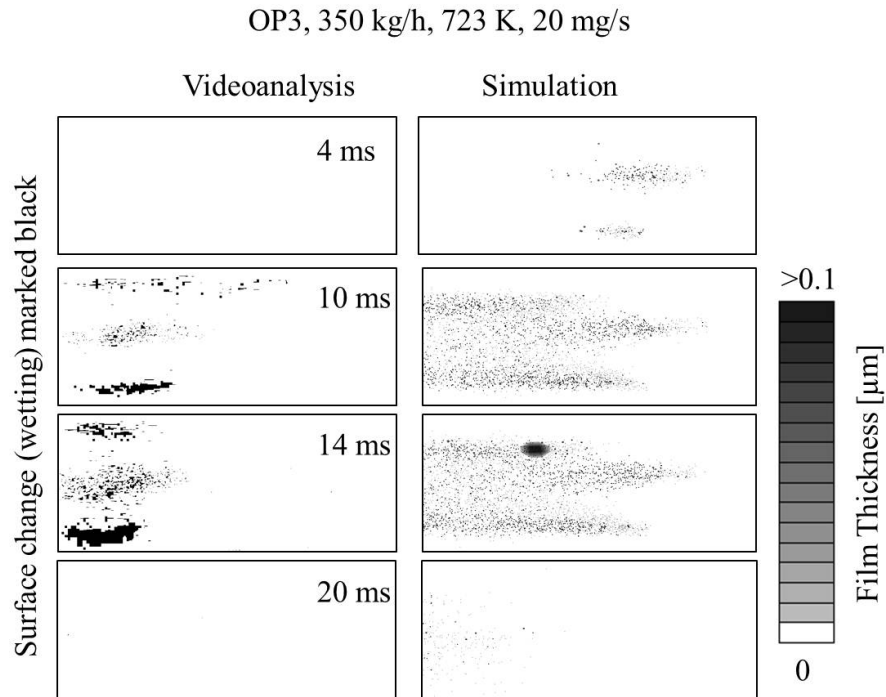

Figure 6.6: *Measured and simulated liquid film formation at the impingement position for the first injection period of OP2*

Taking the near wall droplets into account for the simulation evaluation, the qualitative results are again in good agreement. While OP1 shows the remainder of liquid phase on the wall, in OP2 only a very thin intermediate wall film is formed during the first impingement event. The maximum liquid film thickness observed in the simulation is well below $1\,\mu m$. In both, simulation and experiment, the wall is dry again after less then $25\,ms$.

An insignificant film occurs for the highest temperature OP3, see Figure 6.7. Again nearwall droplets are included in the CFD evaluation, as they affect image processing.

As the picture series reveals, the qualitative scenario is well represented by the simulation. Wall wetting - if present at all - is even shorter and less intense than for OP2. Thus, the wall is again completely dry after less than $20\,ms$.

For each OP, the injection has been maintained active for $120\,s$, to study the long time evolution of liquid film formation. The time interval corresponds to 120 injection events in case of OP1 and 360 events for OP2 and OP3. Figure 6.8 shows the resulting evolution of the

OP3, 350 kg/h, 723 K, 20 mg/s

Figure 6.7: *Measured and simulated liquid film formation at the impingement position for the first injection period of OP3*

wetted wall area as a function of time for all OPs. The measurement data results from digital image processing as outlined in Section 6.3. Therefore, the depicted film area has to regarded as the projected value (circular pipe). Simulation values take into account any wall cell, with liquid film thickness higher than $10^{-10}\,m$. In both cases, the data have been smoothed for OP1 and OP2 by a low frequency filter. Effects of the pulsed injection, leading to high frequency oscillations of the observed film area (see example in lowest subfigure for OP3) are therefore suppressed in those cases.

As the graphs reveal, wall wetting and liquid film formation follows different routes, depending on the particular OP. However, the significantly different qualitative long time behavior for the three OPs is well predicted by the CFD:

For OP1, the wetted surface area increases monotonically with decreasing rate: The remainder of liquid film after the first injection event, results in a successive accumulation of liquid in the impingement region. With each injection event, additional UWS mass remains at the wall. Due to gravity and shear forces, wall film transport can be observed, which further increases the wetted area. With increasing thermal solid-fluid contact area, the overall evaporation process gets more efficient and the film mass per unit area increase slows down. A saturated state, where the film decomposition balances the deposition of fresh UWS, is finally reached after approximately $80s$.

In case of OP2 and 3 no residual liquid film has been observed after the first injection event.
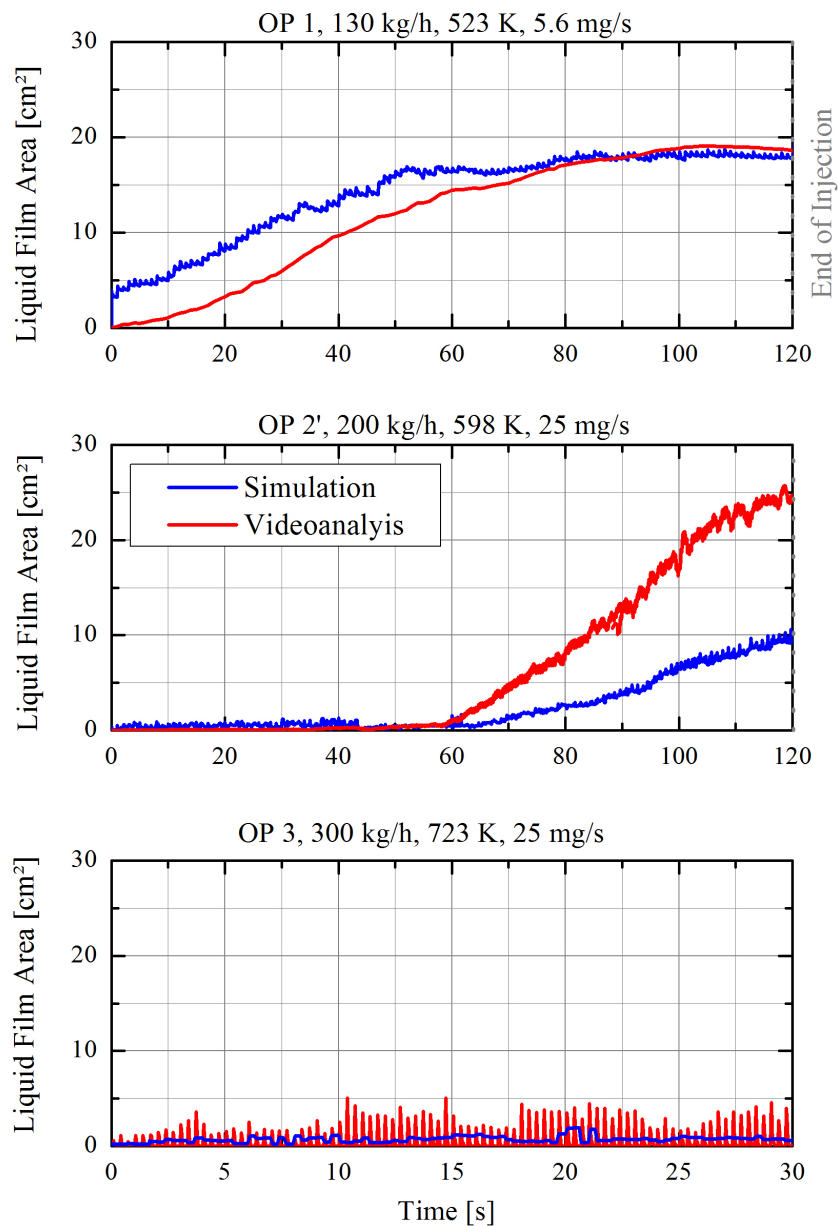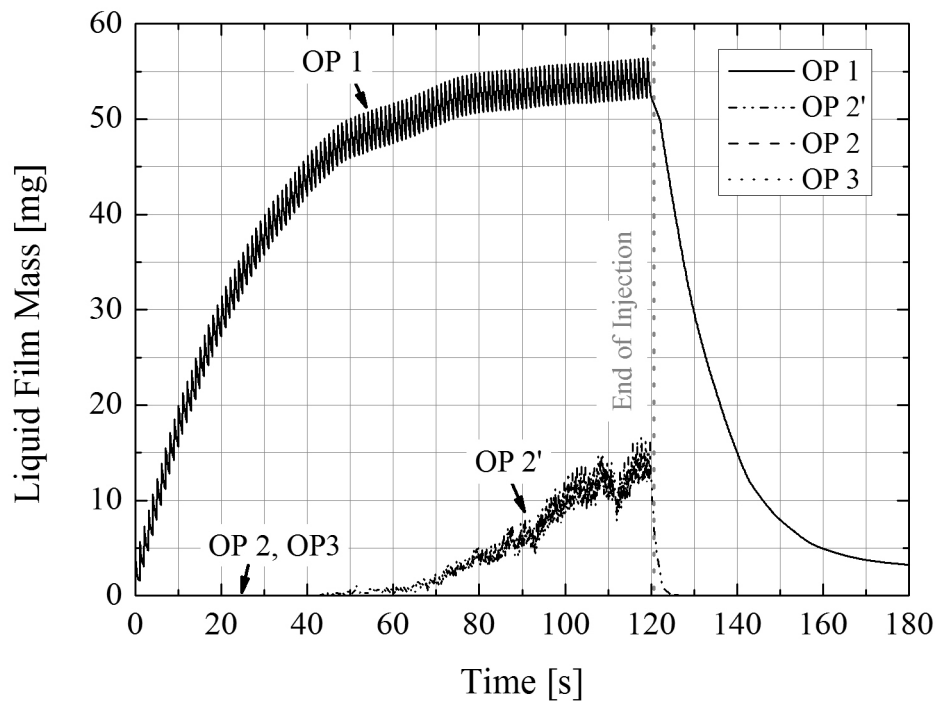
Figure 6.8: *Simulated and measured liquid film formation for multiple injection events as a function of the operating conditions. Data for OP1 and 2' is smoothed by a low-pass filter*

This is true for the complete $120\,s$ of pulsed injection. As a consequence, an oscillation of "wetted wall" (shaded) area can be observed in those cases, see lowest graphs in Figure 6.8 for OP3 as an example.

However, the scenario for OP2 significantly changes with a relatively moderate reduction of the exhaust gas inlet temperature ($598\,K$ instead of $623\,K$), keeping remaining parameters the unchanged. These conditions are in the following referred to as OP2', see middle subfigure of Figure 6.8. Though intermediate wall wetting for OP2' occurs at the beginning analogous to OP2 and 3, after approximately $60\,s$, permanent wall film formation sets in in that case. The onset of this process is well predicted by the simulation, even if the extent of sudden liquid film cumulation is underpredicted. No saturated quasi-steady liquid film area is reached in this case within the $120\,s$ period.

The corresponding simulated liquid film mass evolutions are shown in Figure 6.9.

Figure 6.9: *Simulated and measured liquid film mass for multiple injection events as a function of the operating conditions*

The trends are similar to those of the wetted surface area. OP1 shows a steep increase of liquid film mass leading to a saturated state of massive wall wetting. For OP2' a retarded sudden increase of film mass occurs. No film at all can be observed for OP2 and 3. Taking into account a total injected mass of $667\,mg$ and $3002\,mg$ UWS in case of OP1 and OP2', a maximum value of approximately $8\,\%$ and $0.5\,\%$ is stored in film after $120s$ in those cases, respectively.

Figure 6.10 shows the measured and simulated spread of liquid film for OP1 and 2' after the $120\,s$ of injection, which results from liquid film formation and its successive dynamics. The shear- and gravity driven transport of film are qualitatively well captured. Starting from
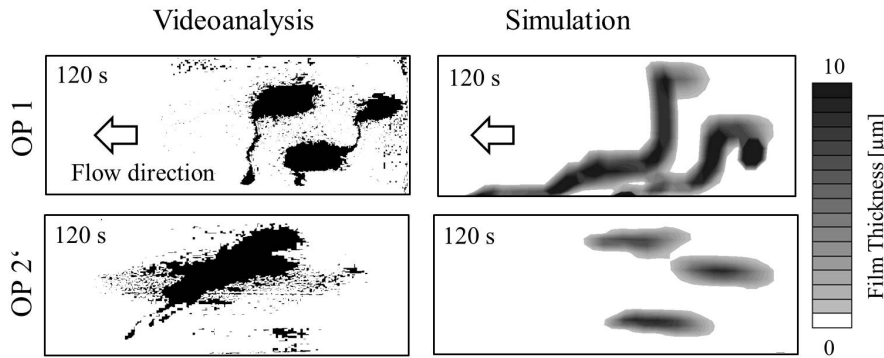

Figure 6.10: *Measured and simulated liquid film after* $120\,s$ *of injection for OP1 and 2'*

the primary impingement spots, a successive extension in the downstream- and pipe bottom-direction can be observed in both CFD and videoanalysis. In case of OP1, showing massive wall wetting, a region of increased film thickness can be observed on the downwind film edge after some time. This droplet-like trailing edge moves in a stick-slip manner and leads to an additional spread of the film. Due to the underestimation of film mass in the CFD for OP2', the film thickness does not reach a critical value for the onset of movement within the $120s$ of injection. Shear driven extension of the wetted area is therefore less obvious in that case.

Considering the number of important factors, the formation and motion of the wall film is captured in sufficient agreement with the experiment.

In order to understand the different impingement and wall wetting behaviors, relevant droplet-wall interaction regimes for the three OPs have been approximately determined and marked in the best-practice parametrization Bai-model regime map, see Figure 6.11. The particular best practice parametrization of the Bai-model to obtain the present CFD results will be discussed throughout the following results discussion. The latter has been derived from the experimental observations and the previously described literature research. A first determination of the OPs' locations on the temperature axis (wall temperature at impingement position) is roughly undertaken on the basis of inlet gas conditions. An exact determination will be discussed in the next subsection.

As Figure 6.11 indicates, the massive wall wetting observed for OP1, is principally a consequence of the relatively low wall temperature. However, in order to match the high extent of experimentally observed wall wetting, as shown in Figure 6.5, it is necessary to additionally increase the deposition/splashing limit for wetted walls We_s. A sensitivity study revealed that the prefactor A_w, see Equation 2.10, has to be increased to $A_w \approx 5000$. This is even higher than the maximum values observed during the single droplet chain impingement experiments
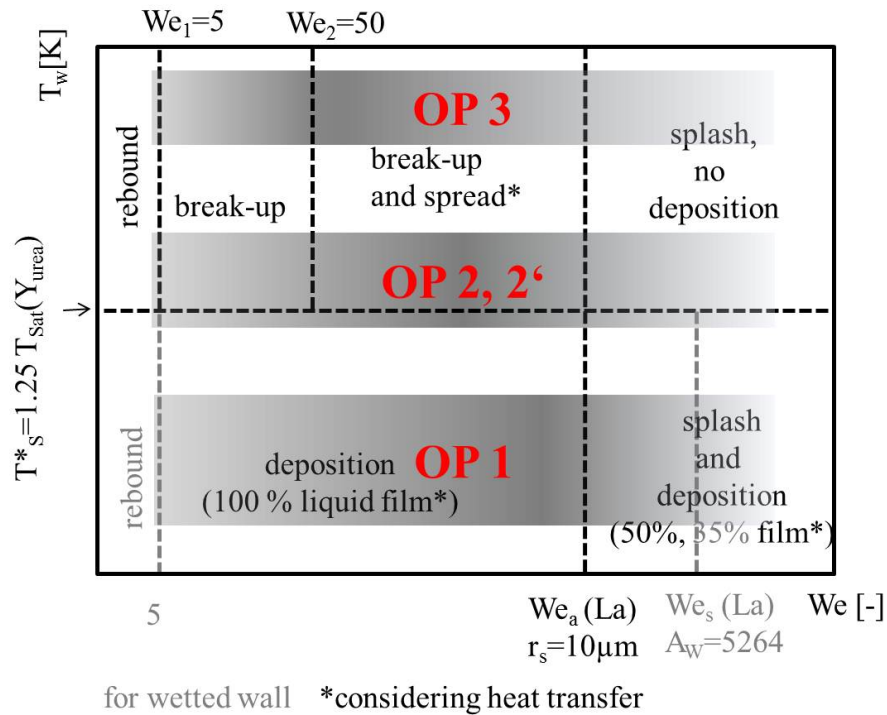
Figure 6.11: *Adopted Bai impingement model for UWS and relevant regimes for operating points OP 1, 2, 2' and 3 (schematic)*

by [17], see Figure 2.8. Moreover, this parametrization leads to $We_a < We_s$, i.e. splashing becomes less likely if the wall is wetted. A possible physical explanation that may justify this semi-empirical calibration might be urea's highly hygroscopic nature. As will be shown in Section 6.4.3, the liquid UWS gets demixed very quickly, leading to a nearly pure and thin urea film. The latter may therefore tend to soak up fresh UWS from the impinging droplets, thereby resolving the concentrated urea under the avoidance of secondary droplets. Splashing, as typically observed for a water or fuel puddle, may therefore be altered in case of a highly concentrated UWS.

In contrast to OP1, OP3 is well above the deposition temperature T_s^*. This coincides with the observation of no (permanent) wall wetting. Moreover, the break-up and spread regime, leads to droplets sliding along the wall. The video analysis delivers indications for such a behavior.

For OP2 / OP2' a definite regime determination from a rough Bai-model estimation is not possible. The observed sudden onset of liquid film formation in case of OP 2' indicates its location near the deposition limit temperature. A precise explanation for the observed impingement mechanisms is in this case linked to an exact evaluation of transient wall temperatures. This will be discussed, together with the related adoption of We_1, We_2 and T_s^*, in the following subsection.

6.4.2 Spray-Wall-Cooling Process

The impingement process and subsequent liquid film evaporation/thermolysis from the wall leads to a local cooling of the structure. Heat conduction within the solid structure counteracts this subsequent cooling process. Both effects are captured by employing a CHT model for the solid wall. Depending on the OP, a steady state wall temperature drop can be observed after the analysis period of $120\,s$. As an example, Figure 6.12 shows the resulting steady state outer wall temperature distribution for OP1 in the impingement region.
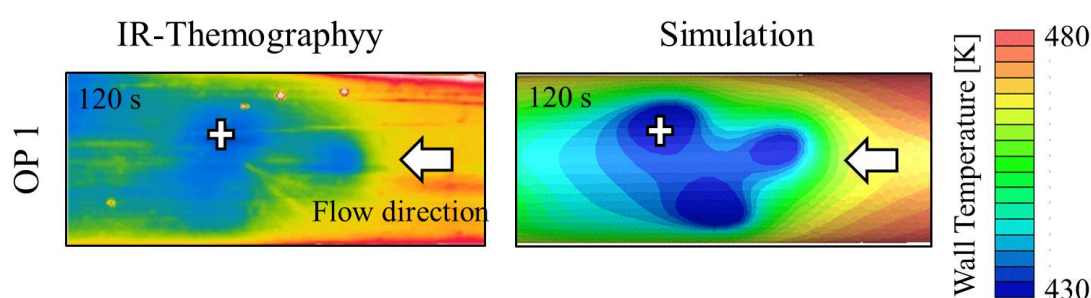
Figure 6.12: *Measured and simulated wall temperature distribution in the impingement region after $120\,s$ of injection for OP1*

A good correlation can be observed between the simulation and IR-thermography results. According to both, CFD and measurement, the major cooling is limited to the three primary impingement locations. Despite the liquid film dynamics, which lead to a spreading of the thermolysis location, see Figure 6.10, no significant cooling can be observed further downstream. A major reason for this observation is the rapid evaporation of water at the impingement position. As will be proved from the liquid film composition analysis (see next subsection), water is completely evaporated from the UWS immediately at the impingement locations. Due to the relatively high latent heat for the water evaporation stage, a high local cooling results. In contrast, the urea thermolysis reaction effects are less definitely located, due to the liquid film spread, and the lower thermolysis rates and -enthalpy. The downstream thermolysis is therefore balanced at a higher solid temperature level by internal heat conduction within the solid.

In order to further validate CFD results, the transient development of the pipe wall temperature is evaluated at the location with highest cooling for each of the three operating points. The latter coincides with one of the three primary impingement spots for all OPs for the discussed reasons. An evaluation of simulated wall temperature is undertaken at the corresponding solid cells of the pipe wall mesh. The results from thermography and simulation are shown in Figure 6.13.
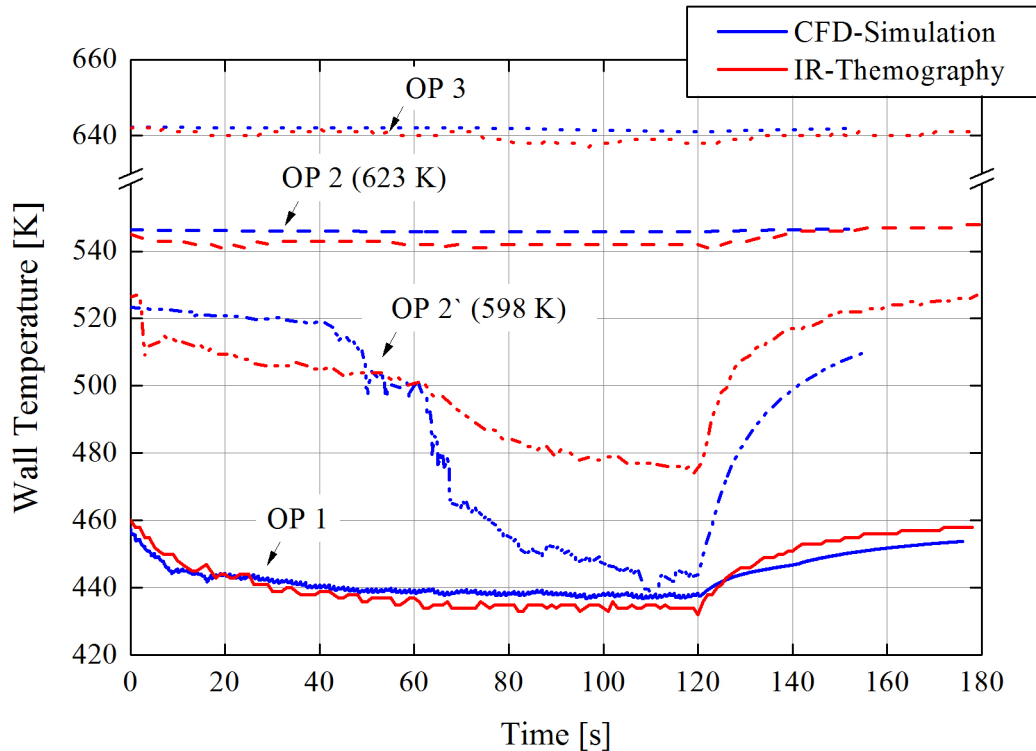
Figure 6.13: *Simulated and measured transient wall temperature at the maximum spray cooling location (impingement region) for all OPs*

For OP1, excellent prediction of the transient cooling process can be seen. The immediate formation of liquid film coincides with an instantaneous onset of wall cooling. After approximately $60\,s$, a balance between evaporative cooling and internal heat conduction within the wall is reached. This leads to a maximum wall cooling of approximately $25\,K$. Considering the employed Nukiyama pool boiling model from Figure 6.2, the surface temperature is located between the nucleate pool boiling and CHF region, depending on the particular urea content (see next subsection).

For OP3, nearly no decrease of the wall temperature occurs throughout the whole $120\,s$ of UWS injection. This observation allows to conclude that the initial wall temperature of $640\,K$ is well above the Leidenfrost temperature for UWS and stays above throughout the (numerical) experiment. This is in accordance with any reported literature data of the Leidenfrost temperature for UWS, see also Table 6.3. As the amount of injected UWS is relatively low and thermal contact - though present - is relatively moderate, complete recovery of the surface temperature is possible in between two injection events. Both, the Bai impingement model and the Nukiyama pool boiling model have been parameterized such that this experimentally observed behavior can be reasonably captured by the CFD.

The latter adjustment has been carried out by considering the transient cooling for OP2

and OP2': Though the injection rate is the same in both cases, the available heat from the exhaust is no longer sufficient in the latter case to fully compensate evaporative cooling of the structure by heat conduction along it. As a consequence, a successive small decrease of wall temperature occurs at the impingement position, though the temperature is still above the Leidenfost value. As the initial wall temperature for OP2' appears to be close to the deposition limit temperature for the impinging UWS in that case, the spray cooling is finally sufficient to reach a critical wall temperature after approximately $60\,s$ in the experiment. Coinciding with the formation of a permanent liquid film, see Figure 6.8, a significant temperature drop occurs from that point on. The latter nearly saturates after another $60\,s$. As discussed in Section 2.2.2, this cooling behavior can be explained with the impingement and Nukiyama pool boiling characteristics and has already been observed by Birkhold [17].

In order to cover these experimentally observed phenomena by the present model, the following calibration steps were necessary: First, the heat contact of sliding droplets with the wall (Bai regime break-up and spread) had to be employed to capture the temperature gradient above the deposition limit. A good correlation has been reached by adjusting We_1 and We_2 to 5 and 50, respectively. Second, the observed onset of deposition has been used to calibrate the deposit limiter B_s^* from the Bai-model. The presented best practice CFD results have been gained for $B_s^* = 1.25$. This leads to an onset of liquid film formation at $T_s^* \approx 520K$, which is within the range reported literature values, see Table 6.3.

However, as the graphs for OP2' from Figure 6.13 reveal, quantitative deviations occur in this case. In particular the long-time maximum temperature drop is overpredicted by the CFD. This corresponds to an underprediction of the observed liquid film area, see Figure 6.8, middle. Both observations indicate an overestimation of the liquid film decomposition rate for OP2' at the impingement position. This may be the consequence of a currently still insufficient parametrization of the UWS Pool boiling curve, see Table 6.4, required in order to better represent the thin-film evaporation. Further calibration may be an issue of future research.

Despite the quantitative deviations, all qualitative features of the experimentally observed wall temperature evolutions can be captured by the CFD for all OPs. Considering the nonlinear nature of the process, the model's output can therefore be regarded as promising, though further adaptation may improve predictivity. The results for OP2 and OP2' indicate that small changes of the exhaust gas temperature or injection rate induce significant differences in the extent of wall film formation. In this context it is worth emphasizing that correct prediction of the wall film and impingement behavior for all operating conditions can only be achieved with a transient calculation of the wall temperature. Only by taking into account the heat capacity and heat conductivity of the pipe walls via the CHT approach, could those effects be captured by CFD. An adiabatic or constant temperature wall boundary condition does not allow for any transient wall cooling. A 1-dimensional heat conduction through the wall model does not allow for wall parallel heat conduction and the consideration of the structure's thermal inertia. A numerical sensitivity study proved that all of these simplified wall description approaches significantly alter impingement and finally UWS preparation predictions.

6.4.3 Liquid Film Composition

The decomposition model results of single isolated UWS droplets proves that water evaporation occurs much faster than urea thermolysis. As shown in Section 5.1, the wide spread in the particular saturation pressure curves leads to a drying of UWS droplets before ammonia is released from pure urea.

A similar behavior can be observed for the liquid film: Figure 6.14 shows the transient evolution of the average liquid film urea content from the CFD simulation. The results for OP2 and 3 can be regarded as irrelevant as no appreciable liquid film is formed in that case.
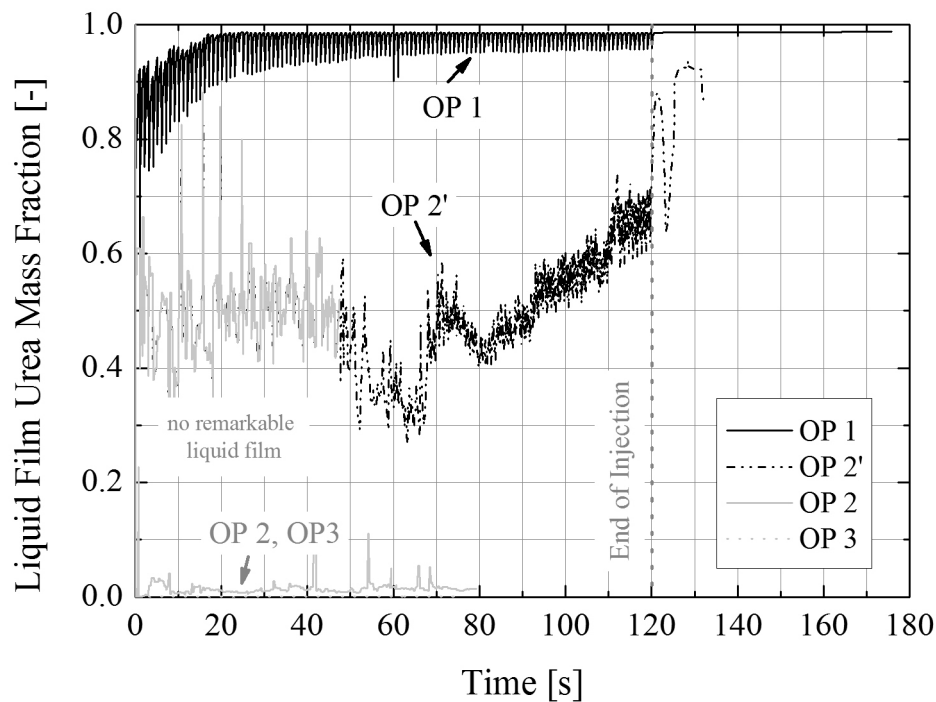
Figure 6.14:   *Simulated transient liquid film urea mass fraction for all OPs*

As the curves reveal, successive demixing of the UWS film can be observed for OP1. Immediately after the first injection event, a urea mass fraction of 80% can be observed within the film. With ongoing increase of the liquid film mass, this value further increases on average. With each injection event, an intermediate reduction in the overall urea mass fraction occurs, which results from the deposition of fresh standard UWS to the existing wall film. The fast drying however limits the region of appreciable water content to the primary impingement spots. Any liquid film further downstream of the impingement position consist of nearly pure urea for OP1 according to the simulation. This can be seen from Figure 6.15.

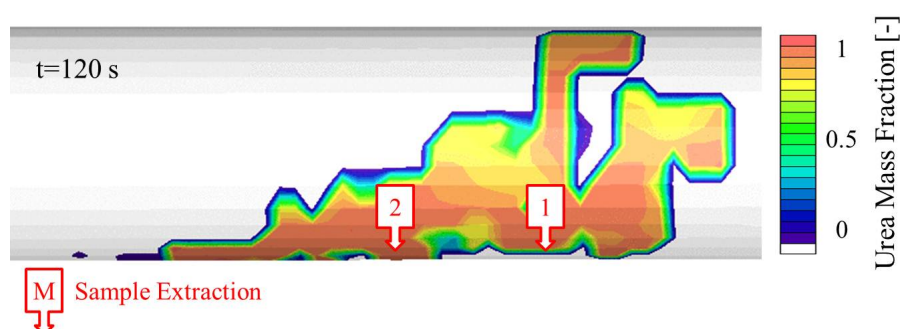For OP2', the evaluation of urea mass fractions becomes reasonable as a permanent liquid

Figure 6.15: *Urea mass fraction within the liquid film after* 120 *s for OP1*

Table 6.5: Gravimetric and refractometric determination of the liquid film's urea content

Sample extraction position, see Figure 6.15	1	2
Mass fraction urea grav.[%]	99,25	99,2
Mass fraction urea refract.[%]	99,5	99,6

film occurs, i.e. after approximately $60\,s$. Again, successive demixing, interrupted by standard UWS impingement, can be observed. However, a less concentrated UWS can be observed after $120\,s$ of injection, as the liquid film is primarily limited to the impingement region. In addition, the saturation pressures of water and urea narrow, as the wall- and therefore liquid temperatures are higher for OP2'. Thus, the thermolysis and evaporation rates differ less in this case.

The numerical predictions for OP1 are in good accordance to the laboratory film analysis. As Table 6.5 proves, both the gravimetric- and refractometric analysis reveal a similar high urea mass fraction of the liquid film. The corresponding probe extraction positions are marked in Figure 6.15.

In order to guarantee that the extracted liquid film indeed solely consists of urea and water, and no alternative undesired decomposition products are present within the film, a NMR analysis has additionally been carried out [99]. No deposit compounds, like CYA, Biuret, etc. have been found in that analysis. Considering the low temperature level, see Figure 6.12, and the reaction mechanism according to Schaber et al. [22], a pure urea melt for OP1 appears reasonable.

This may be different for OP2, which lies within the second reaction regime (see Figure 2.3), enhancing the probability of secondary deposit reactions. However, no probe analysis data is available for OP2 at the current time. Literature reports indicate that deposits in this case consist of a mixture of biureth, CYA and undecomposed urea , which corresponds to the observed temperature range for OP2 in the present work.

6.4.4 Ammonia Buffering by Liquid Film Formation

The previous results prove that a significant amount of ammonia is stored as unprepared urea within the liquid film for a certain period in case of OP1 and 2'. In order to quantify the retardation in ammonia release, transient FTIR concentration measurements of the reducing agent have been conducted at the pipe outlet according to the method outlined in Section 6.3. The data is compared to the CFD prediction of transient ammonia outlet flow, see Figure 6.16.
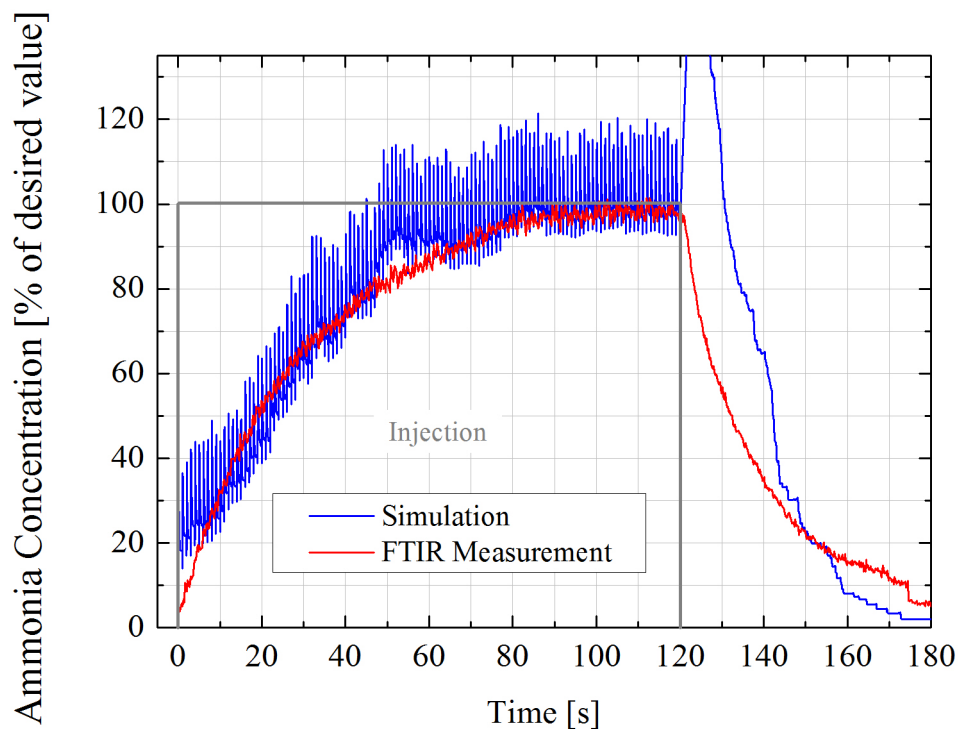
Figure 6.16: *Retarded release of ammonia due to liquid film formation in terms of the pipe outlet concentration evolution , OP1*

Due to the sensitivity of concentration data to UWS droplets reaching the probe section, the comparison has to be limited to OP1. For both variants of OP2 and OP3 the FTIR measurement has been disturbed by secondary droplets reaching the system. For OP1, a good correlation between CFD predictions and FTIR measurement can be observed during injection: At the beginning of the injection period, a significant fraction of urea / ammonia remains intermediately stored within the liquid film. As a consequence, ammonia available at the pipe outlet is significantly below the desired dosed value. With the film mass and surface area rising, the total evaporation rate and in consequence the concentration of the reducing agent at the pipe outlet monotonically increase. After approximately $80\,s$, when the film mass and surface saturate, the ammonia release also reaches a steady state value. Now the film surface

area has become sufficient for evaporative ammonia release from the film to balance ammonia storage of injected UWS within the film. However, after the end of injection ($120\,s$), the buffering effect of the wall film becomes obvious. In both CFD and experiment the supply of the reducing agent at the pipe outlet (catalyst intake) ends more than $60\,s$ after the injection has been stopped.

Under real transient vehicle operating conditions, this behavior is unacceptable for a proper dosing control of the reducing agent. As the present study proves, careful control of the wall film extent and in particular the avoidance of permanent wall wetting, is imperative for the design of a production type SCR system. This may be promoted by insulation of outer pipe walls to avoid significant structure cooling. Moreover, the integration of an internal evaporation enhancer, e.g. a static mixing element exposed to the exhaust gas and UWS spray, is an efficient measure to reduce deposit risk, as will be pointed out in Section 7.

6.4.5 Computational Effort

The present study proves that the evolution of a steady state in an SCR system may take up to minutes in time scale due to the inertia of liquid film formation and thermal processes. As shown in the previous sections, the presented longterm CFD studies allow for a comparison to available measurement data. On this basis, a calibration of liquid phase submodels has been possible. However, each of the presented numerical long time runs, even with the measures described in Section 4, takes approximately $14\,days$ of computation if parallelized to reach approximately $100,000$ cells per node. An evaluation of multiple injections during an industrial development process, including a more sophisticated system geometry, is therefore currently a very computationally extensive issue. However, the presented results allow a detailed insight into long term processes and important lessons can already be gained from a single injection event calculation on their basis.

Nevertheless, further performance increase should be a future research topic. This may e.g. be realized by the deactivation of flow solvers during the transient run or alternative, yet unknown, performance measures.

7 Ammonia-Homogenization in Turbulent Swirling Flow

Based on the validated UWS decomposition- and liquid phase dynamics model from the previous stages, the mixing of gaseous ammonia vapor in the turbulent exhaust gas is examined. The impacts of turbulence modelling, the description of scalar transport and the UWS liquid phase dynamics are studied. The SCR system examined in this modelling stage can be regarded as a state-of-the-art passenger car SCR mixing section. Therefore, the following results are of general validity for any industry type UWS based SCR system. Simulation results are again validated by measurement results from an engine test bench [8].

7.1 SCR-Mixing-System Geometry

Figure 7.1 shows a sketch of the SCR system geometry that has been used throughout the study. The CFD domain covers the exhaust line from downstream of the DPF to the outlet pipe of the SCR catalyst. This includes the UWS injector location, which is integrated into a pipe bend to realize tangential injection of the UWS spray. The spray again is produced from a three hole nozzle, geometrically similar to the one from the previous studies, but with an SMD of $140\,\mu m$. It is directly targeted onto the center of a static swirl mixer (see close up in Figure 7.1). The downstream mixing section changes from circular to an oval/flat cross section for packaging reasons and leads - after a bend - smoothly into the SCR catalyst. The mixing length from mixer to catalyst inlet is approximately $950\,mm$.

The CFD mesh consists of approximately $2.1\,Mio.$ computational cells, including about $0.4\,Mio.$ solid cells for the mixer and pipe walls, to model their thermal behavior with conjugate heat transfer. The SCR catalyst is modeled with a structured hexahedral mesh to apply a porous medium description [38]. The remaining geometry is meshed with polyhedral cells. No mesh independence study is conducted. Instead, the cell base size is chosen at a base size of approximately $3\,mm$, which leads to a cell count typical for an industrial development process. The base grid size is in accordance to the findings by Bhattacharjee and Haworth [38] regarding mesh insensitivity. Local refinements are undertaken in the mixer region. An extrusion layer covers the near-wall regions throughout the geometry, to allow correct simulation of the turbulent boundary layer.
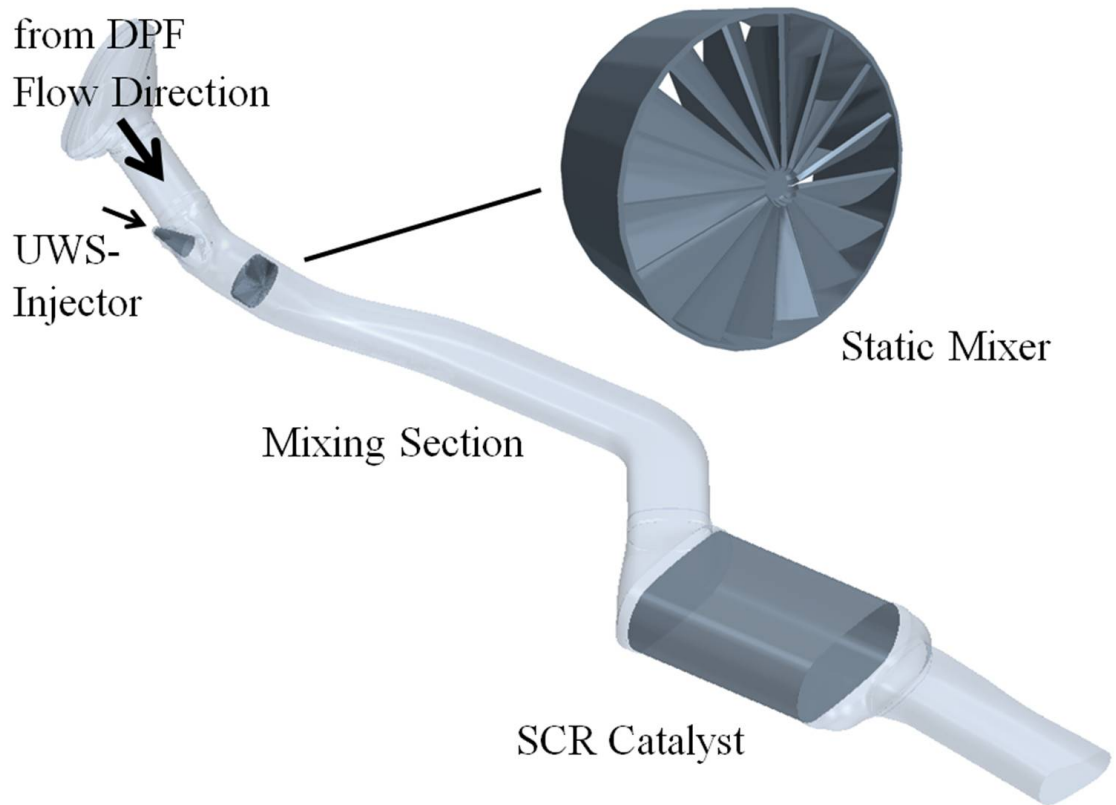
Figure 7.1:   *Analyzed passenger car SCR system geometry (and covered CFD domain) including a static swirl mixer*

7.2 CFD Submodel Description

As outlined in the literature review, there is a lack of knowledge on an adequate choice of turbulence modelling and (numerical) scalar transport description in SCR mixing systems. So far, reported studies have been limited to k-ε-models (Section 2.4) and the impact of numerical spatial discretization has not been conclusively studied. Based on the theoretic findings on scalar mixing simulation (Section 2.3), a selection of submodel setups is systematically analyzed, to identify their impacts on ammonia mixing.

7.2.1 Turbulence Model and Spatial Discretization Schemes

Table 7.1 gives an overview on the turbulence models and numerical spatial discretization setups employed.

The choice of turbulence models is restricted to RANS formulations. The use of a LES- or even DNS model currently cannot be regarded as suitable for the computer aided design of SCR systems, due to the computational effort required. From the chosen models, only the

Table 7.1:   Analyzed turbulence models and numerical spatial discretization schemes

Setup No.	Turbulence Model	Differencing Scheme (Pres., Mom., Turb., Scalars)
1	k-ε-RNG	Upwind (1st order)
2	k-ε-high Re	Upwind (1st order)
3	k-ε-RNG	MARS (2nd order)
4	k-ε-high Re	MARS (2nd order)
5	RSM - Speziale	MARS (2nd order)

RSM accounts for anisotropy in velocity fluctuations that can be found between the main flow direction and normal directions in a turbulent field. As a consequence, the RSM is expected to be more expensive, but also more precise, especially in the expected strong swirl flow, generated by the mixing element [87]. The two analyzed derivatives of the k-ε-models differ only slightly in their dissipation description [86, 46].

With respect to numerical description, the results of ammonia homogenization are compared for a first- and a second order discretization scheme. To keep the complexity of the study to a reasonable level, the same scheme is - for a given simulation run - applied to all transport equations (i.e. momentum, pressure, turbulence and scalars). First order is realized by the upwind differencing scheme (UD). For second order differencing, Star-CD provides the MARS scheme as a state-of-the-art multi-dimensional second-order accurate differencing scheme [86, 46]. It operates in two separate steps. In the reconstruction stage, a set of monotone gradients are computed with a multi-dimensional Total Variation Diminishing (TVD)-scheme [46]. The cell flow properties and the gradients completely define a second-order accurate spatial discretisation. The reconstructed cell-face flow properties are then used to compute the face fluxes for all advected properties using a monotone and bounded advection scheme [86].

Despite these details on turbulence model and numerics, the exhaust gas is modelled in analogy to the previous model stages, see Section 6.2.1.

7.2.2 Scalar Transport Model

The scalar transport for ammonia is modelled according to the theory outlined in Section 2.3. Thus, convection, turbulent and molecular diffusion is accounted for. Scalar properties are the same as described in Section 5.1. The turbulent Schmidt number is chosen on its default value of 0.9 as a first choice, but a sensitivity study is additionally carried out.

7.3 Postprocessing- and Validation Methodology

Postprocessing Methodology

The following methodology is implemented using the postprocessing capabilities of Star-CD to compare results from the different model setups and quantify possible differences in their predictions: For equidistant cross sections along the mixing pipe, the mean value and uniformity of the parameter of interest is determined and plotted versus pipe length. As an example Figure 7.2 shows the velocity magnitude distribution on sections along the pipe.
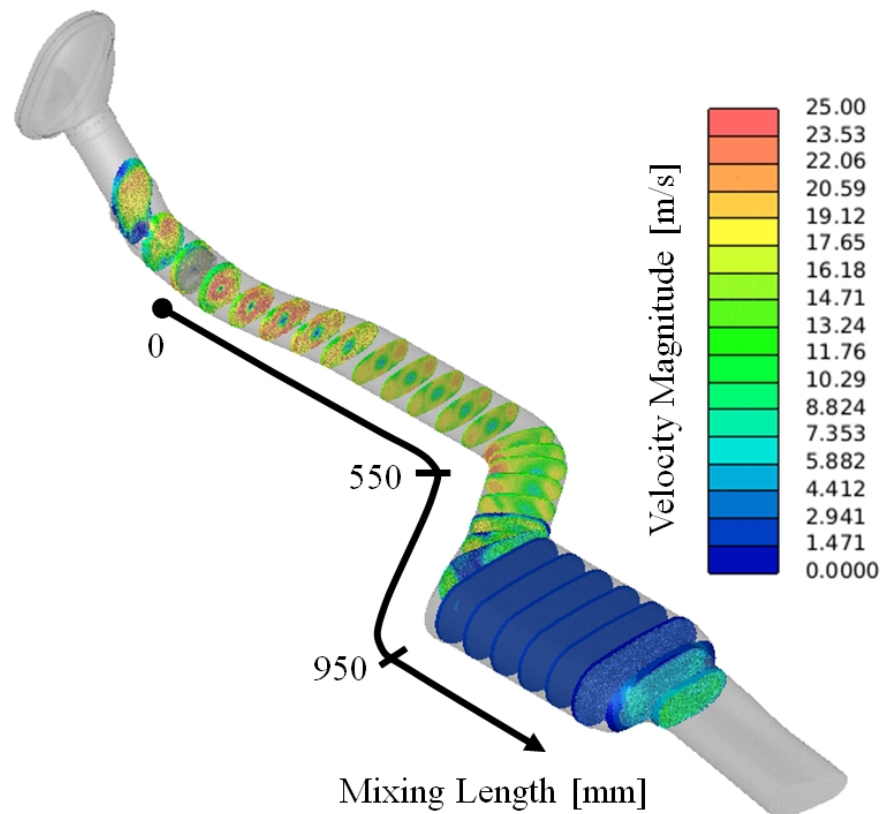
Figure 7.2: *Evaluation cross sections and mixing length definition along the SCR system, exemplarily shown for velocity data*

The mixer center is set as the origin of the length scale. The mean value of any property's distribution Y_i (e.g. velocity, ammonia concentration) is calculated as follows (Equation 7.1):

$$\overline{Y_{sect}} = \frac{\sum_{i=1}^{N} A_i Y_i}{A} \tag{7.1}$$

A_i is the area resulting from the intersection of the computational cell i (with property value Y_i) and the current cross section. A similar area weighted concept is used to evaluate the properties homogeneity with the uniformity index UI (Equation 7.2):

$$UI = 1 - \frac{\sum_{i=1}^{N} A_i \sqrt{(Y_i - \overline{Y_{sect}})^2}}{2A\overline{Y_{sect}}} \qquad (7.2)$$

During the transient simulation, ammonia is continuously produced from the decomposition of liquid UWS. In order to interpret the transient homogenization of ammonia, its vapour concentrations are time-averaged for each computational cell over the period of one injection interval. Thus, a quasi-steady distribution of ammonia is determined.

In order to allow a relative comparison between the OPs, the section mean values $(\overline{Y_{sect}}$ are normalized by the theoretical steady state concentration $\overline{Y}$ for each OP. The latter can be determined from the ratio of exhaust gas mass flow and the UWS injection mass flow.

$$\overline{Y} = \frac{M_{Exhaust}}{M_{urea}} \cdot \frac{0.325 \cdot dm_{UWS}/dt}{dm_{Exhaust}/dt} \qquad (7.3)$$

This estimation is justified, if the average transport velocity of ammonia vapour along the exhaust system is identical to the average exhaust gas velocity. Though this is a good first approximation, as there is mainly convective transport of ammonia, slight deviations may occur. Moreover, the equation considers an equimolarity of educt urea and product ammonia during the thermolysis reaction, see Equation 1.1.

Raise of Validation Data [7, 8]

To verify the CFD simulation results, measurements of the ammonia homogeneity at the catalyst intake plane have been carried out at the IFA on an engine test bed [7]. The exhaust system has been coupled to a 4-cylinder diesel engine. To determine the distribution of ammonia, the nitrogen concentration is measured with a chemo-luminescence detector (CLD) upstream of the SCR system and at discrete locations on the catalyst outlet. By calculating the local NO_x-reductions along the SCR catalyst from those values, the ammonia distribution upstream of the catalyst is determined. This methodology assumes a perfect homogeneity of NO_x upstream of the catalyst. The latter can be regarded as fulfilled in good approximation, considering the long upstream path from the engine via the DPF to the SCR catalyst.

To avoid dilution with fresh air, the probes are inserted into the closed system. The 12 measurement locations are distributed uniformly over the cross section. Short insulated tubes are mounted to a heated gas switching unit, which is connected to the CLD through a heated line. A detailed description of the measurement technique can be found in [7].

7.4 Impact of the Turbulence Model, Discretization Scheme and Schmidt Number

For each of the five cases summarized in Table 7.1 a steady state simulation of the turbulent flow field is first carried out. The example of Figure 7.3 shows the basic features of the average flow field along the exhaust system as predicted by the RSM for OP1. The streamline colour represents the local velocity magnitude. The depicted features have in general been observed for all submodel setups.
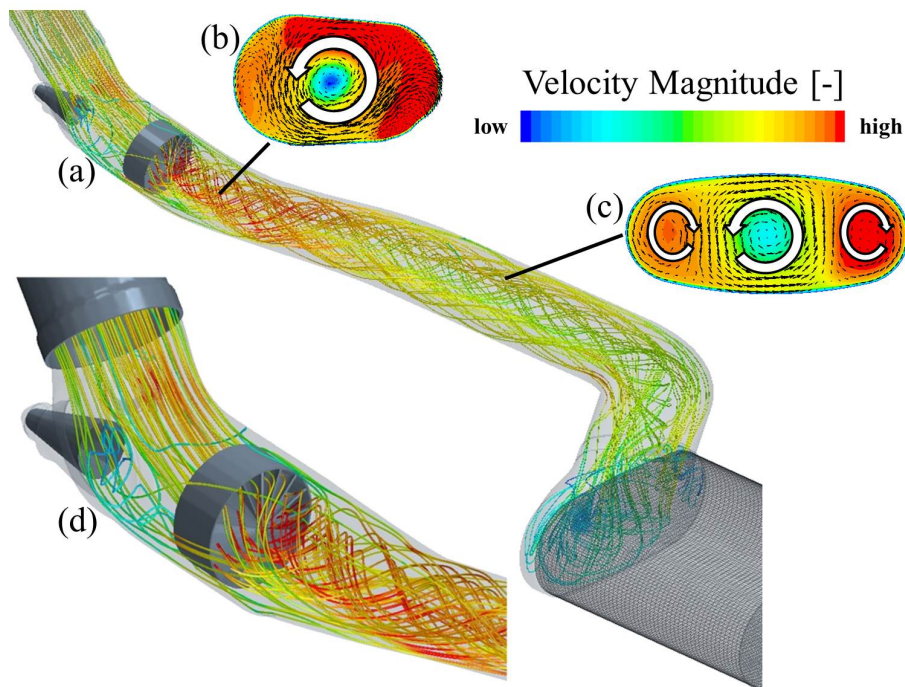
Figure 7.3:   *Swirl flow characteristics, representatively shown for OP1*

The most characteristic feature of the system's flow field is the swirl, generated downstream of the mixing element, see Figure 7.3. This swirl breaks down to three vortices due to the flattening of the pipe cross section and the circular gap between the mixer and the tube wall. Another characteristic feature common to all submodel results is the recirculation in the catalyst inlet cone. Despite these qualitative consistencies between the results from the different submodel setups, differences occur in the quantitative flow field and turbulence predictions and the details of flow characteristics. This will be discussed in the following subsections.

7.4.1 Mean Flow Field

Based on the method described in Section 7.3 the cross sectional average velocity magnitude has been quantified on the sections depicted in Figure 7.2. Figure 7.4 shows the mean velocity

magnitude along the exhaust system for all five model setups. The positions of the mixer and catalyst are marked grey for a better orientation.
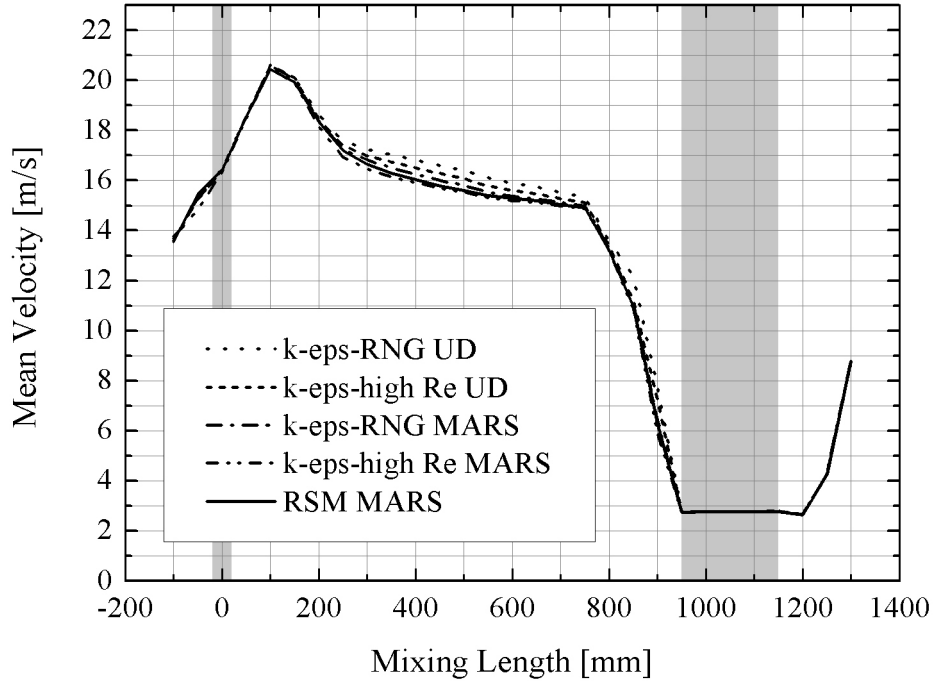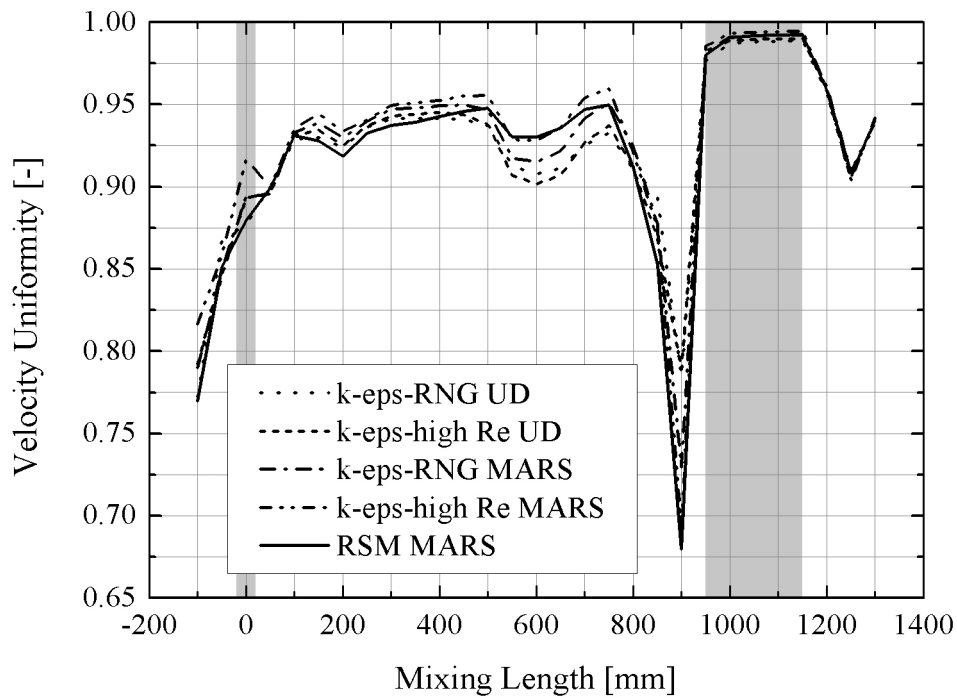

Figure 7.4: *Mean velocity magnitude on sections along the exhaust system under variation of the model setup, mixer and catalyst position marked grey*

As can be seen from the picture, all turbulence model/scheme combinations show the same qualitative velocity characteristic, in agreement with [87]. The highest velocity magnitudes are reached in the circular pipe region immediately downstream of the mixer. Neglecting turbulence and dissipation effects in first approximation, the successive decrease of the average velocity level further downstream results from the increase of the pipe cross section. Accordingly, the drop of velocity upstream of the catalyst ($750\,mm$ to $950\,mm$) is mainly a consequence of the continuous cross section increase in the inlet cone. The main quantitative differences between the submodels can be found as the secondary vortices evolve, which accompany the primary swirl, see Figure 7.3 (i.e. $400\,mm$ to $500\,mm$ downstream of the swirl mixer). Maximum deviations in this region are around $6\,\%$, with the RSM and k-ε-high Re model with MARS predicting the lowest velocities, the k-ε-RNG with UD the highest. An explanation for this observation lies in the different predictions of transfer from kinetic- to turbulent kinetic energy. Details on this mechanism will be discussed in Section 7.4.2.

As for the mean value, the different model setups lead to slightly different predictions in the velocity magnitude uniformity index. For its determination see Equation 7.2. Nevertheless, all setups maintain the same qualitative trends. This can be seen from Figure 7.5.

Figure 7.5:   *Velocity magnitude uniformity on sections along the exhaust system under variation of the model setup*

Due to the porous medium approach, covering the channel cross section, a high flow homogeneity can be observed in the catalyst brick ($950\,mm$ to $1150\,mm$). Further upstream, the curves reveal a positive impact of the swirl mixer on the velocity magnitude uniformity. The introduced angular momentum leads to a comparably high level of uniformity ($UI \approx 0.95$) in the mixing section. The symmetry and in consequence the high homogeneity is however disturbed by the pipe bend ($600\,mm$) and significantly by the catalyst inlet diffuser ($900\,mm$). Within the latter, the UI of velocity drops to $0.7 - 0.8$ depending on the particular submodel. These differences are discussed in more detail in the following subsection.

7.4.1.1 Catalyst Inlet Cone Recirculation Flow

Figure 7.6 shows the calculated velocity fields in three vertical sections through the catalyst inlet cone for the five model setups. All of the turbulence model/differencing scheme configurations predict a flow recirculation in this region. However, the regions of reverse flow differ

in size and position for the different setups. Altogether, the RSM predicts the most extended recirculation volume in the catalyst inlet diffuser, which can also be observed from the velocity uniformity drop at $900\,mm$ in Figure 7.5. A very likely explanation for this observation is the stronger coupling of flow regions perpendicular to the main flow direction that is exclusively implemented in the RSM [87].
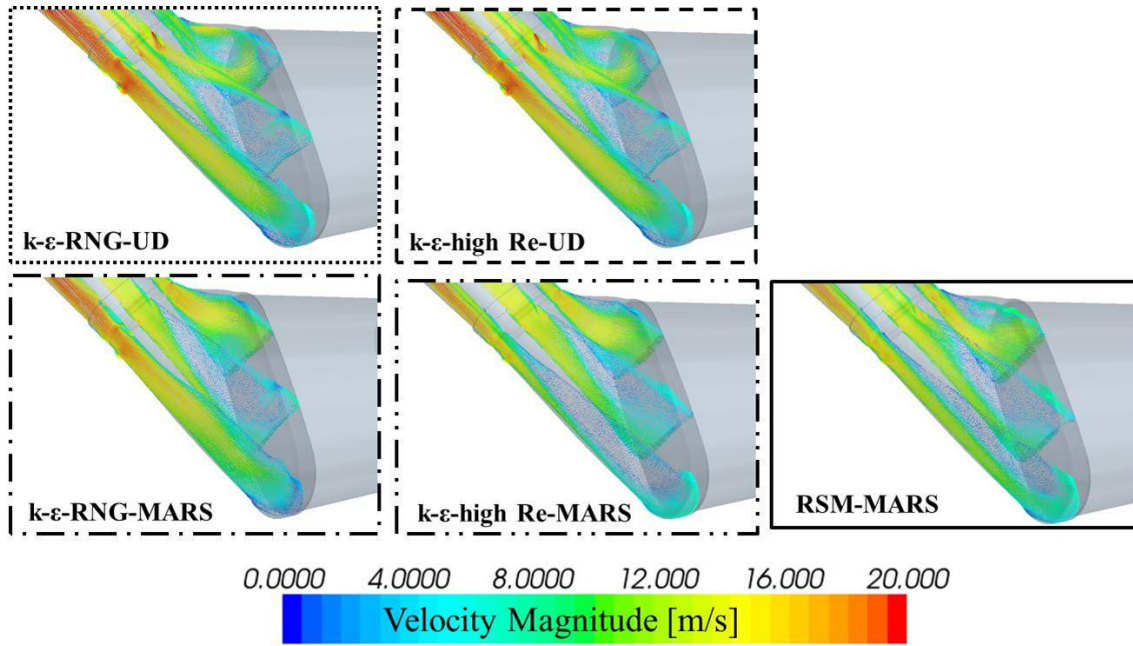

Figure 7.6: *Flow separation in the catalyst inlet cone under variation of the model setup*

7.4.1.2 Swirl Flow

Zhang et al. [91] have pointed out that a swirling motion is expected to strongly influence the homogenization of ammonia vapor, even far down the mixing section, due to the stability of large vortex structures. In order to characterize the secondary flow structure evolution in the present configuration, Figure 7.7 shows the tangential velocity vectors on pipe cross sections, downstream of the mixer. The results for the RSM / MARS configuration are depicted as examples. Immediately downwind of the mixer, significant in-plane velocities of the order of the main flow occur. With increasing distance from the mixer, the swirl core is accompanied by two secondary, counter rotating vortices on both sides, as already indicated in Figure 7.3.

In order to compare the results regarding the swirl flow on a quantitative level, a characteristic swirl number is introduced according to Beer and Chigier [107]:

$$S = \frac{tangent. angular momentum}{radius \cdot axial momentum} = \frac{2\pi \sum_{i=1}^{N} \rho_i w_i u_i r_i^2}{2\pi R \sum_{i=1}^{N} \varrho_i w_i u_i^2 r_i} \tag{7.4}$$
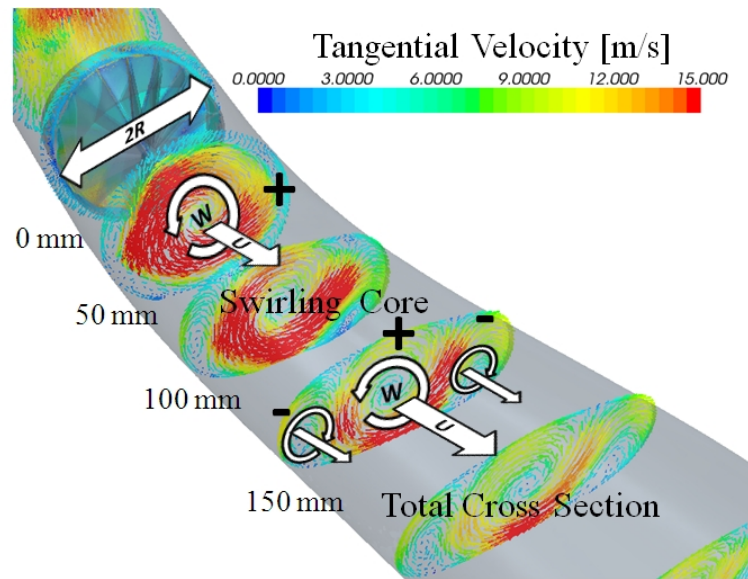
Figure 7.7:   *Secondary swirl flow structure on sections downwind of the mixing element*

This swirl number compares the angular momentum of the flow (perpendicular to main flow direction) to its axial one (in main flow direction). Following the methodology of section 7.3, the number is determined on the sections shown in Figure 7.2. The resulting value is plotted in Figure 7.8 for each total pipe cross section (grey graphs), and a reduced circular cross section, with a radius similar to the mixer's (black curves). The latter is introduced to separately analyze the inner swirl core. A positive swirl number in the diagram means a counter clockwise rotating flow and vice versa, see also Figure 7.7.

The curves prove that all turbulence model/numerical scheme variants predict the same swirl strength immediately downstream of the mixing element. However, the predictions start to differ further downstream, especially when the secondary counter rotating vertices start to develop. Though the inner swirl core loses angular momentum in all cases, the strength of the effect depends on the particular model setup. The decay of the swirl core is most significant for the RSM, and least steep for the UD cases. In turn, the swirl for the total cross section reaches the highest absolute value for the RSM, which is negative due to the lever of the near wall counter rotating secondary vortices. This observation again indicates the stronger coupling of flow regions, perpendicular to the main flow direction, that is, from all models analyzed, only intrinsic to the RSM's anisotropic formulation.

7.4.2 Turbulent Properties of Flow Field

While the mean flow field determines the convective transport of the scalar, the mixing on small length scales is directly linked to the vortex structures that are described with the turbulence models. Therefore, turbulent properties will be discussed in detail in this section.
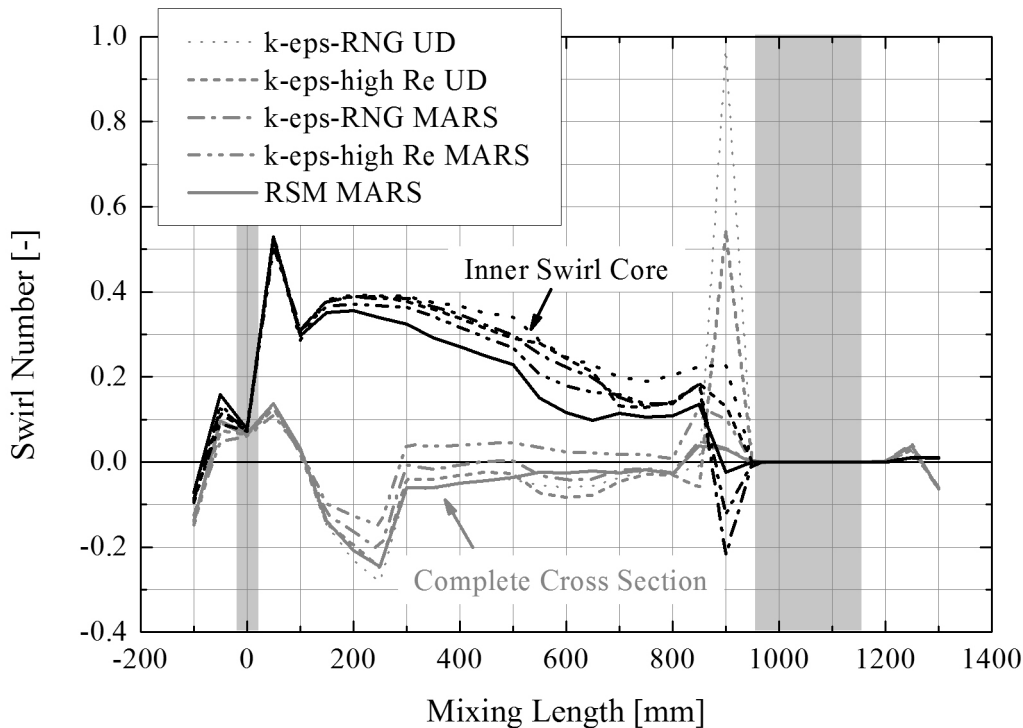
Figure 7.8: *Swirl number on sections along the exhaust system under variation of the model setup*

7.4.2.1 Turbulent Kinetic Energy and Dissipation

The turbulent kinetic energy (TKE) is an important input to determine the turbulent viscosity and on this basis the turbulent diffusion, see Equations 2.15 and 2.16. Figure 7.9 shows the mean TKE on cross sections along the exhaust system.

A feature common to all TKE curves is the local maximum in the inlet cone of the catalyst ($900\,mm$). This is a result of the earlier discussed flow separation showing steep velocity gradients that are a source of turbulence [86]. In the swirl region downstream of the mixing element ($50 - 600\,mm$), significant differences in the TKE are predicted for the investigated setups. All MARS differencing schemes results show a local TKE maximum at some distance downstream of the mixer ($300 - 350\,mm$). This observation can be explained by the turbulence generation, due to the strong velocity gradients in the swirl flow and during the secondary vortices development. The UD scheme tends to a smear the gradients [86], so the upwind scheme results are quite flat in the region and lack the TKE peak downwind of the mixer. In all cases, the swirl structure, created by the mixer, successively breaks down. The big structure's kinetic energy is continuously transferred to small scale structures, i.e. into turbulence and finally dissipates. This can be seen from the turbulent dissipation, which is shown
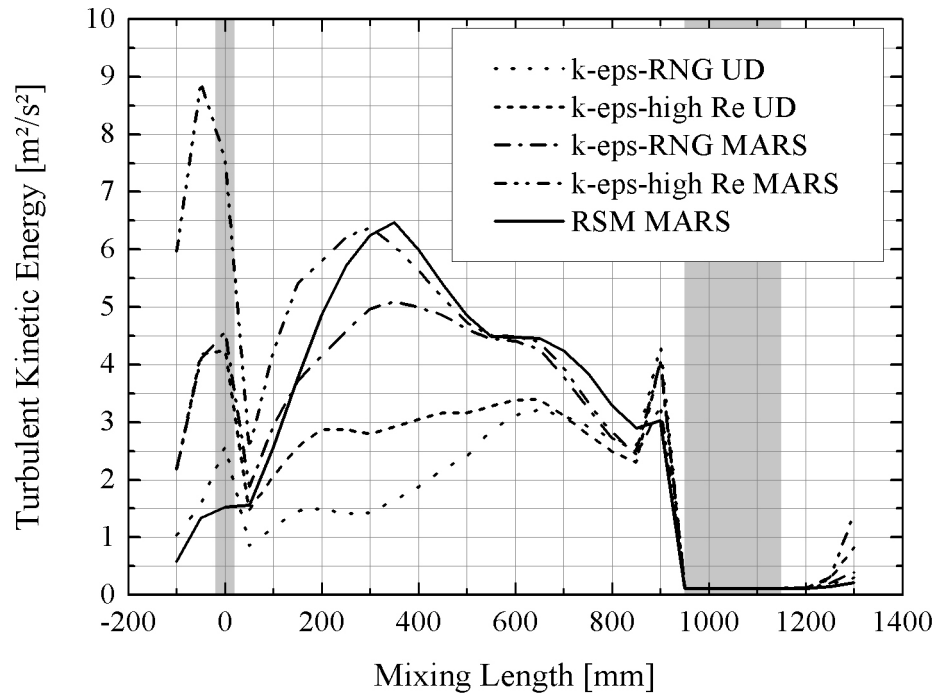
Figure 7.9:   *Mean turbulent kinetic energy on sections along the exhaust system under variation of the model setup*

in Figure 7.10. In comparison to the TKE curves, the figure shows that for each case, regions of high mean turbulence are regions of high mean turbulent dissipation. However, there are significant differences in the strength of this correlation between the particular model setups. Though the k-ε-high Re model and the RSM with MARS differencing scheme showed very similar levels of turbulence in the region of strong swirl ($50-600\,mm$), they differ with respect to the dissipation in this area.

To understand this observation, Figure 7.11 shows the local distribution of the TKE and dissipation in the exhaust line's mid plane for the two model variants.

Focusing on the swirl region, the two-equation-model shows a separation between the high turbulence inner swirl core and an outer near wall domain with lower turbulence and dissipation levels (this is common to all analyzed k-ε-variants). In contrast, the RSM shows an elevated turbulence level across a wider range of the pipe section and a completely different topology of turbulent dissipation. In the latter case, turbulent dissipation is concentrated in the region between the main and secondary swirls. The swirl core is not dissipating from its center, but from its outer rim, though the core has maximum TKE values. In that sense the RSM differs from all of the two-equation formulations that always show a local high TKE - high dissipation correlation. For the RSM, the main kinetic energy elimination takes place,
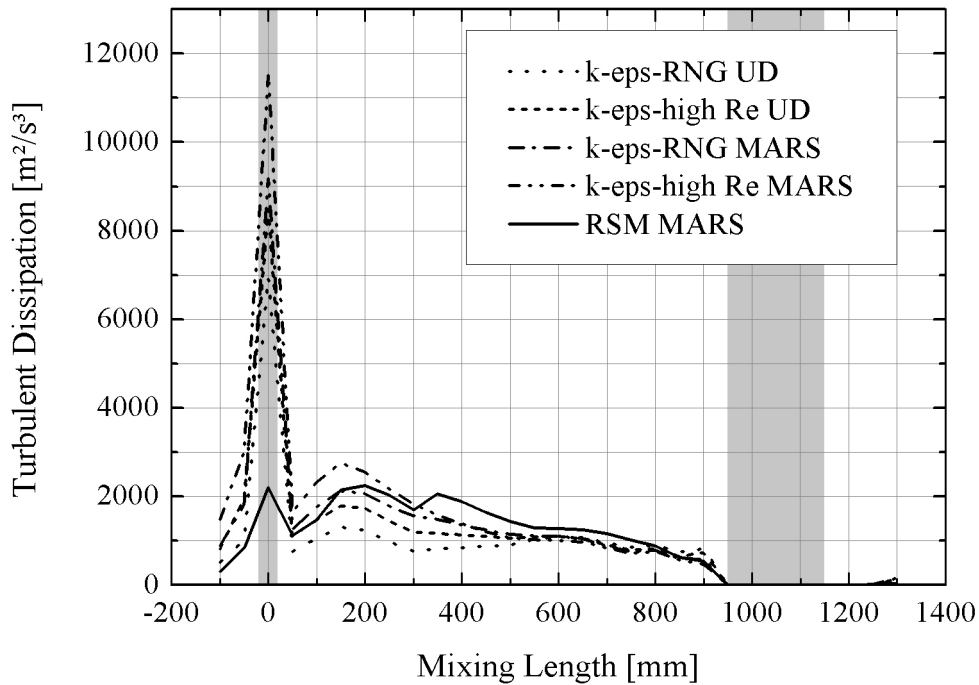
Figure 7.10: *Mean Turbulent Dissipation on sections along the exhaust system under varia-tion of the model setup*

where a maximum of shear forces in the direction perpendicular to the main flow region can be expected, i.e. where the primary vortex touches the secondary counter rotating vortices and angular momentum is transferred to the near wall pipe region. This effect cannot be captured with the same intensity by the two-equation models.
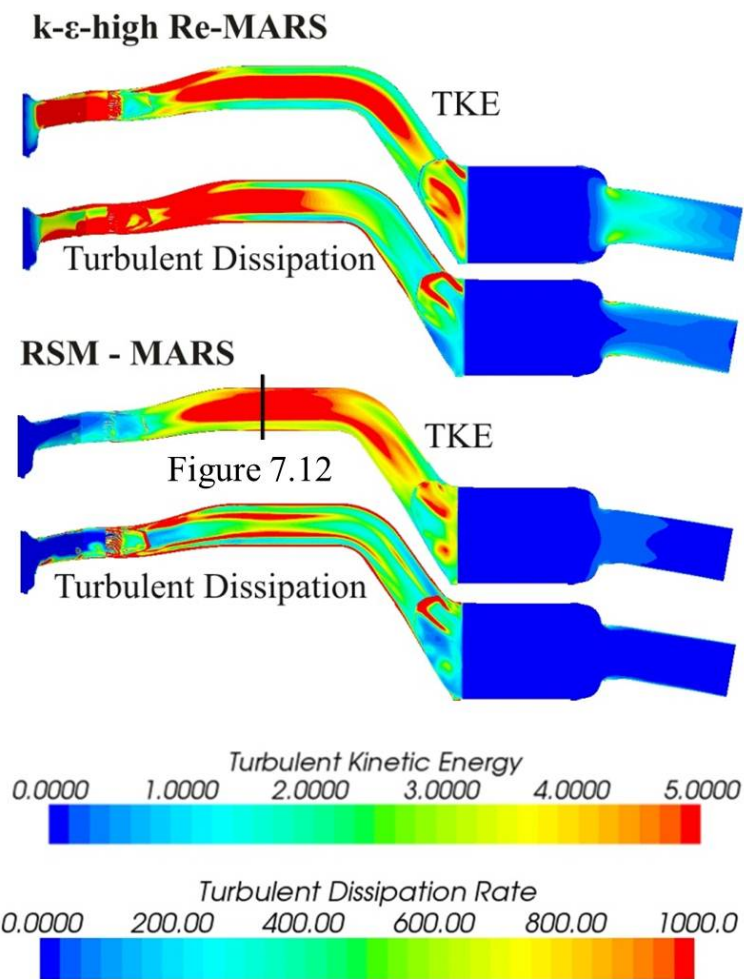
Figure 7.11: *Turbulent kinetic energy and dissipation on the mid-plane of the exhaust system under variation of the model setup*

To analyze the cause, Figure 7.12 shows the Reynolds stress tensor components on a pipe cross section in the swirl region (see marker Figure 7.11).
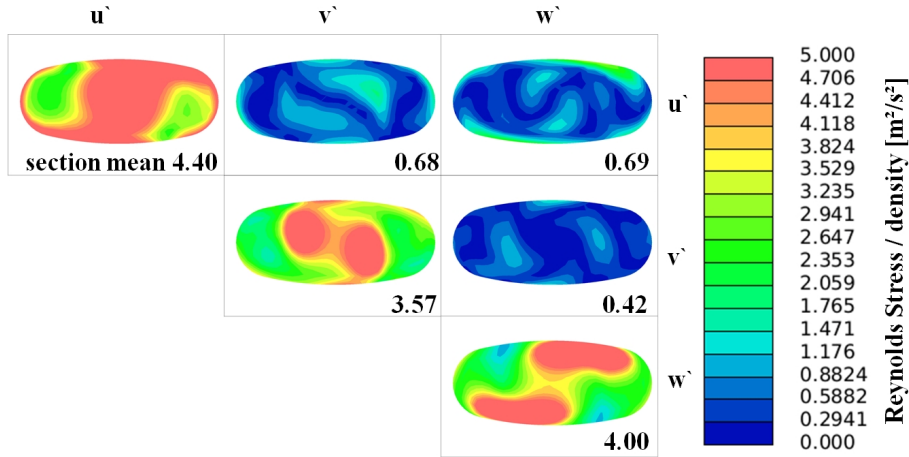

Figure 7.12:   *Reynolds stress tensor components on a pipe cross section in the swirl region (see marker Figure 7.11)*

The figure signals that the **isotropy assumption of the k-ε-models is insufficient within the swirl zone**: First, significant differences occur between the local normal stresses (diagonal elements of the RS tensor). Second, the off-diagonal shear stresses cannot be neglected as they reach up to $20\,\%$ of normal stress magnitudes. Therefore, none of the conditions that justify an isotropic turbulence assumption that underlies all k-ε-models is fulfilled within the swirl flow [108]. This has also been observed by El-Tahry [87] and predicted by Ström et al. [40].

To conclude, only the RSM with its anisotropic turbulence description is capable to predict the strong coupling between the primary swirl core and the outer secondary vortices. This leads to elevated TKE values across a wide range of the pipe cross section and a relatively low dissipation in the swirl core.

7.4.2.2 Turbulent Viscosity

In any of the discussed model setups, the turbulent viscosity determines the turbulent diffusion, see Equation 2.16. It is therefore expected to be the most relevant quantity for ammonia mixing on small length scales. Figure 7.13 shows the mean turbulent viscosity on cross sections along the exhaust pipe for all turbulence model/differencing scheme setups investigated in this work. Again, different predictions of the particular model setups exist. The most obvious difference is the accentuated peak of turbulent viscosity around $300\,mm$ downstream of the mixer that is solely predicted by the RSM. It is the manifestation of the maximum turbulent energy (Figure 7.9) in the swirl and a relatively low level of turbulent dissipation (Figure 7.10). This behavior in the swirl flow, is unique to the RSM, as discussed in the section above. **None of the two-equation formulations is capable to model the high turbulence level in the swirl flow,**

without predicting a relatively high dissipation at the same time.
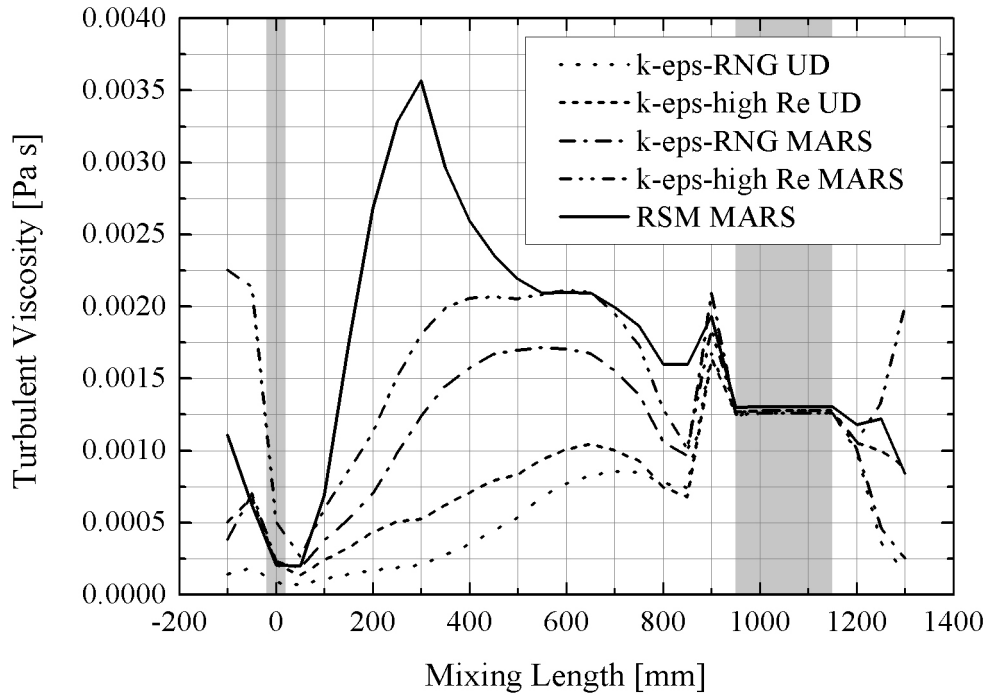

Figure 7.13: *Mean turbulent viscosity on sections along the exhaust System under variation of the model setup*

With respect to the arrangement of the viscosity curves, predicted by the different setups, one observes the same sequence as for the TKE. The UD schemes therefore tend to predict lower viscosity levels than the MARS scheme, for the same two-equation turbulence model. The observed differences are higher than $100\,\%$ in the swirl region. In contrast, all models show a similar steep gradient for the mean turbulent viscosity in the catalyst inlet cone (around $900\,mm$). This is due to the reduction of the swirl core strength in the widening cone (see also Figure 7.8), which results in a more isotropic character the turbulence. Further, all models predict a flow separation in this area (Figure 7.6), which leads to similar turbulent viscosity values. The quantitative differences in the height of the local viscosity maximum at $900\,mm$ correspond to the different recirculation volume predictions. As pointed out earlier, the RSM showed the most extended recirculation, which results in the highest turbulent viscosity value.

The impact of the turbulence model and differencing scheme on the calculated turbulent viscosity distribution in the mid section is shown in Figure 7.14.

The grading from low to high overall viscosity predictions with increasing model complexity is obvious. In more detail, **the unique capability of RSM to account for turbulence**
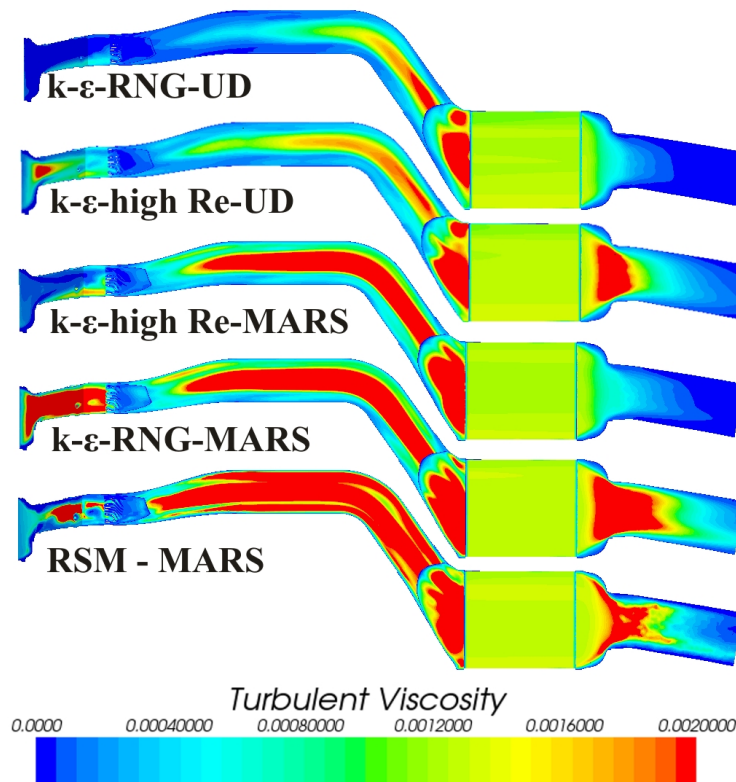
Figure 7.14:   *Turbulent viscosity on the mid-plane of the exhaust system under variation of the model setup*

anisotropy is apparent in the swirl region, downwind of the mixing element. The separation between the highly turbulent viscous inner swirl core and low viscosity outer secondary flow region - noticeable in all two-equation variants - is not as pronounced for the RSM. Only in the latter case, an increased turbulent viscosity can be observed across a wide range of the pipe cross section within the swirl region.

7.4.2.3 Conclusion

A conclusive survey of the previous results is given in Figure 7.15. The diagram shows the average inner swirl number and turbulent viscosity in the mixing section ($0 - 850\,mm$, excluding the catalyst inlet cone) as a function of the submodel setup.

The increasing perpendicular coupling of flow regions with increasing submodel complexity produces two major trends: A decreasing inner swirl number, which is accompanied by an increasing turbulent viscosity within the swirl region. While the former can be expected to affect the convective ammonia scalar mixing, the latter determines the turbulent diffusion. In order to evaluate those impacts on the ammonia homogenization, it is studied under variation of turbulence modelling depth in the next step.
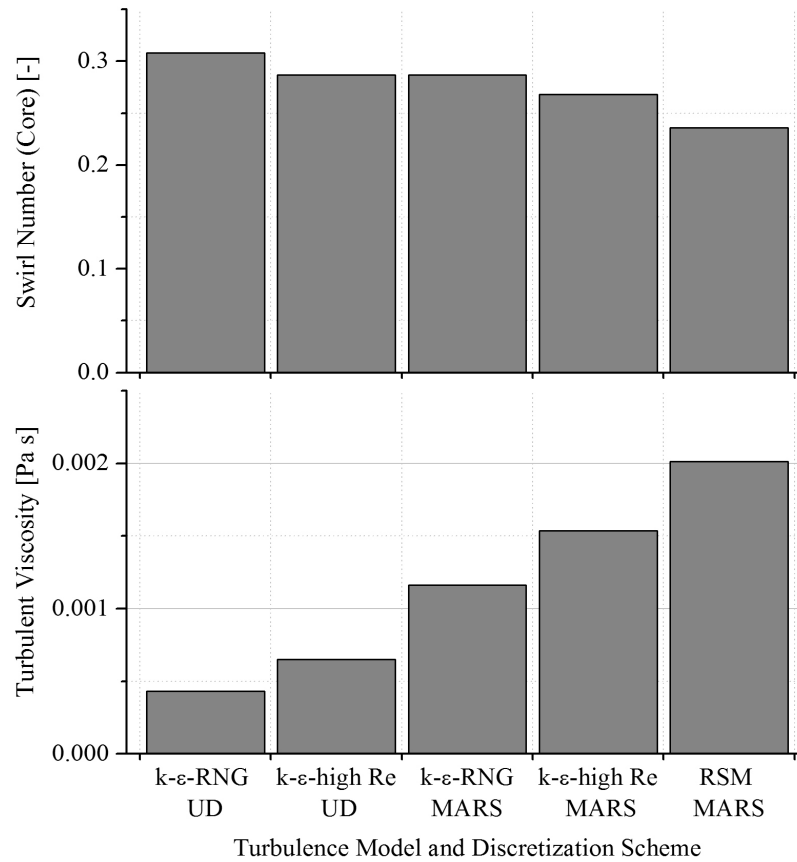
Figure 7.15: *Total average of inner swirl and turbulent viscosity in the mixing pipe* $(0 - 850\,mm)$ *under variation of the model setup*

7.4.3 Ammonia Homogenization

On the basis of the steady state flow fields discussed in the previous section, transient calculations with UWS injection for OP 1 are carried out. For each case, the settings of the turbulent flow field and spatial discretisation are maintained. The transport equations for the scalars are discretised with the same differencing scheme as the momentum and turbulent flow properties for each case. The Setup 2 from Table 7.1 has no longer been considered in the transient run, as results are expected to be quite similar as for setup 1. Though two-way-coupling between the liquid and gas phase is accounted for, no significant impact from the spray to the flow field can be noticed. The reason for this is the relatively low momentum of UWS spray. Therefore, the flow field does not change during the transient run and all effects discussed in the previous section remain valid, even with UWS injection.

7.4.3.1 Droplet Impingement and Ammonia Sources

Based on the findings from the previous modelling stage, OP1 has been chosen for the sensitivity study of ammonia mixing. In this case the gas temperature and therefore the mixer and pipe wall surface temperatures are well below the deposition/thermal break-up limit temperature for UWS. As a consequence, most of the liquid mass evaporates from a thin intermediate liquid film formed on the mixer or in the surrounding wall region. This behavior is captured by the Bai-impingement model due to the adoption to the experimentally observed UWS behavior. The resulting spray dynamics during impingement can be seen in Figure 7.16.
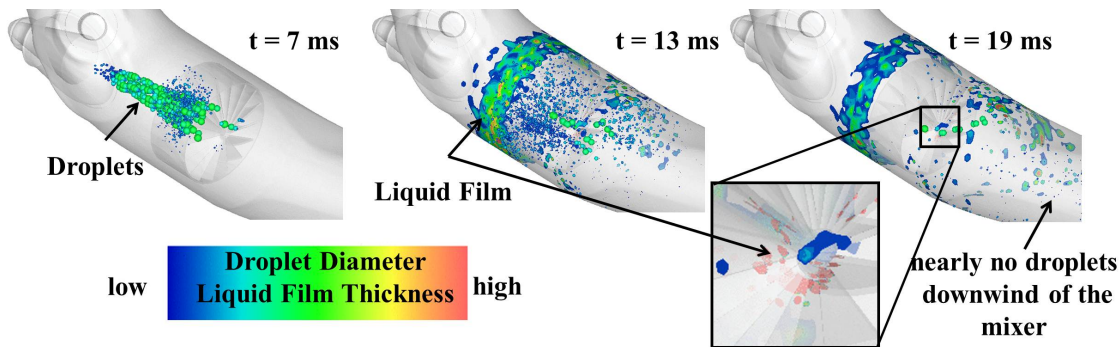

Figure 7.16:   *UWS spray impingement process on the swirl mixer for OP 1*

The figure shows UWS droplets and liquid film during injection. The film thickness and droplet diameter is color coded, while the parcel mass is represented by the parcel diameter. Most of the liquid forms a film on the mixer and pipe walls upstream of the mixer and nearly no droplet mass remains downstream. As a consequence, ammonia mixing can be analyzed along the complete mixing section with a well defined ammonia source location. Moreover, interdependencies from the liquid phase that may, under other circumstances, additionally travel down the mixing pipe are avoided by this means. For OP 1, no liquid film remains on the mixer or walls and the solid temperatures of the mixer and pipe are recovered by the time the next injection burst hits them. This allows one to conclude that a single injection event can be regarded as representative in this particular operating point.

7.4.3.2 Convective and Diffusive Mixing Process

With this well defined boundary condition of the ammonia source (liquid urea) location, the convective and diffusive mixing with different turbulence models and differencing schemes of the scalar can be studied. The transient ammonia vapor homogenization process is evaluated according to Section 7.3. Figure 7.17 shows the resulting quasi-steady ammonia vapor distribution on sections along the exhaust system gained for the simulation setups from Table 7.1 (except for setup 2).

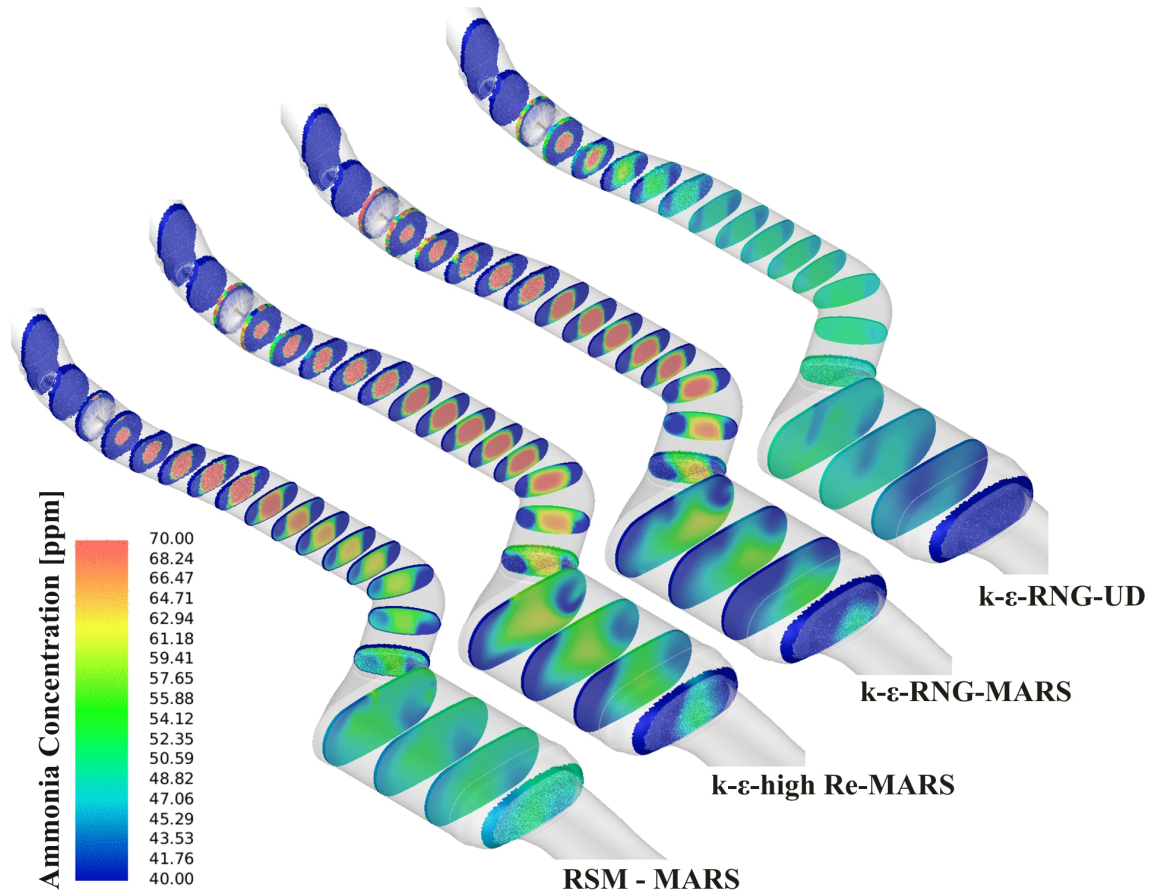The uniformity index of the ammonia distribution for each section has been plotted along the system in Figure 7.18.

Figure 7.17:   *Quasi- steady ammonia vapor distribution on sections along the exhaust system under variation of the model setup*

A high ammonia concentration can be observed in the pipe center due to the film evaporation on the mixer, see Figure 7.17. Therefore, all models have an identical UI of 0.23 at the mixer position, see Figure 7.18. However, significant differences occur in the ammonia distribution further downstream of the pipe for the different setups. The k-ε-RNG UD setup yields the steepest UI gradient along the pipe, corresponding to an extremely fast homogenization. The MARS scheme models follow, with the RSM predicting the second efficient homogenization and the remaining k-ε (MARS)- derivatives showing the lowest increase in ammonia homogeneity. As Figure 7.15 proves, the RSM predicts the highest turbulent diffusion coefficient (viscosity), followed by the two-equation MARS setups and the UD case with least efficient small scale mixing. An estimate of the convective transport has to take both the inner swirl and the secondary outer vortices into account. While the inner swirl strength decreases with model complexity, the outer vortices secondary flow again increases, see Figure 7.8. Therefore, it can be concluded that the overall mixing is dominated by the diffusive mechanisms.
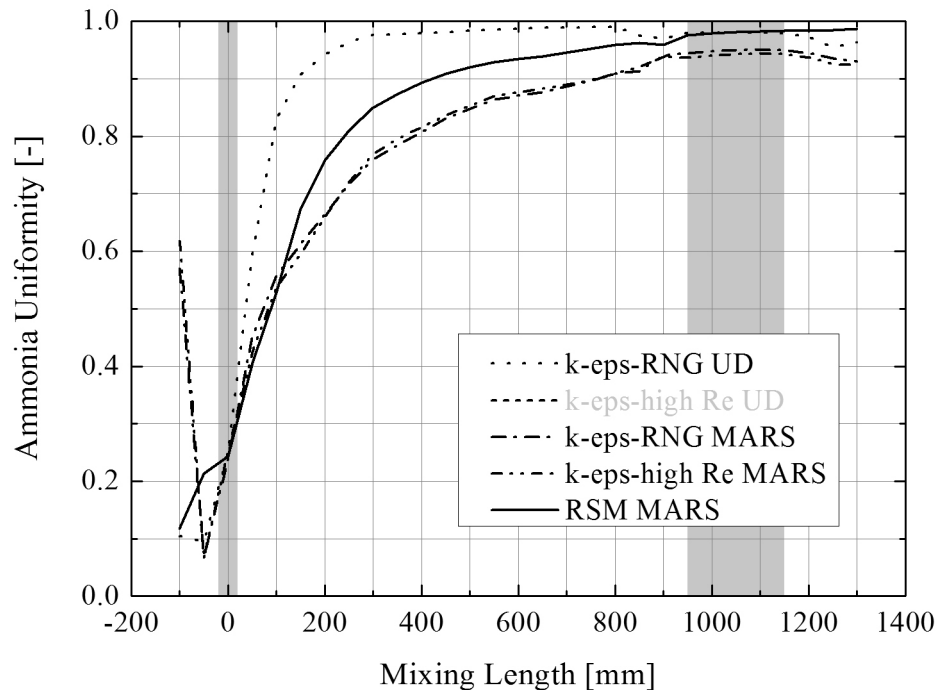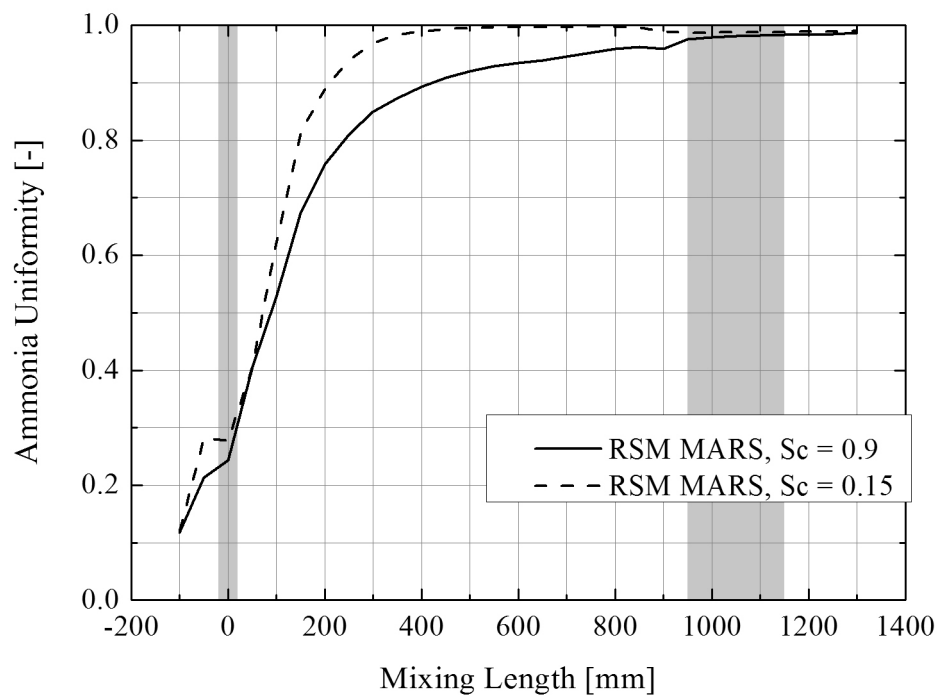
Figure 7.18: *Quasi-steady ammonia uniformity along the exhaust system under variation of the model setup*

The steep gradient of the UI for the UD setup in Figure 7.18 can therefore not be explained by the physical model used. It must be concluded that the **numerical diffusion of the first order scheme significantly influences the solution.** With a state-of-the-art mesh size for SCR-CFD-analysis it is therefore recommended to employ a higher order differencing scheme (e.g. MARS) to avoid a numerical overestimation of ammonia homogenization. For the remaining cases that have been calculated with the second order MARS scheme, the ammonia homogenization results are consistent with turbulence models predictions. The RSM predicts a better overall ammonia homogenization in the swirl flow than the k-ε-models. Maximum deviations in the UI of approximately $10\,\%$ are reached in the region around $300\,mm$, where the RSM predicts a peak in the turbulent viscosity. Overall, a better ammonia uniformity prediction of the RSM exists at the catalyst intake. The underlying spatial ammonia distributions in Figure 7.17 prove the RSM's better coupling of the swirl core region with the secondary vortices. An **enhanced ammonia transport in the direction perpendicular to the main flow on a physical basis (no numerical diffusion) can only be observed for the RSM MARS setup.**

7.4.3.3 Schmidt-Number Relevance and Adaption

According to Equation 2.16 the Turbulent Schmidt Number Sc_t directly affects the turbulent ammonia diffusion process. It is commonly accepted that Sc_t is in the order of unity ($0.7-0.9$) for typical gas phase mixing processes, but depending on the particular flow conditions and with significant local and temporal fluctuations (up to $50\,\%$) [109]. Recommended values from CFD studies even range from 0.2 [110] to 1.3, see discussion in Section 2.3 and Tominaga and Stathopoulos [88], who argue this is for compensation of insufficient turbulence description. A large eddy description of the scalar field has revealed temporal/local values of the turbulent Schmidt number between 0.2 and 2, with an average of 0.7. Despite these findings, no general rules are available to predict an adequate value for Sc.

In order to therefore study the sensitivity of the homogenization prediction to the empirical number (default value 0.9) in the SCR system, the ammonia mixing process has additionally been simulated with the RSM (MARS) setup for $Sc_t = 0.15$. A comparison of ammonia homogenization prediction with $Sc_t = 0.9$ and 0.15 is shown in Figure 7.19.

Figure 7.19: *Quasi-steady ammonia uniformity along the exhaust system under variation of the turbulent Schmidt number, RSM with MARS*

A comparison of the graphs reveals the systematic increase of the uniformity index gradient along the pipe with decreasing Schmidt number. The effect is most pronounced at low levels

of uniformity but high turbulent viscosities, i.e. in the near mixer region $(100 - 400 \, mm)$. As the UI approaches unity, the further homogenization and therefore the relevance of turbulent diffusion becomes insignificant. However, in total a small difference between the two setups even remains at the catalyst intake.

7.4.3.4 Ammonia Uniformity Validation

Figure 7.20 shows the ammonia distribution and corresponding uniformity indices at the catalyst inlet from the simulations and the CLD measurements. Each distribution on the right subfigure is normalized with its mean ammonia concentration value and local concentrations are plotted relative to it.
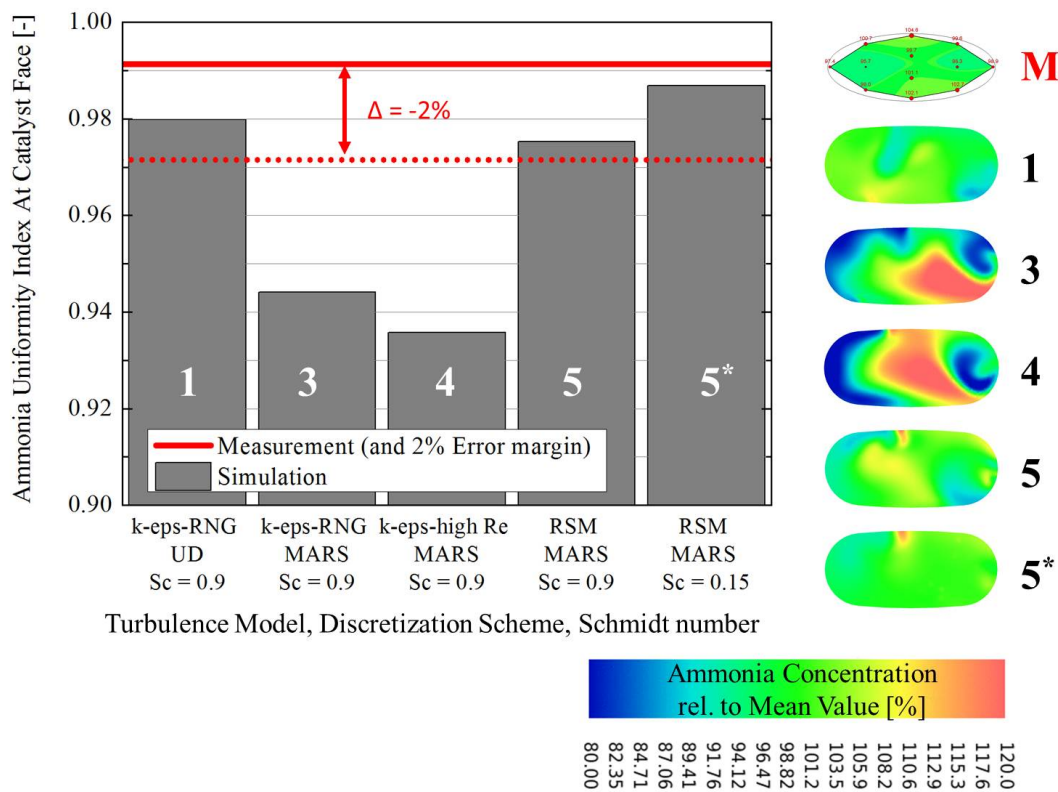

Figure 7.20: *Quasi-steady ammonia distribution and uniformity index at the catalyst intake plane under variation of the model setup*

As can be seen from measurements, the ammonia vapor is nearly perfectly distributed over the catalyst in OP 1. In the chosen scale $(80 - 120 \, \%$ of the mean value), no significant concentration gradient can be seen from the data. The measured uniformity index is therefore very near to unity (UI = 0.992). Only the k-ε-RNG with UD and the RSM with MARS differencing

scheme are capable to simulate such a homogeneous distribution within a two percent deviation limit. The prediction from the k-ε-RNG UD setup, though being closest to the measured value, results from numerical diffusion, i.e. a numerical error. For the remaining setups a more or less pronounced underestimation of the measured ammonia uniformity can still be noticed. The two-equation models show a $5\,\%$ deviation. This error magnitude is in good agreement with the underestimations that have so far been observed throughout validated literature cases that employed a k-ε-model [17, 90]. The RSM with MARS scheme is capable to reproduce the measured uniformity index within a $2\,\%$ limit of deviation for $Sc_t = 0.9$ and a $0.5\,\%$ limit for $SC_t = 0.15$, avoiding numerical diffusion. Considering the complexity of the complete process from UWS spray to the ammonia distribution at the catalyst, this can be regarded as a good prediction.

The remaining underestimation is very likely caused by the insufficiencies of any RANS formulation, even the relatively sophisticated RSM. A possible overcome could be the employment of LES for the flow [111] or even additionally for the scalar field [112]. However, this cannot be regarded as practical for an efficient, industry oriented SCR system design process with the CFD method at the current state. Another further improvement in predictivity might result from an anisotropic description of the turbulent scalar diffusion, see [112]. However, a commercially available formulation is not available at the present state.

As a compromise, the RSM with the Schmidt number adoption to 0.15 is regarded as a pragmatic best practice approach within the RANS limits, bearing in mind the compensative character of Sc-tuning [88]. As a benefit, the overall increase in computational effort, i.e. the calculation time for steady state and transient run, for the RSM with MARS is only about $20\,\%$ higher than for the two-equation k-ε-models.

7.5 Flow Field from Reynolds-Stress-Model Turbulence Description

The best practice turbulence model setup from the previous study (RSM with MARS) is employed to calculate the flow field in the SCR system for all OPs. The resulting turbulent flow properties as a function of the increasing volume flow will be discussed.

7.5.1 Swirl Flow Characterization

Figure 7.21 shows the average velocity magnitude evolutions for all OPs on cross sections along the exhaust pipe.

The array of curves reveals that the qualitative velocity development is independent of the particular volume flow (OP) in first approximation. All features discussed for the average velocity of OP1 from Figure 7.4 remain valid for the other OPs. The characteristics only differ in their quantitative degree, as the average inlet velocity increases linearly with the volume
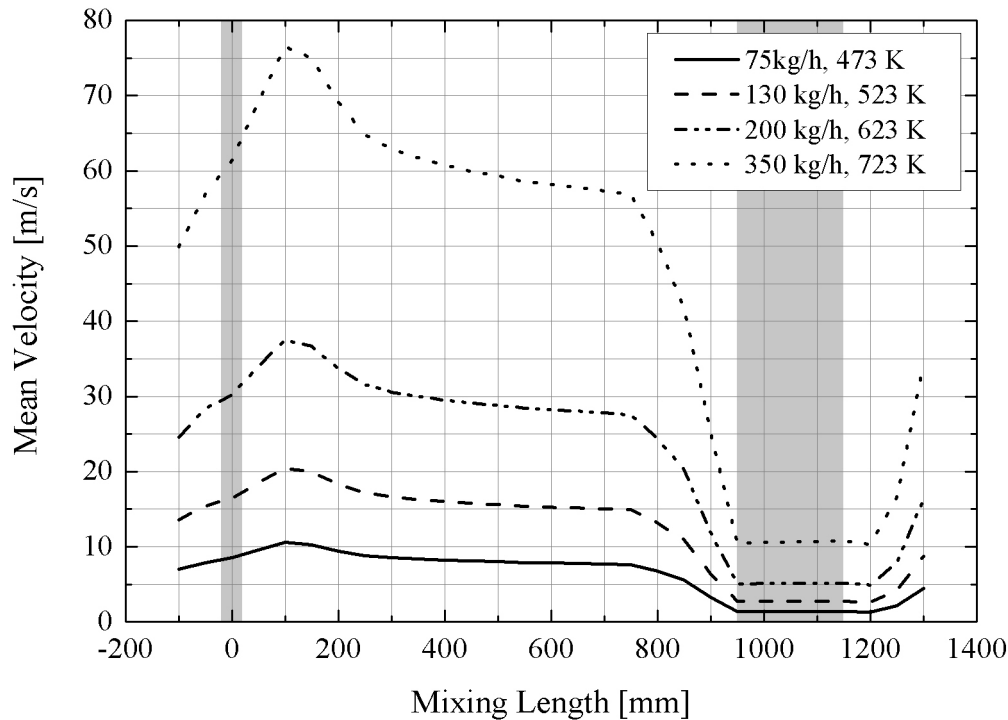
Figure 7.21: *Mean velocity magnitude on sections along the exhaust system for all OPs, RSM with MARS*

flow.

In case of the swirl number, depicted in Figure 7.22 for all OPs, the different curves even collapse to a nearly identical development. In first approximation, a constant (volume flow independent) ratio exists between the average angular momentum and the corresponding axial momentum, see definition of the swirl number in Equation 7.4. This is valid for both, the inner swirl core number and the total cross section value. The observation allows one to conclude that the pitch of the swirl, created by the static mixer, is independent of the particular volume flow (OP) in a first approximation. Thus, the convective transport velocity of ammonia, perpendicular to the main flow, is generally proportional to the one parallel to the main flow direction. In other words, an ammonia streak released from a local source near the mixer experiences the same number of revolutions in the mixing section regardless of the particular OP.

The swirl does increase very moderately with increasing volume flow in the downwind part of the mixing section, see also Figure 7.26, upper graph. The relative increase of the swirl number from OP 0 to OP 3 is however well below $10\,\%$, compared to an increase of volume flow by $700\,\%$. The large scale redistribution of ammonia should therefore be very similar for
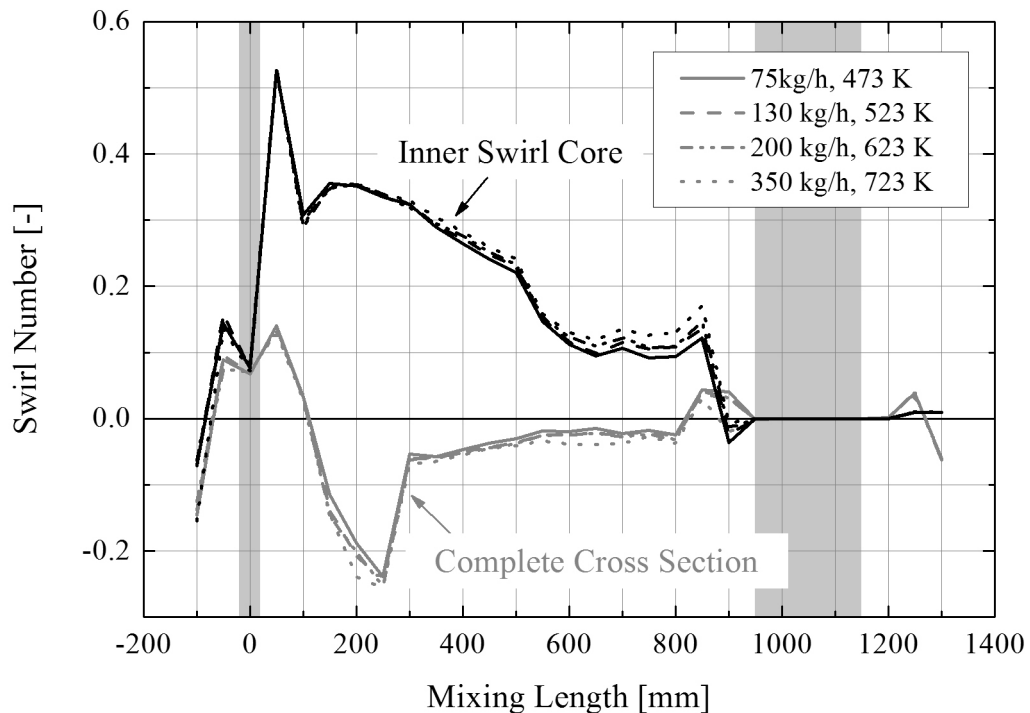
Figure 7.22: *Swirl number on sections along the exhaust system for all OPs, RSM with MARS*

all operating points, if only gaseous transport effects are considered, i.e. liquid phase dynamics are neglected.

Major impacts of the OP (volume flow) on the gaseous ammonia transport and homogenization have therefore to be expected from the turbulent eddies, driving the small scale turbulent diffusion.

7.5.2 Turbulent Properties of Flow Field

The average turbulent kinetic energy along the mixing pipe for all OPs is depicted in Figure 7.23. Again, the same behaviour can be observed for the evolution of all OPs. The local maximum, observed downstream of the swirl mixer for OP1, holds under all operating conditions. However, in contrast to the average flow field, on a quantitative level, a nonlinear increase in turbulent kinetic energy occurs, see logarithmic scaling of the ordinate. In accordance with turbulence theory, a quadratic increase of kinetic energy of the average flow field leads to a very similar increasing turbulent kinetic energy in first approximation [113].
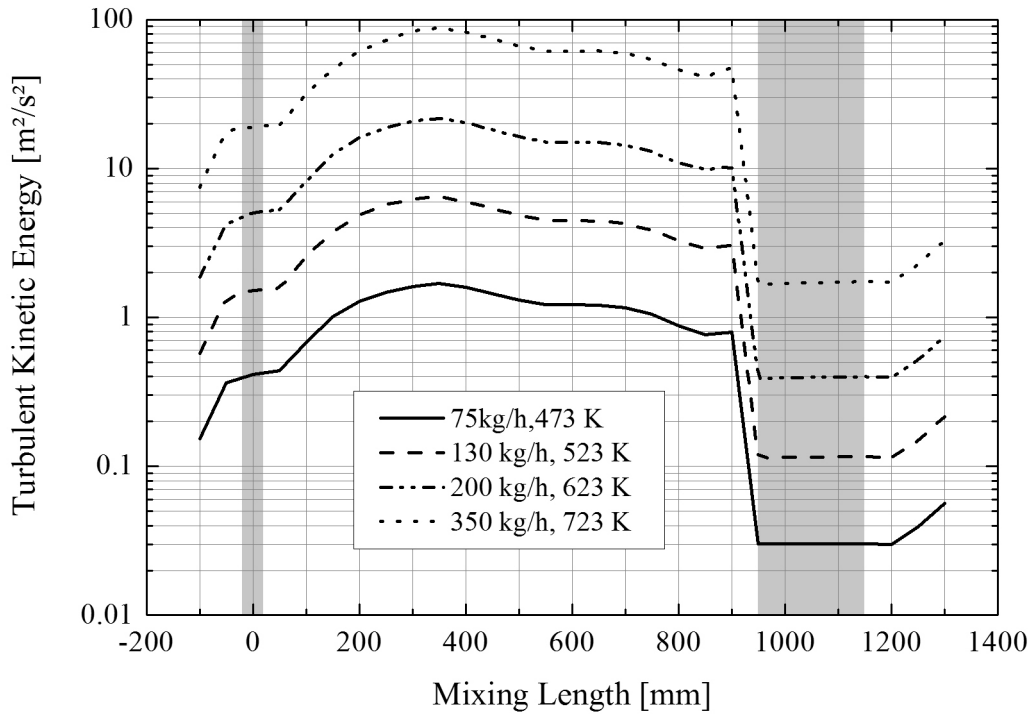
Figure 7.23: *Mean turbulent kinetic energy on sections along the exhaust system for all OPs, RSM with MARS*

Following the turbulence cascade to even lower length scales, the turbulent dissipation behaves very similarly. As Figure 7.24 reveals, the dissipation of all OPs shows the same qualitative behavior along the exhaust pipe. Maximum dissipation occurs as the flow passes the mixer ($0\,mm$) and in the very near downstream swirl ($150 - 200\,mm$), when the pipe's cross section changes from circular to oval. It is worth emphasizing that the latter position is well upstream of the maximum turbulent kinetic energy location ($350\,mm$, Figure 7.23), which is a unique feature to the RSM. This has already been discussed in context of Figure 7.11, lower subfigure. Quantitatively, a nonlinear increase of dissipation levels by three orders of magnitude from OP0 to OP3 is obvious.

The resulting sectionwise turbulent viscosity is shown in Figure 7.25 for all OPs. As a consequence of qualitative similarity between all OPs of both the TKE and dissipation, the viscosity shows an analogous behavior. All qualitative characteristics of the viscosity evolution, including maxima and minima locations, remain similar with increasing volume flow. The absolute values again increase with the volume flow (OP) and differ by up to a factor of five between OP0 and OP3. This can be attributed to an increasing turbulent eddy formation due to higher velocities and resulting fluctuations in the exhaust system. However, the dis-
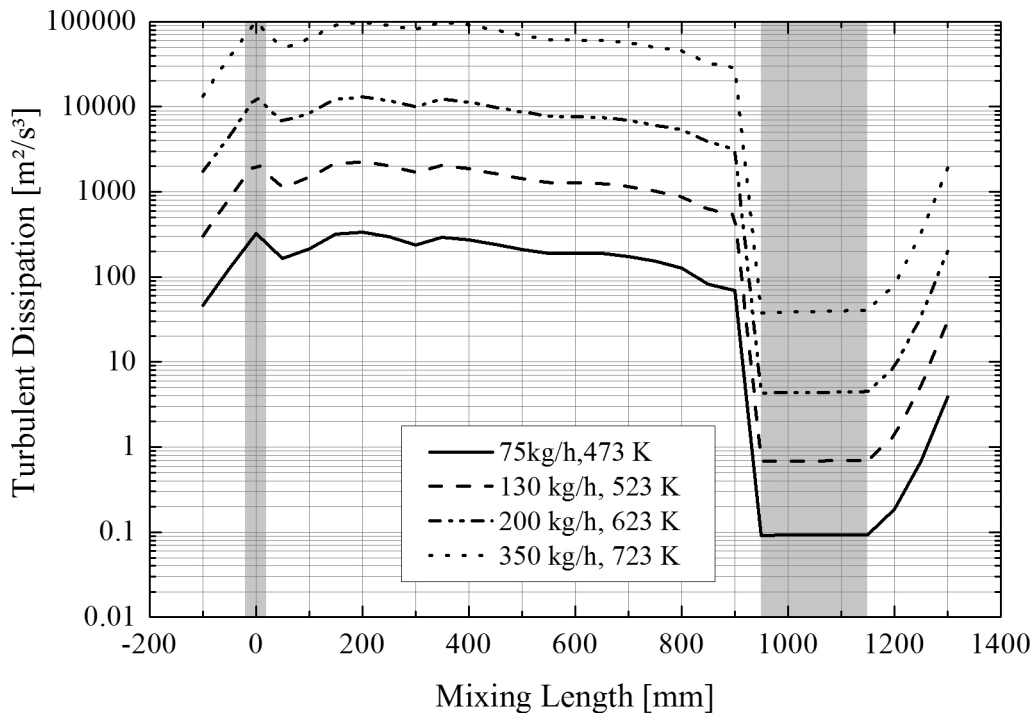
Figure 7.24: *Mean turbulent dissipation on sections along the exhaust system for all OPs, RSM with MARS*

tinct nonlinear trend of the overall turbulent kinetic energy and dissipation with volume flow becomes less pronounced for the turbulent viscosity.

7.5.3 Conclusion and Validation

A full summary of the flow properties as a function of the operating point (volume flow) is given in Figure 7.26. The graphs show the average values within the mixing section ($0 - 800\,mm$, i.e. excluding the catalyst inlet cone) of all relevant flow properties as a function of the exhaust gas volume flow.

As already indicated, the swirl number is only moderately changing with increasing exhaust gas flow. In very good approximation, a quadratic increase can be observed for both the TKE and -dissipation, see fitted parabola-models (red dashed lines). The turbulent viscosity increases less then quadratically, and even slightly sub-linear, with volume flow. This is due to the change of gas density, in addition to turbulence increase ($\mu_t \sim \rho \cdot k^2/\varepsilon$).

With respect to the mixing of ammonia, the following expectation may be deduced from those trend curves (assuming the same ammonia source location): as the swirl is only moderately changing with the OP, no significant effect is expected for the convective transport of
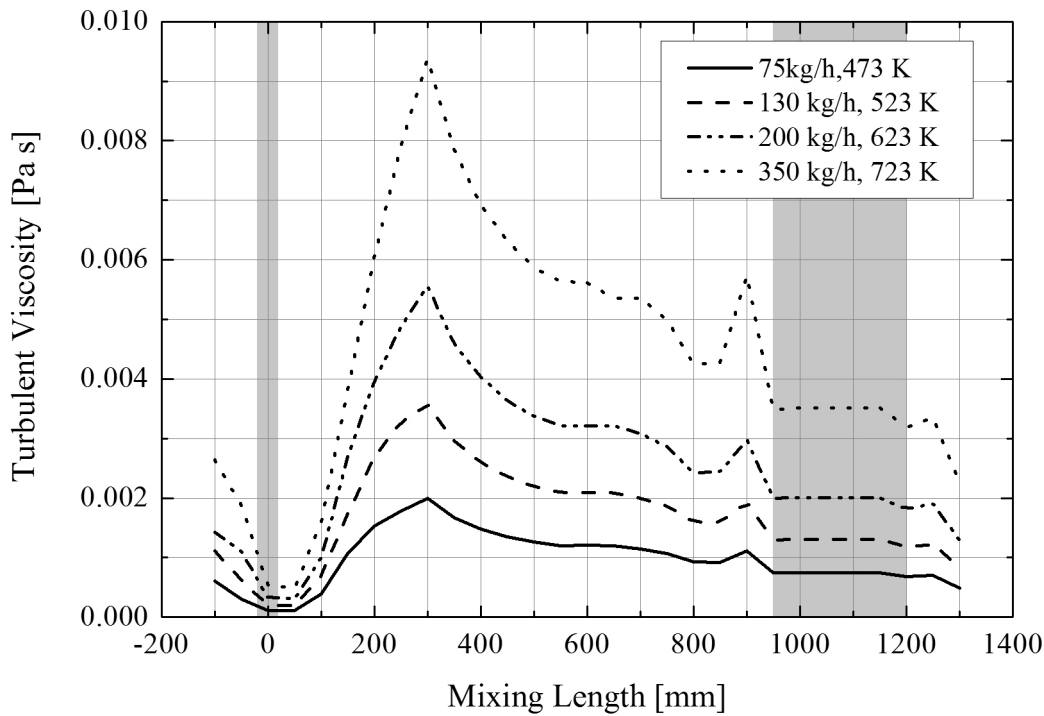
Figure 7.25: *Mean turbulent viscosity on sections along the exhaust system for all OPs, RSM with MARS*

ammonia vapor. This is at least valid within the swirling flow region, but may not be true in the recirculation region of the catalyst inlet cone, see Figure 7.6. In addition to the convective mixing of ammonia, driven by the large swirl structure, the turbulent viscosity drives the turbulent diffusive ammonia homogenization on small length scales. The nearly linear increase of turbulent viscosity can therefore be expected to enhance the turbulent diffusion of ammonia vapor with raising exhaust volume flow, see Equation 2.16.

The lowest subfigure from Figure 7.26 shows the back pressure of the SCR mixing system as a function of the exhaust gas volume flow (OP). In addition to simulation the figure includes test bench results for validation purposes [8]. At low volume flow conditions, back pressures values are at the same order of magnitude as the measurement precision, which should be taken into account for the validation discussion. In this particular range, the simulation slightly overestimates the back pressure with a maximum offset of approximately $1 \, mbar$. At high volume flows, when measurement data is more precise and reliable, the back pressure is very well predicted by the CFD simulation. This indirectly confirms the turbulence predictions from the RSM.
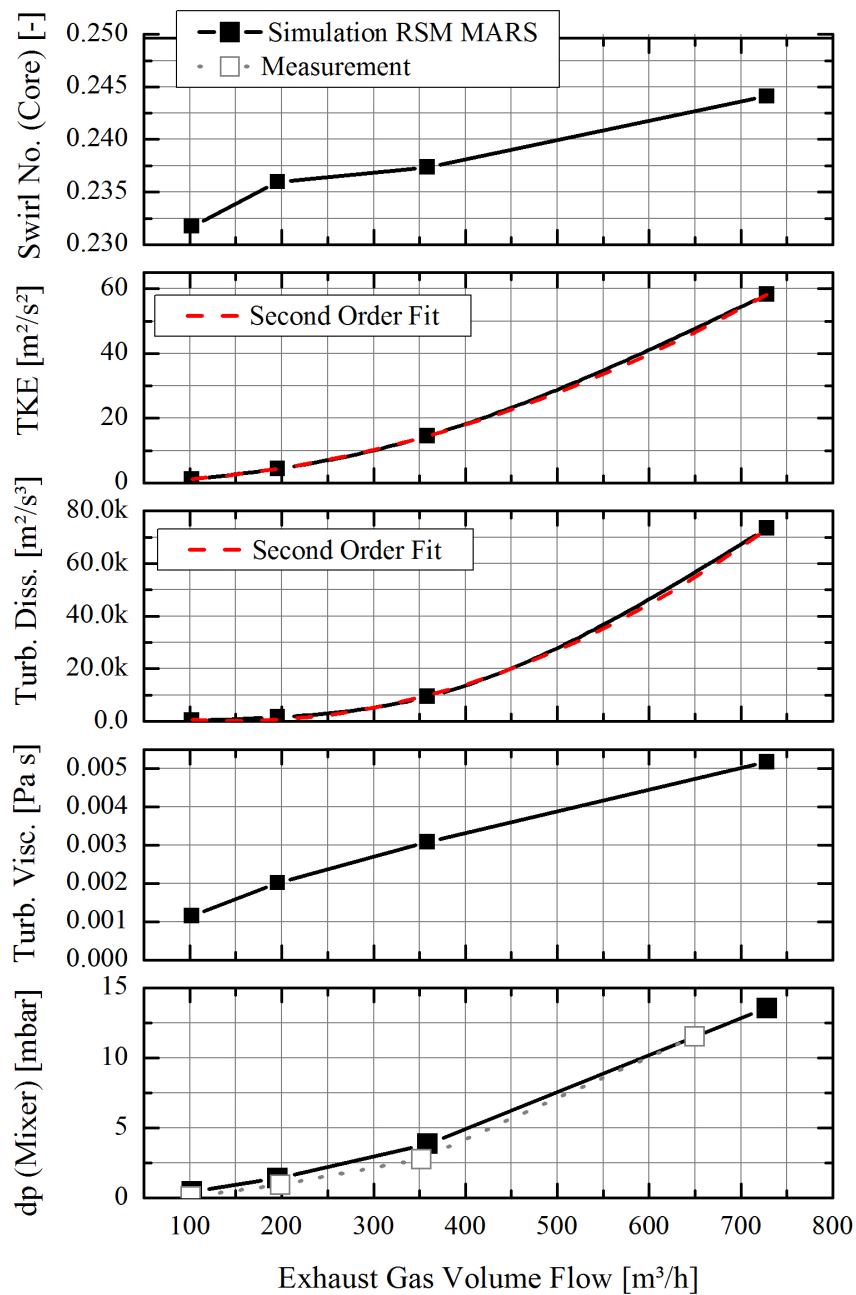
Figure 7.26: *Average values of flow properties in the mixing section $(0 - 850\,mm)$ as a function of the exhaust gas volume flow (OP), RSM with MARS*

7.6 Impact of Ammonia Source Term Prediction

The previous discussion of flow impacts on ammonia homogenization is only valid, if the formation of ammonia from UWS took place at the same location for all operating conditions. As can be expected from the basic research stage on droplet impingement, Section 6, this assumption is not generally applicable due to the wide temperature range of OPs. The impact of ammonia source location on the homogenization process, resulting from different droplet wall interaction behavior, will therefore be discussed in the following section.

7.6.1 Ammonia Uniformity Dependency on Operating Conditions

Figure 7.27 and Figure 7.28 show, respectively, the uniformity index and the underlying distribution of ammonia at the catalyst inlet for all analyzed operation points. Measured uniformity values and distributions from the test bed are compared to simulation data from the best practice CFD-model, including the validated UWS decomposition model, the Reynolds stress turbulence description with MARS and the adapted multi-regime Bai-model.
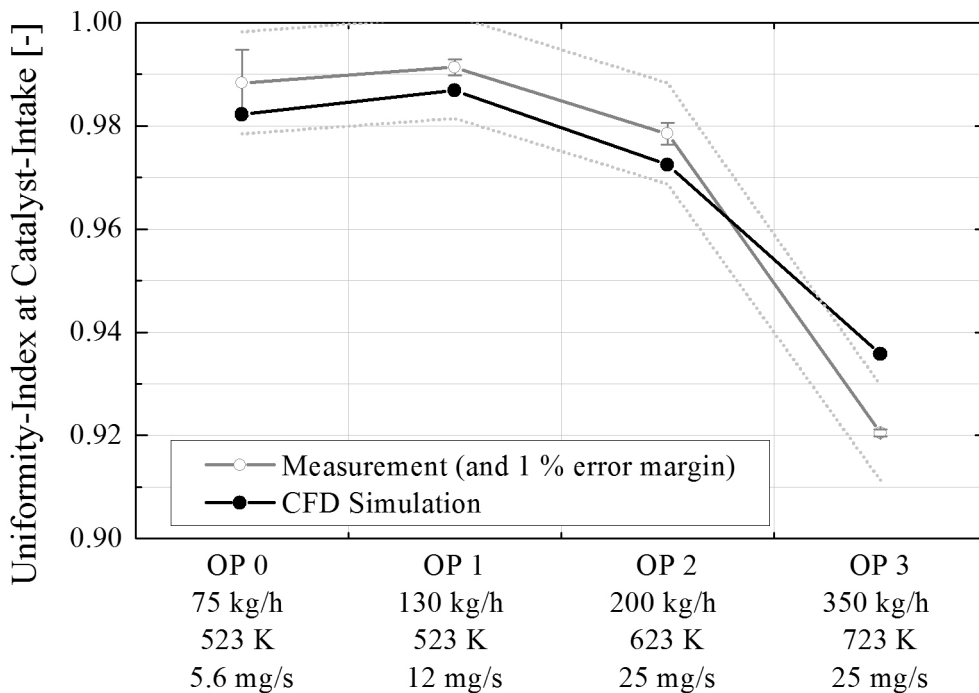

Figure 7.27: *Measured and predicted ammonia uniformity-index at the catalyst inlet plane as a function of the OP*
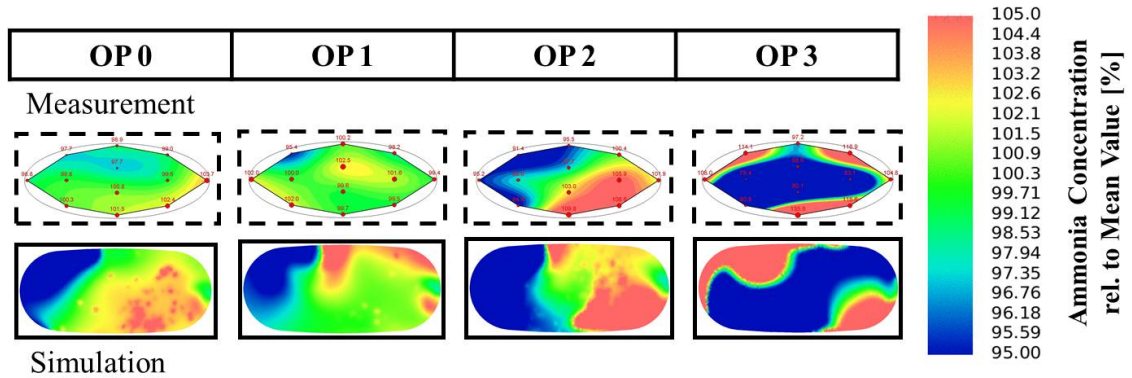
Figure 7.28:   *Measured and predicted ammonia distribution at the catalyst inlet plane as a function of the OP*

Both, simulation and measurements show a slight increase of ammonia uniformity from OP 0 to OP 1, but a remarkable drop towards the OPs with high temperatures and exhaust flows. The simulation matches the measured uniformity index values within a $1.5\,\%$ deviation limit for all OPs and the measured nonlinear trend is correctly predicted. In addition, the CFD model predicts the underlying ammonia distribution correctly. Especially for the inhomogeneous cases OP 2 and 3 the locations of ammonia hot spots are in good agreement with measurement. The observed trend of a lower ammonia uniformity for the higher OPs is however contradictory to the turbulent flow property evolution with increasing volume flow, see discussion of Figure 7.26. The key factor to understand this behavior, lies in the correlation between the liquid phase dynamics, i.e. the location of the ammonia sources, and the ammonia homogenization process.

7.6.2 UWS Droplet Dynamics and Impingement

The relevant droplet impingement regimes at the mixing element and exhaust system walls for the different OPs are very similar to the ones observed in the straight pipe analysis, Section 6. This can be seen from the simulated spray behavior during impingement in Figure 7.29. It shows the UWS droplets and liquid film for each OP during injection and interaction with the mixing element. The film thickness and droplet diameter are color coded, while the individual parcel mass is represented by the plotted parcels' diameters. In order to better compare the post-impingement droplet mass for the different OPs, the parcel diameters are scaled up after the primary injection by a factor of 10 (Apart from this, the fourth line in the picture series of Figure 7.29 is a duplicate of the third line).

For the low temperature cases OP 0 and OP 1 nearly no droplet mass remains downstream of the mixing element after spray impingement. In those cases most of the UWS forms a film on the mixer and pipe walls upstream of the mixer. This has already been observed in the straight pipe configuration. Some droplets that splash on the mixers' surface even travel
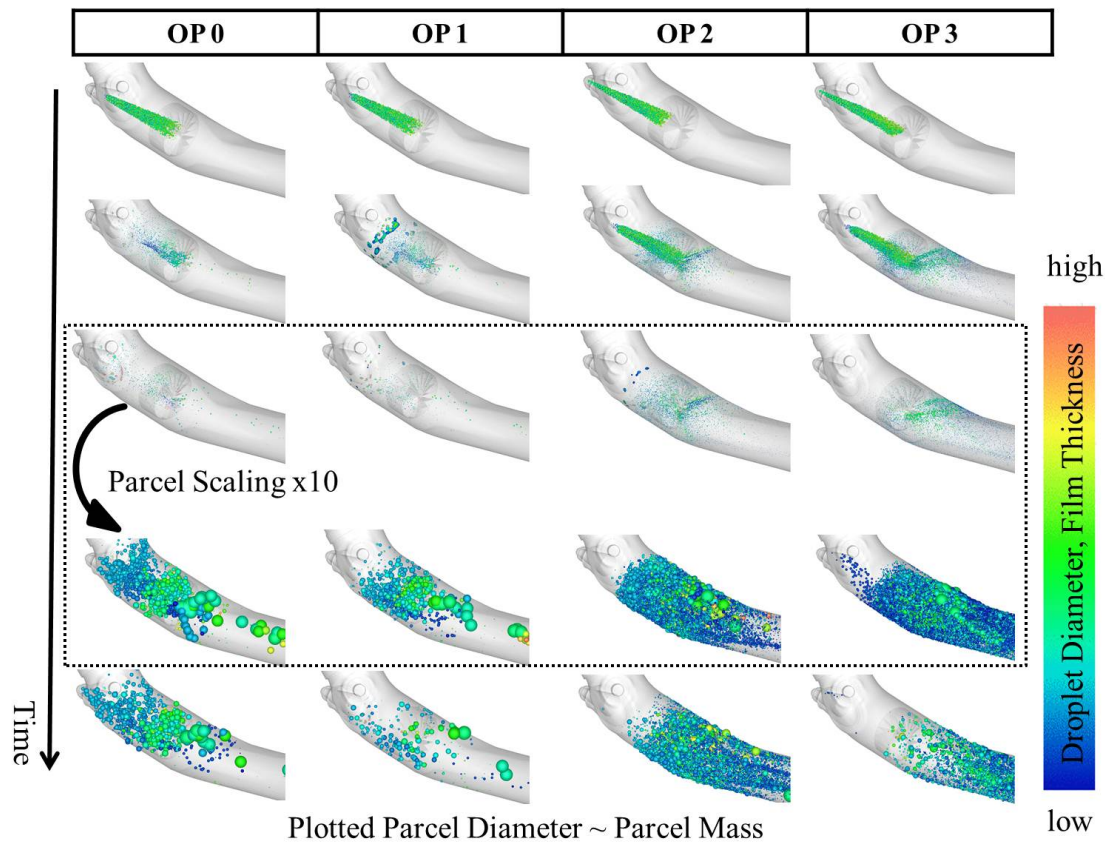
Figure 7.29:   *Droplet dynamics and liquid film formation during spray impingement on the mixing element, all OPs*

against the flow direction until they are reversed by drag forces. This is possible, due to the relatively low mass flows for those OPs. Downstream of the mixer, only a few large droplets from the primary spray remain, which have passed the mixer unchanged due to an incomplete overlapping of mixer blades (see green droplets with an intermediate diameter). Those droplets can also be found for the intermediate temperature OP 2 and high temperature OP 3. However, in those cases, a substantial number of secondary droplets can additionally be found downstream of the mixer. A significant decrease of the secondary droplets' diameters can now be observed, resulting from droplet break-up at the mixer vanes. Again, those observations are in accordance with the theoretical estimations and observations from the basic impingement studies from the previous modelling stage.

The amount of secondary droplets and their further evolution along the mixing section can be seen from Figure 7.30. Droplet scaling and -coloring are analogous to the lower part of Figure 7.29. The average droplet velocities vary from OP to OP, due to the different exhaust flow velocities. However, to compare the extent of secondary droplets, the depicted times

117

are chosen to get an impression of the maximum extent of secondary droplets in the mixing section for each OP.
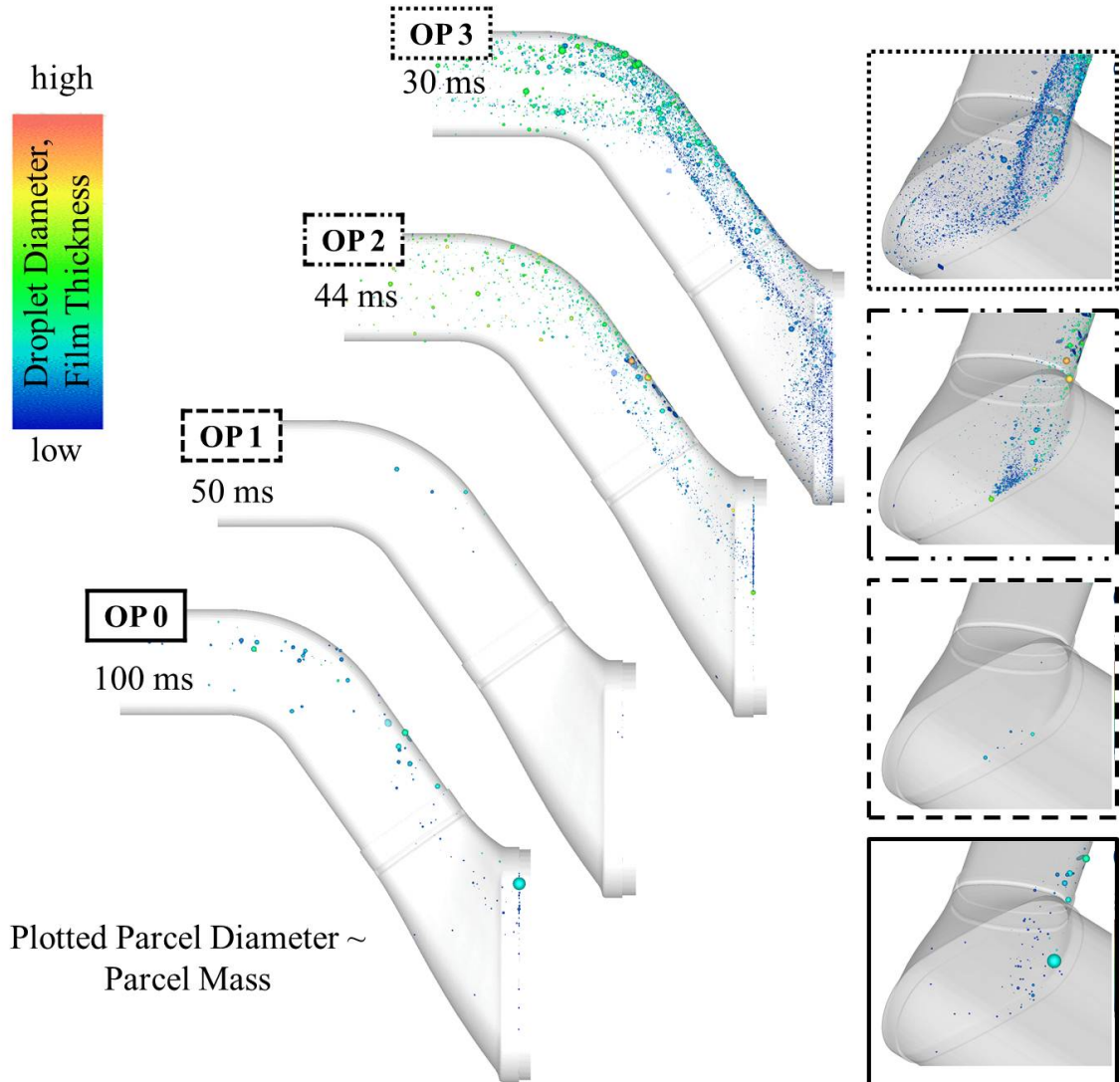
Figure 7.30: *Secondary droplets remaining downstream of the mixing element and reaching the SCR catalyst surface*

The figure reveals that with *increasing* gas temperature and exhaust flow (from OP 0 to OP 3), the mass of droplets that reach the downwind parts of the mixing section successively *increases*. This trend remains valid even down to the catalyst intake plane, see right subfigures of Figure 7.30. A substantial amount of UWS droplets hits the catalyst surface for OP 3, followed by OP 2 while for the low temperature OPs 0 and 1 the amount seems negligible.

This observation can be understood for the following reasons: the successively rising vol-

ume flow from OP 0 to OP 3 leads to increased mean exhaust velocities and - in consequence - droplet transport velocities. Thus, less time is available for droplet evaporation for the OPs with higher mass flows. This effect competes with the higher exhaust temperature (see Figure 5.3) and the higher relative velocities between droplets and gas, which both enhance the droplet evaporation rate. However, considering only the gas phase effects does not solely explain the increasing liquid phase amount reaching the catalyst with increasing OP.

The major factor determining the liquid phase amount at the catalyst is the fraction of droplets, which are passing through the mixer. Thus, the UWS evaporation on surfaces of the exhaust system must be additionally considered. While the decomposition of levitating or dispersed UWS droplets is improved by an increase in ambient gas temperature, this is no longer generally valid for droplets interacting with walls of increasing temperature. Here, the nonlinear nature of thermal droplet-wall contact as described by the Nukiyama curve (Figure 6.2) and the Leidenfrost phenomenon in the Bai-model becomes relevant. By considering the formation of an isolating vapour cushion between wall and droplet for high surface temperatures (see OP 3) and the formation of liquid film for relatively cool walls (OP 0 and 1), thermal contact times and total heat transfer to droplets are extensively altering from OP to OP. As the observations from Figure 7.30 prove, this significantly affects the location of ammonia sources as a function of the particular operating conditions. In that sense, OP3, for which surface temperatures are well above the Leidenfrost point is most disadvantageous and the low OPs are generally favorable, as less liquid passes through the mixer. The consequences of these observations for the ammonia homogenization process will be discussed in the next subsection.

7.6.3 Impact of the Ammonia Source Location on the Homogenization

The simulated ammonia vapour distribution on sections along the exhaust system has been evaluated according to the method in Section 7.3 for all four operating points. The Results are illustrated in Figure 7.31. The ammonia concentration is colour scaled with individual upper and lower scale limits for each OP in order to visualize the development along the pipe for each OP. In all cases, a local concentration similar to the OP's average concentration that is expected for an ideal mixing (see Equation 7.3) is coloured green.

The figure reveals a correlation between a fast preparation of the UWS close to the mixing element and a good homogenization of ammonia within the mixing length (OP 0 and 1). The inset for OP 1 (green circle) shows that the majority of the ammonia is released from the center of the mixer, which is a result of the direct impingement and intermediate film formation of the UWS spray. The same is valid for OP 0. From this central position the homogenization occurs within a very short distance, due to the highly turbulent swirl flow, see also the turbulent viscosity evolution in Figure 7.25.

In case of OP 3, the Leidenfrost effect prevents significant ammonia formation at the mix-
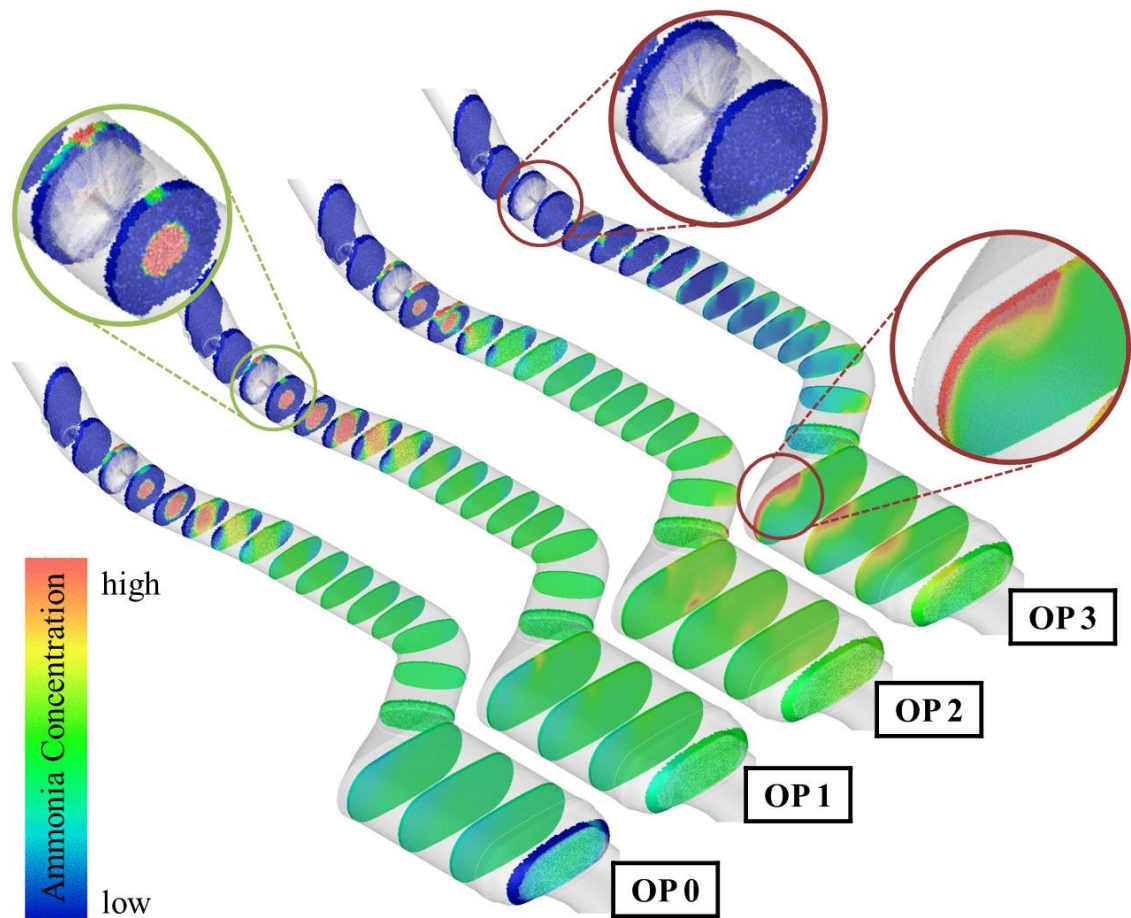
Figure 7.31:   *Quasi-steady ammonia distribution on sections along the SCR system, all OPs*

ing element (upper brown inset in Figure 7.31). Instead, a successive monotonic increase of the ammonia concentration can be observed downstream due to the evaporation of secondary droplets (Figure 7.30) along the mixing section. As a consequence, the mixing procedure is less efficient. Droplets, hitting the catalyst, make the inhomogeneity even worse (compare lower brown inset of Figure 7.31 to Figure 7.30). For OP 2 a superposition of both effects from OP 0/1 and OP 3 can be seen.

A quantification of the trends is given in Figure 7.32, which shows the ammonia mean values in every section.

The plot confirms the complete and early ammonia release at the mixing element in OP 1. The average section ammonia concentration reaches $100\,\%$ of the total injected amount immediately after the mixer. The value remains constant along the pipe as the released ammonia is solely travelling down the pipe. The same is valid for OP 0, despite the fact that only $80\,\%$ of injected ammonia is released from the UWS. The remaining $20\,\%$ is stored in liquid film that
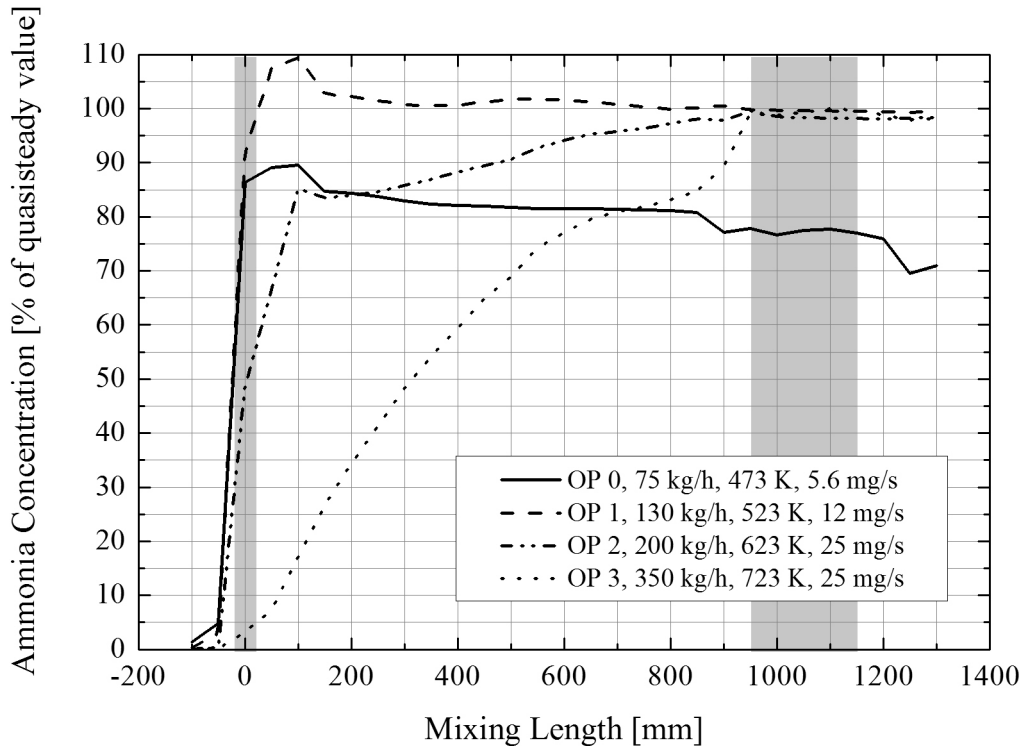
Figure 7.32: *Time averaged ammonia concentration along the SCR-mixing-section for all OPs*

has not been completely evaporated when the next injection starts. Further details about this incomplete liquid film decomposition and resulting deposition risks will be discussed in the next subsection.

The monotonic increase of the mean concentration along the mixing pipe for OP 3 mirrors the successive release of ammonia from secondary droplets. In this case, the evaporation of UWS is primarily driven by droplet-gas-heat transfer and - to some extent - heat transfer from pipe walls to sliding droplets (see regime discussion in Figure 6.11). The steep increase in ammonia release between 900 and $950\,mm$ is the consequence of droplets finally reaching the catalyst. As the latter is modelled as a barrier for droplets, they evaporate at the bricks intake surface, releasing the rest of ammonia very locally (see lower inset in Figure 7.31). The intermediate location of the curve for OP 2 in Figure 7.32 underlines its location on the border between wall wetting and non-wetting regimes in the Bai-model formulation. Approximately $50\,\%$ of ammonia is directly released at the mixing element and another $30\,\%$ as a consequence of droplet impingement very close to it. The remaining droplets behave similar to OP 3, but, as a consequence of lower gas temperatures for OP2, a smaller gradient of ammonia concentration increase occurs along the mixing section. Despite this fact, the amount of ammonia released at the catalyst is lower in OP 2, as fewer droplets pass the mixer.

121

The increase above $100\,\%$ for OP 1 at 100 mm, and the following slight oscillations can be explained with reference to the transport velocity assumption that underlies the determination of the quasi-steady concentration by Equation 7.3. Despite those small deviations, the observations, resulting from the quasi-steady analysis, give a very good insight in the UWS preparation process.

Figure 7.33 in comparison to Figure 7.32, finally quantifies the impact of ammonia source location on the homogenization process. The diagram shows the ammonia uniformity index along the mixing section for all OPs.
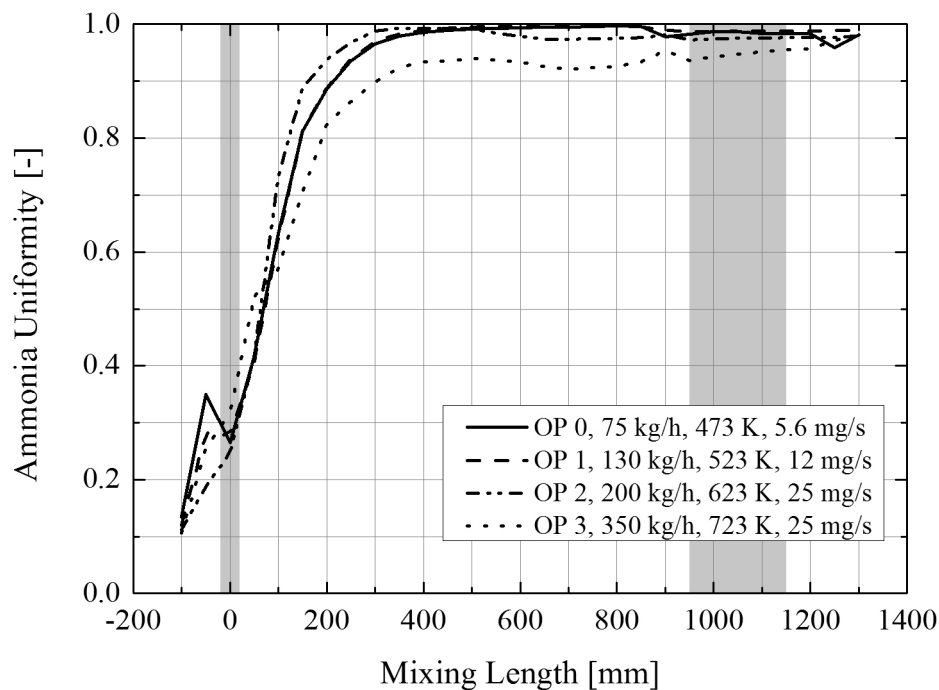

Figure 7.33: *Ammonia Uniformity-Index on cross sections along the SCR-system for all OPs*

Though all OPs basically reach a high uniformity index at the catalyst intake, differences occur between them. The major finding is that an early release of ammonia leads to a longer available mixing length and therefore a better homogenization. OP 0 and 1 reach the highest level of uniformity at the catalyst due to a fast mixing in the strong turbulent swirl close to the mixer. Though OP 2 shows the highest level of homogenization at the beginning of the mixing section for the same reason, the late local release of ammonia from droplets in OP 2 reduces the homogenization level again. Those droplets primarily evaporate at the outer wall of the pipe bend and the remaining mixing length is not sufficient to fully compensate this local ammonia release (see Figures 7.30 and 7.31). For OP 3 the level of uniformity is generally below the other OPs, due to late ammonia release and the less efficient homogenization of the

liquid phase UWS (droplet inertia). Additionally, a noticeable uniformity decrease occurs at the catalyst inlet due to droplets reaching the brick (Figure 7.30).

Figure 7.34 summarizes those observations on the dynamics of liquid UWS and their impact on the location of ammonia sources.
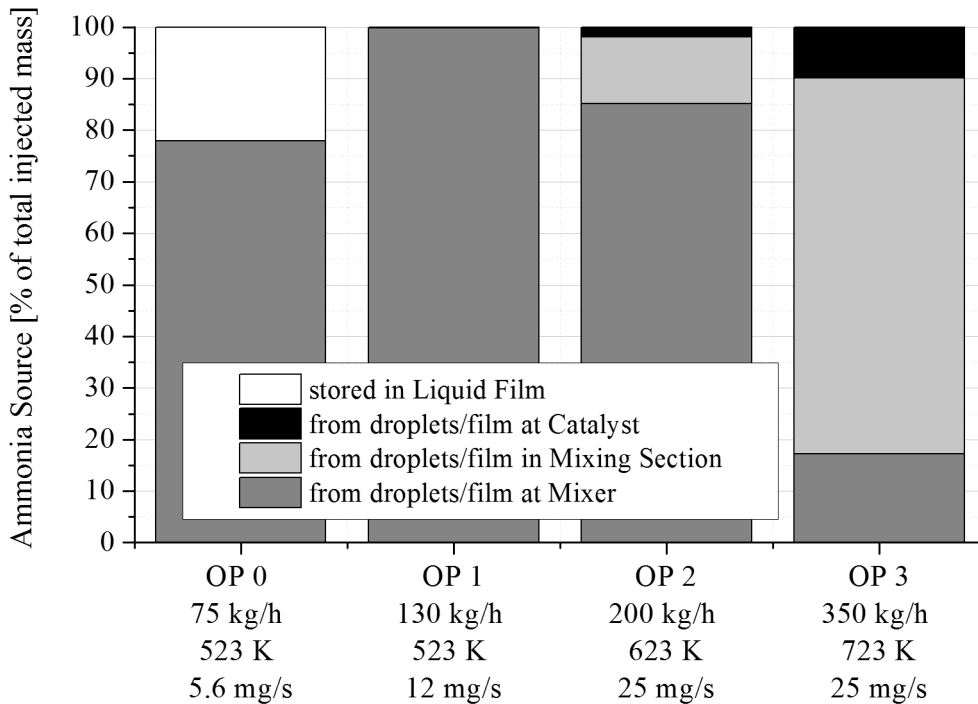

Figure 7.34:   *Ammonia source terms as a function of the OP*

Together with Figure 7.27, theses results confirm the **significant correlation between ammonia source location and homogenization level at the SCR catalyst**. The non-linear trend of the ammonia uniformity (Figure 7.27) can exactly be found in the proportion of upstream located ammonia sources (Figure 7.34, grey).

An more detailed comparison with Figure 7.26 also confirms the dominating impact of ammonia source location over the turbulent flow properties. In the present exhaust system, **any benefit from a higher turbulence level at high exhaust gas flows, is overcompensated by the disadvantageous liquid phase dynamics at high gas temperatures (Leidenfrost effect at the mixer)**. From a technical point of view, those results imply that the mixer's function as an evaporation enhancer and droplet barrier is at least as important as its turbulence inducing function. Moreover, the latter function can even only be sufficiently exploited, if the former is. Any optimizing measures on an SCR system should respect this fact.

7.6.4 Liquid Film Formation and Deposition Risk

Though no chemical mechanism is explicitly implemented and no multi-injection scenarios have been simulated for the production type SCR system, the CFD method allows for a first qualitative estimate of deposition risk. A major indicator for the formation of a permanent solid deposit that can be gained from the CFD study is the cumulation of liquid film. As the results from Section 6 revealed, the latter is promoted by residual liquid film and an insufficient wall temperature recovery after one injection period, i.e. when the next injection event starts.

A conclusive overview of those deposition risk factors for the present SCR system is given in Figure 7.35. Both indicators are shown as a function of operating conditions. The temper-

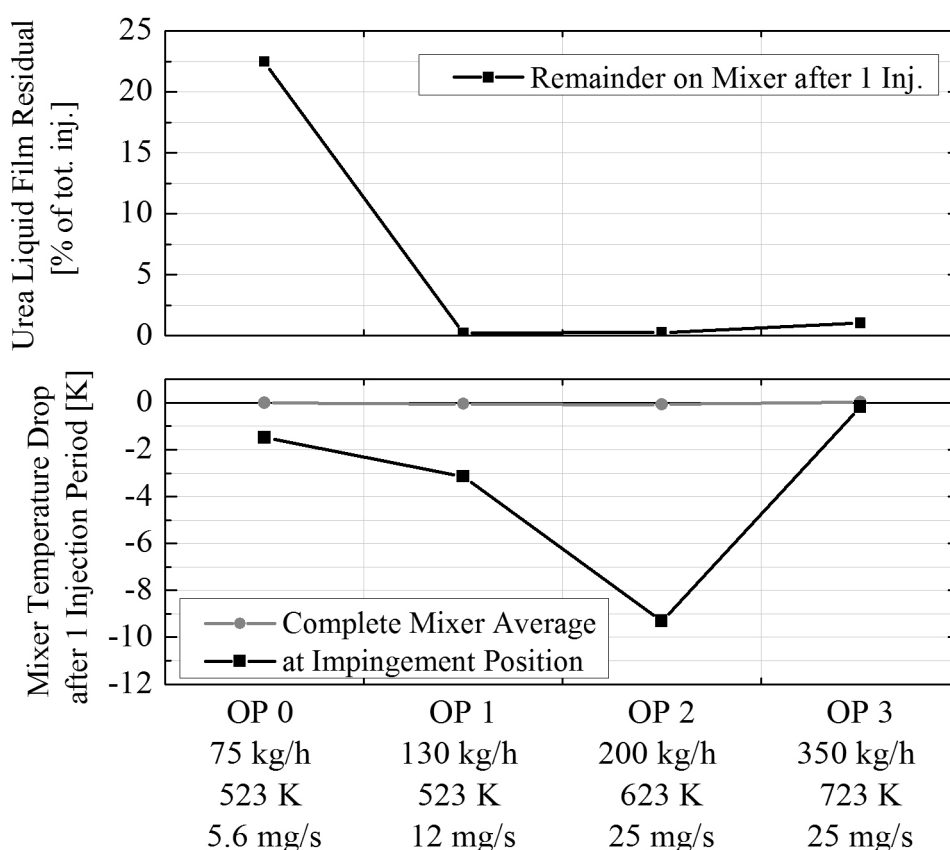Figure 7.35: *Deposition risk factors, incomplete liquid film evaporation and surface temperature drop, as a function of operating conditions*

ature drop after the first injection period has been evaluated for the complete mixer (average value) and at the primary impingement position on the mixer. The latter coincides with the position of maximum cooling and unevaporated liquid film, see also Figure 7.36.

Accordingly, OP0 fulfills both criteria for the onset and accumulation of a permanent liquid film. Considering the gas temperature in the liquid puddle region around $515\,K$ and the reaction mechanism according to Figure 2.3, these conditions allow for the solidification to biureth and higher compounds like CYA. For OP1 and 2 a deposition prognosis from the single injection event is less definite and reliable. In those cases no appreciable liquid film urea can be observed at the end of the first injection interval. However, a surface temperature drop remains that may - as proved in Section 6.4 - also lead to permanent wall wetting in the long run. For OP3 the system seems uncritical with respect to both factors at the mixer, but has shown a significant amount of liquid UWS reaching the catalyst surface, see Figure 1.5, right, with possible consequences.

The CFD simulation predicts that the unevaporated liquid film is - if present at all - limited to the mixing element and the injector recess for all OPs. For OP0 the location of undesired remaining liquid film on the mixer can be seen in Figure 7.36, right. The inner blade region, where the primary spray impinges is especially critical. At present, no experimental data is
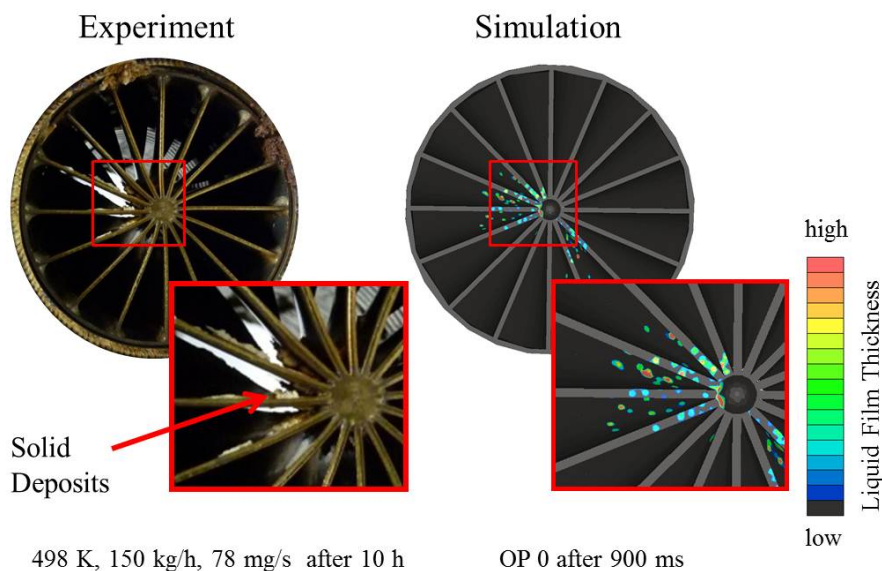
Figure 7.36: *Location of undesired deposits from $10\,h$-dosing experiment (left) [7] and simulated liquid film remainder for OP0 (right)*

available to *directly* validate the CFD deposition prognosis for the particular SCR system. However, for qualitative validation purposes, the l.h.s. of Figure 7.36 shows the solid deposits, observed during an experimental $10\,h$ long-term test, which has been conducted for a very similar SCR system geometry [7]. This includes an analogous mixing element and injector, as well as relative positioning. Though the different exhaust gas and injection boundary conditions (see Figure 7.36) prohibit a quantitative comparison of deposition extent, a comparison of critical regions can be regarded as reasonable. With respect to the latter, the CFD

prediction is in good accordance with experiment. This correlation allows one to conclude that the present CFD method has the potential to uncover critical spots in the SCR mixing section. An extension to a solidification modelling may additionally be considered on this basis.

8 Conclusion

The efficient reduction of nitric oxides formed during Diesel combustion with SCR-technology will contribute to the compliance of future exhaust legislation. In the present work, a CFD model has been implemented and validated to simulate the UWS preparation and ammonia homogenization in UWS based SCR systems.

A thermodynamic model of the UWS decomposition process has been implemented and validated. An evaporation approach for both water vaporization and urea thermolysis has been established as a reasonable model on the basis of available literature data on single UWS droplet decomposition. A rapid mixing description (infinite internal diffusion velocity) for the internal droplet components- and temperature distribution has been used as a computationally effective, but sufficiently precise description. The model displays the well known two stage decomposition of UWS with a valid D^2-law for water evaporation and urea thermolysis. Predicted evaporation and thermolysis time constants as a function of ambient gas conditions are in good agreement with measurements. Though secondary reaction paths of urea, leading to undesired deposits, have been neglected in the current model formulation, the droplet temperature and concentration predictions during the thermolysis stage allow for an explanation of experimentally-observed crust formation and resulting micro-explosions. The model is therefore capable of an extension to a more detailed solidification model.

The simulation of liquid UWS in the turbulent exhaust gas has been performed in an Euler-Lagrange framework. Droplet-wall interaction and liquid film formation have been studied and validated on the basis of videoanalysis, IR-thermography and FTIR- concentration data. The multi-regime Bai-impingement model has been adopted to predict wall wetting behavior for a wide range of exhaust gas conditions. Key factors are the determination of the deposition limit temperature and the critical Weber numbers separating splash and deposition regimes. Moreover, the break-up and slide regime boundaries have been adapted to consider wall cooling effects beyond the deposition limit temperature. Based on experiments, a single physically motivated parametrization has been extracted that captures phenomena ranging from massive wall wetting at low system wall temperatures to the thermal break-up and Leidenfrost phenomenon at elevated surface temperatures. The nonlinear thermal film-wall-interaction has been captured by an adoption of the Nukiyama-pool boiling model to UWS on the basis of literature findings. The submodel allows for a qualitative prediction of wall cooling on long time scales, but may be further optimized by an extended parameter adjustment.

The long-time behavior of wall film formation and dynamics and their correlation to surface temperatures has been studied with both CFD and experiment. The analysis confirms

the relevance of wall cooling effects on long time scales, which may lead to a change in spray impingement behavior. If wall temperatures are close to the deposition limit value, a transition from intermittent wall wetting to permanent wall film formation can be observed. The transition coincides with a significant wall temperature drop at the impingement position. For low temperatures a fast demixing of UWS has been numerically observed, which leads to liquid films consisting of a pure urea melt. The observation has been confirmed by a laboratory analysis of the film composition. The effect of liquid film formation on the timescales of ammonia release has been determined for massive wall wetting conditions. A significant urea buffering, leading to retardation of ammonia release in the order of minutes, has been observed. This proves the importance of avoiding permanent wall wetting in a production type SCR system to achieve a stable dosing control.

On the basis of the validated UWS liquid phase- and decomposition model, the impact of the turbulence model and numerical spatial discretisation scheme on the prediction of the ammonia homogenization in a production type SCR system has been studied. A high-Reynolds- and RNG-formulation of the k-ε-model have been compared to a Reynolds stress model. Only the RSM has been found to properly predict turbulent kinetic energy and dissipation in the swirl exhaust flow, where anisotropic effects in turbulence become significant. As a consequence, higher turbulent viscosity values have been observed in the mixing section for the RSM than for the two-equation models. This leads to increased turbulent diffusion and more realistic ammonia uniformity predictions at the catalyst. The underestimation of ammonia homogenization, common to reviewed two-equation model approaches, was significantly reduced. With the optimized CFD setup, maximum deviations from ammonia uniformity measurements are well below two percent for a wide range of operating conditions. At the same time the computational effort for the RSM is only about 20 percent higher than for the k-ε-models. The study has further proved that a first order spatial discretisation scheme leads to severe numerical diffusion of the ammonia scalar for state-of-the-art mesh resolutions. The RSM in combination with a higher order discretisation scheme is therefore regarded as the best choice for a precise but efficient turbulence- and ammonia transport simulation.

The present study further revealed the importance of the complex droplet-wall-interaction submodel used for predictive CFD simulation of the processes in the SCR-mixing section. By employing the adapted multi-regime Bai-model, the measured nonlinear trend of ammonia uniformity at the catalyst with exhaust gas flow rate and temperature has been predicted correctly over a wide range of exhaust gas conditions. Moreover, the complex two-phase model gives detailed insights into the impact of ammonia source location on the homogenization process. A general correlation between fast UWS preparation and high ammonia uniformity at the catalyst has been proved. Interestingly, high temperature operating conditions are especially critical with respect to this topic. In these cases the Leidenfrost effect may lead to a significant amount of liquid UWS reaching the catalyst surface. Moreover, the model allows for the prediction of incomplete liquid film decomposition and therefore an estimation of deposition risk. This is especially relevant at very low exhaust temperatures.

In conclusion, the present CFD method allows for an accurate evaluation and optimization of SCR-mixing systems.

For further model improvement an extension of the droplet impingement description, taking the thermal contact time into account on a physical basis, may be beneficial. The latter may avoid the semi-empirical adaptation of sliding-droplet Weber numbers, to capture thermal contact beyond the Leidenfrost temperature. LDA measurements and/or LES simulations may moreover be employed to directly validate the turbulent exhaust gas flow field, predicted by the RSM.

As UWS dosing is successively shifted to lower exhaust gas temperatures to fulfill future emission limits, modelling the deposition formation from residual liquid film will be an important future research topic. The presented CFD method offers a promising basis for such an extension. A probable future alternative to direct spray injection of UWS may be the blow-in of gaseous ammonia from a preconditioning reactor. The turbulent gas phase- and species mixing studies of the present work may be directly transferred to those applications.

Bibliography

[1] W. Reuter and F. Terres. Appropriate NOx Aftertreatment solutions for different Markets and Applications. In *20th Aachen Colloquium Automobile and Engine Technology*, 2011.

[2] H.-J. Brüne, J. Honeder, P. Raschl, M. Schinnerl, and R. Tangemann. Diesel-Emissionstechniken von BMW für künftige weltweite Abgasnormen. *Motorentechnische Zeitschrift*, 03:210–216, 2009.

[3] T. V. Johnson. Diesel Emission control in Review. *SAE Int. J. Fuels Lubric.*, 01-0121: 1–12, 2009.

[4] M. Heseding, M. Nitsche, and J. Slama. Politische Randbedingungen für die Förderung umweltfreundlicher AGN-Technologien für Industriemotoren. In *8. FAD-Konferenz, Herausforderung - Abgasnachbehandlung für Dieselmotoren*, 2010.

[5] C. Brinkmeier, F. Opferkuch, U. Tuttlies, V. Schmeißer, J. Bernnat, and G. Eigenberger. Autoabgasreinigung - eine Herausforderung für die Verfahrenstechnik. *Chemie Ingenieur Technik*, 77 (9):1333–1355, 2005.

[6] M. Koebel and E. O. Strutz. Thermal and Hydrolytic Decomposition of Urea for Automotive Selective Catalytic Reduction Systems: Thermochemical and Practical Aspects. *Ind. Eng. Chem. Res.*, 42:2093–2100, 2003.

[7] R. Bitto, S. Fischer, W. Weissel, B. Keppeler, and T. Beckmann. Weiterentwicklung von PKW-SCR-Systemen mit Hilfe von Motorprüfstandsuntersuchungen und CFD-Simulationsrechnungen. In *19. Aachener Kolloquium Fahrzeug- und Motorentechnik 2010*, number 19. Aachener Kolloquium Fahrzeug und Motorentechnik 2010, Aachen, 2010.

[8] R. Bitto. Internal Measurements - IFA. Technical report, Institute For Powertrains and Automotive Technology, Vienna University of Technology, 2010.

[9] L. Xu, W. Watkins, R. Snow, G. Graham, R. McCabe, C. Lambert, and R.O. Carter III. Laboratory and Engine Study of Urea-Related Deposits in Diesel Urea-SCR After-Treatment Systems. *SAE Technical Paper Series*, 01-1582, 2007.

[10] A. Zheng, A. Fila, A. Kotrba, and R. Floyd. Investigation of Urea Deposits in Urea SCR Systems for Medium and Heavy Duty Trucks. *SAE Technical Paper Series*, 01-1941, 2010.

[11] E. Abu-Ramadan, K. Saha, and X. Li. Modeling of the Injection and Decomposition Processes of Urea-Water-Solution Spray in Automotive SCR Systems. *SAE Technical Paper Series*, 01-1317, 2011.

[12] M. Koebel, M. Elsener, and M. Kleemann. Urea-SCR: a promising technique to reduce NOx emissions from automotive diesel engines. *Catalysis Today*, 59:335–345, 2000.

[13] M. Chen and S. Williams. Modelling and Optimization of SCR-Exhaust Aftertreatment Systems. *SAE Technical Paper Series*, 01-0969, 2005.

[14] F. Birkhold, U. Meingast, P. Wassermann, and O. Deutschmann. Modeling and simulation of the injection of urea-water-solution for automotive SCR DeNOx-systems. *Applied Catalysis B: Environmental*, 70:119–127, 2007.

[15] S. Kontin, A. Höfler, R. Koch, and H.J. Bauer. Evaporation and Concurrent Crystallisation of Single AdBlue-Particles. In *Berichte zur Energie- und Verfahrenstechnik - Engine Combustion Processes Xth Congress*, volume 11, pages 187–198. Prof. Dr.-Ing. Alfred Leipertz, 2011.

[16] A. Lundström. *Urea Decomposition for Urea- SCR Applications*. PhD thesis, Department of Chemical and Biological Engineering, Chalmers University of Technology, 2010.

[17] F. Birkhold. *Selektive Katalytische Reduktion von Stickoxiden: Untersuchung der Einspritzung von Harnstoffwasserlösung*. PhD thesis, Fakultät für Maschinenbau, Universität Karlsruhe, 2007.

[18] S. D. Yim, S.J. Kim, J.H. Baik, and I. Nam. Decomposition of Urea into NH3 for the SCR Process. *Ind. Eng. Chem. Res.*, 43:4856–4863, 2004.

[19] S. Musa, M. Saito, T. Furuhata, and M. Arai. Evaporation Characteristics of a Single Aqueous Urea Solution Droplet. *ICLASS-2006*, ICLASS06-195, 2006.

[20] T. J. Wang, S. W. Baek, and S. Y. Lee. Experimental Investigation on Evaporation of Urea-Water-Solution Droplet for SCR Applications. *AIChE Journal*, 55, No.12:3267–3276, 2009.

[21] J. Kim, S. H. Ryu, and J. Soo Ha. Numerical Predictions on the Characteristics of Spray-Induced Mixing and Thermal Decomposition of Urea Solution in SCR System. In *ASME 2004 Internal Combustion Engine Division Fall Technical Conference*, 2004.

[22] P.M. Schaber, J. Colson, S. Higgins, D. Thielen, B. Anspach, and J. Brauer. Thermal decomposition (pyrolysis) of urea in an open reaction vessel. *Thermochimica Acta*, 424:131–142, 2004.

[23] H.L. Fang and H. F. M. DaCosta. Urea thermolysis and NOx reduction with and without SCR catalysts. *Applied Catalysis B: Environmental*, 46:17–34, 2003.

[24] A. Lundström, B. Andersson, and L. Olsson. Urea thermolysis studied under flow reactor conditions using DSC and FT-IR. *Chemical Engineering Journal*, 150:544–550, 2009.

[25] A. Nishioka, Y. Sukegawa, K. Katogi, H. Mamada, T. Kowatari, T. Mukai, and H. Yokota. A study of a New Aftertreatment System (2): Control of Urea Solution Spray for Urea-SCR. *SAE Technical Paper Series*, 01-0644, 2006.

[26] J. Seo. Aftertreatment Package Design for SCR Performance Optimization. *SAE Technical Paper Series*, 01-1135, 2011.

[27] C.K. Law and H.K. Law. A d2-Law for Multicomponent Droplet Vaporization and Combustion. *AIAA Journal*, 20, No 4:522–530, 1981.

[28] Y. Zhao, B. Jiang, and H. Fang. Experimental study of the effects of wind speed, radiation, and wet bulb diameter on wet bulb temperature. *Experimental Thermal and Fluid Science*, 5, Issue 6:790–794, 1992.

[29] J.-R. Yang and S.-C. Wong. An experimental and theoretical sudy of the effects of heat conduction through the support fiber on the evaporation of a droplet in a weakly convective flow. *International Journal of Heat and Mass Transfer*, 45:4589–4598, 2002.

[30] J.-R. Yang and S.-C. Wong. On the discrepancies between theoretical and experimental results for microgravity droplet evaporation. *International Journal of Heat and Mass Transfer*, 44:4433–4443, 2001.

[31] E. Abu-Ramadan, K. Saha, and X. Li. Modeling the Depletion Mechanism of Urea-Water-Solution Droplet for Automotive Selective Catalytic Reduction Systems. *AIChE Journal*, 0:1–16, 2011.

[32] B. A. Al Zaitone and C. Tropea. Evaporation of pure liquid droplets: Comparison of droplet evaporation in an acoustic field versus glass-filament. *Chemical Engineering Science*, 66:3914–3921, 2011.

[33] H. Schiffter and G. Lee. Single-Droplet Evaporation Kinetics and Particle Formation in an Acoustic Levitator. Part 1: Evaporation of Water Microdroplets Assessed using Boundary-Layer and Acoustic Levitation Theories. *Journal of Pharmaceutical Sciences*, 96:2274–2283, 2007.

[34] A.L. Yarin, G. Brenn, and D. Rensink. Evaporation of acoustically levitated droplets of binary liquid mixtures. *International Journal of Heat and Fluid Flow*, 23:471–486, 2002.

[35] V. O. Strots, S. Santhanam, B.J. Adelam, G.A. Griffin, and E.M. Derybowski. Deposit Formation in Urea-SCR Systems. *SAE Int. J. Fuels Lubric.*, 2:283–289, 2009.

[36] G. Salanta, G. Zheng, A. Kotrba, R. Rampazzo, and L. Bergantim. Optimization of a Urea SCR System for On-Highwa Truck Applications. *SAE Technical Paper Series*, 01-1938, 2010.

[37] A. Lundström, B. Waldheim, H. Ström, and B. Westerberg. Modeling of urea gas phase thermolysis and theoretical details on urea evaporation. *Proceedings of the Institution of Mechanical Engineers, Part D: Journal of Automobile Engineering*, 225:1392–1398, 2011.

[38] S. Bhattacharjee and D. C. Haworth. CFD Modeling of Processes Upstream of the Catalyst for Urea SCR Reduction Systems in Heavy-Duty Diesel Applications. *SAE Technical Paper Series*, 01-1322, 2011.

[39] F. Birkhold, U. Meingast, P. Wassermann, and O. Deutschmann. Analysis of the Injection of Urea-water-solution for automotive SCR DeNOx-Systems: Modeling of Two-phase Flow and Spray/Wall-Interaction. *SAE Technical Paper Series*, 01-0643, 2006.

[40] H. Ström, A. Lundström, and B. Andersson. Choice of urea-spray models in CFD simulations of urea-SCR systems. *Chemical Engineering Journal*, 150:69–82, 2009.

[41] Y. Yi. Development of a 3D Numerical Model for Predicting Spray, Urea Decomposition and Mixing in SCR Systems. *SAE Technical Paper Series*, 01-3985:1–11, 2007.

[42] A. Munnannur and G. Z. Liu. Development an Validation of aPredictive Model for DEF Injection and Urea Decomposition in Mobile SCR DeNOx Systems. *SAE Technical Paper Series*, 01-0889, 2010.

[43] S. Rajadurai. Improved NOx Reduction Using Wiremesh Theemolysis Mixer in Urea SCR System. *SAE Technical Paper Series*, 01-2636, 2008.

[44] S. Kontin, A. Höfler, R. Koch, and H.J. Bauer. Heat and Mass Transfer accompanied by Cristallisation of single Particles containing Urea-water-solution. In *ILASS-Europe 2010, 23rd Annual Conference on Liquid Atomization and spray Systems*, 2010.

[45] S.-J. Jeong, S.-J. Lee, W.S. Kim, and C. B. Lee. Simulation on the Otimum Shape and Location of Urea Injector for Urea-SCR System of Heay-duty Diesel Engine to Prevent NH3 Slip. *SAE Technical Paper Series*, 01-3886, 2005.

[46] *Methodology STAR-CD Version 4.16*. CD adapco Ltd., 2011.

[47] G. Zheng, P. Palmer, G. Salanta, and A. Kotrba. Mixer Development for Urea SCR Applications. *SAE Technical Paper Series*, 01-2879, 2009.

[48] E.P. Perman and T. Lovett. Vapour pressure and heat dilution of aqueous solutions. *Trans. Farad. Soc.*, 22, 1926.

[49] V. Ebrahimian, A. Nicolle, and C. Habchi. Detailed Modeling of the Evaporation and Thermal Decomposition of Urea-Water Solution in SCR Systems. *AIChE Journal*, 0: 1–12, 2011.

[50] D. Ferro, G. Barone, G. Della Gatta, and V. Piacente. Vapour pressures and sublimation enthalpies of urea and some of its derivatives. *J. Chem. Thermodynamics*, 19:915–923, 1987.

[51] C. L. Yaws. *Chemical Properties Handbook*. McGraw-Hill, New York, 1999.

[52] DIPPR database, Project 801. Evaluated Thermophysical Property Database. V 4.0.0. URL `http://www.aiche.org/dippr`.

[53] V.N. Emelyanenko, G.J. Kabo, and S.P. Verevkin. Measurement and prediction of thermochemical properties: improved increments for the estimation of enthalpies of sublimation and standard enthalpies of formation of alkyl derivatives of urea. *J Chem Eng Data*, 51:79–87, 2006.

[54] H.Aoki, T. Fujiwara, Y.E. Morozumi, and T. Miura. Measurements of urea thermal decomposition reaction for NO selective non-catalytic reduction. In *5th International Conference on Technologies and Combustion for a Clean Environment, Lisbon, Portugal*, pages 115–118, 1999.

[55] W.E Ranz and W.R. Marshall. Evaporation from drops: Parts I and II. *Chem. Eng. Prog.*, 48(3):141, 1952.

[56] M.M. El Wakil, O.A. Ueyhara, and P.S. Myers. A theoretical investigation of the heating-up period of injected fuel droplets vaporizing in air. *NACA Technical Note 3179*, 1954.

[57] D. Kuhnke. *Spray/Wall- Interaction Modelling by Dimensionless Data Analysis*. PhD thesis, TU Darmstadt, 2004.

[58] C. Bai and D. Gosman. Development of Methodology for Spray Impingement Simulation. *SAE Technical Paper Series*, 950283:69–87, 1995.

[59] D. W. Stanton and C. J. Rutland. Multi-dimensional modeling of thin liquid film and spray-wall interactions resulting from impinging sprays. *International Journal of Heat and Mass Transfer*, 41:3037–3054, 1998.

[60] C. Bai and D. Gosman. Mathematical Modelling of Wall Films Formed by Impinging Sprays. *SAE Technical Paper Series*, 960626:1–15, 1996.

[61] D. W. Stanton and C. J. Rutland. Modeling Fuel Film Formation and Wall Interaction in Diesel Engines. *SAE Technical Paper Series*, 960628:29–45, 1996.

[62] *FLUENT 6.3 User's Guide*, 9 2006.

[63] *User Guide FIRE 8.4*, 2005.

[64] M. A. Friedrich, H. Lan, J. A. Drallmeier, and B. F. Armaly. A separation criterion with experimental validation for shear-driven films in separated flows. *ASME J. Fluids Engineering*, 2007.

[65] M. Ledoux. *Modelisation des Sprays*. Cours de DEA, 1993.

[66] F.M. White. *Heat and Mass Transfer*. Addison Wesley, 1988.

[67] Pool Boiling Regimes. online, July 2010.

[68] Y. S. Hong, S. M. You, C. N. Ammerman, and J. Y. Chang. Ordered and Chaotic Bubble Departure Behavior During Film Boiling. *ASME IMECE - Visualization of Thermal Phenomen*, 1996.

[69] H. Sakashita, A. Ono, and Y. Nakabayashi. Measurement of critical heat flux and liquid-vapour structure near the heating surface in pool boiling of 2-propanol/water mixtures. *International Journal of Heat and Fluid Flow*, 53:1554–1562, 2010.

[70] M. Taboas, M. Vallès, M. Bourouis, and A. Coronas. Pool boiling of ammonia/water and its pure components: Comparison of experimantal data in the literature with the predictions of standard correlations. *International Journal of Refrigeration*, 30:778–788, 2007.

[71] V.V. Yagov. Critical Heat Flux prediction for pool boiling of binary mixtures. *Trans IChemE*, 82 (A4):457–461, 2004.

[72] C.D. Henry and J. Kim. A study of the effects of heater size, subcooling, and gravity level on pool boiling heat transfer. *International Journal of Heat and Fluid Flow*, 25: 262–273, 2004.

[73] C.M. Rops, R. Lindken, J.F.M. Velthius, and J. Westerweel. Enhanced heat transfer in confined pool boiling. *International Journal of Heat and Fluid Flow*, 30:751–760, 2009.

[74] S. G. Kandlikar, M.E. Steinke, and S. Ashish. Effects of Weber number and surface temperature on the boiling and spreading characteristics of impinging water droplets. In *Proceedings of NHTC 2001, 35th National Heat Transfer Conference*, Anaheim,CA,, 2001.

[75] F. Pischinger. Abschlussbericht SFB 224: Motorische Verbrennung. Technical report, SFB 224 RWTH Aachen, 2001.

[76] N. Wruck. *Transientes Sieden von Tropfen beim Wandaufprall*. PhD thesis, Fakultät für Maschinenwesen, RWTH Aachen, 1998.

[77] A. Moriyama, K. Araki, and T. Okouchi. Heat Transfer from Hot Metal Surafce to an Impinging Water Droplet in Transitional Boiling Regime. In *12th Japan Conference on Liquid Atomization and Spay Systems, The Fuel society of Japan*, Tokyo,, 1984.

[78] U. Meingast. *Spray/ Wand-Wechselwirkung bei der dieselmotorischen Direktein-spritzung*. PhD thesis, Fakultät für Maschinenwesen, RWTH Aachen, 2003.

[79] F. Akao, K. Araki, S. Mori, and A. Moriyama. Deformation Behaviors of a Liquid Droplet Impinging onto Hot Metal Surface. *Trans. Iron and Steel Institute of Japan*, 20:737–743, 1980.

[80] J.E. Eckhause and R.D. Reitz. Modeling heat transfer to impinging fuel sprays in direct-injection engines. *Atomization and Sprays*, 5:213–242, 1995.

[81] W.M. Rohsenow. A method of correlating heat transfer data for surface boiling of liquids. *Transactions of the ASME*, 74:969–976, 1952.

[82] Z. Li, J. Deng, L. Li, L. Cao, and Z. Wu. A Study on the Facotrs Affecting Heated Wall Impinging Characteristics of SCR Spray. *SAE Technical Paper Series*, 01-1311, 2011.

[83] F. Puschmann. *Experimentelle Untersuchung der Spraykühlung zur Qual-itätsverbesserung durh definierte Einstellung des Wärmeübergangs*. PhD thesis, Fakultät für Verfahrens- und Systemtechnik, Otto-von-Guericke-Inuversität Magde-burg, 2003.

[84] M. Ciofalo, A. Caronia, M. Di Liberto, and S. Puleo. The Nukiyama curve in water spray cooling: Its derivation from temperature-time histories and its dependence on the quantities that characterize deop impact. *International Journal of Heat and Mass Transfer*, 50:4948–4966, 2007.

[85] S. Fest-Santini. *Wärmeübergang bei der Spraykühlung mit intermittierenden Srays oberhalb der Leidenfrosttemperatur*. PhD thesis, Fakultät für Verfahrens- und Sys-temtechnik, Otto-von-Guericke-Inuversität Magdeburg, 2009.

[86] J. H. Ferziger and M. Peric. *Computional Methods for Fluid Dynamics*. Springer, Berlin,, 2002.

[87] S.H. El-Tahry. A Comparison of Three Turbulence Models in Engine-Like Geometries. In *International Symposium on Diagnostics and Modelling of Combustion in Reciprocating Engines*, pages 203–213, Commodia,, 1985. JSME-Fluid Mechanics Department, JSME.

[88] Y. Tominaga and T. Stathopoulos. Turbulent Schmidt numbers for CFD analysis with various types of flowfield. 41:8091–8099, 2007.

[89] F. Obermeier and H. Chaves. Initial modelling of splashing phenomena. *IDEA Project, Subprogram A3*, 1991.

[90] J. Gehrlein, A. Lang, and G. Palmer. Optimierung von SCR-Systemen durch Integration von Mischelemente. *Motorentechnische Zeitschrift*, 03:218–223, 2009.

[91] X. Zhang, M. Romzek, and C. Morgan. 3-D Numerical Study of Mixing Characteristics of NH3 in Front of SCR. *SAE Technical Paper Series*, 01-3444, 2006.

[92] Ch. Krenn, Ch Samhaber, and G. Pessl. Simulation of Selective Catalytic Reduction (SCR) Systems. In *STAR European Conference, London*, London,, 2008. STAR European Conference, London.

[93] VDI-Gesellschaft, editor. *VDI-Wärmeatlas*. 10th edition. VDI-Verlag, 2006.

[94] *BASF Technisches Merkblatt M6221d- AdBlue*. BASF, 11 2006.

[95] J. Jäger, S. Nývlt, S. Horácek, and J. Gottfried. Viskositäten von Harnstofflösungen. *Collection Czechoslov. Chem. Commun.*, 30:2117–2121, 1965.

[96] A. Agrawal. Surface Tension of Polymers. Online, 06 2005. URL `http://web.mit.edu/nnf/education/wettability/summerreading-2005short.pdf`.

[97] M. Roseman and W. P. Jencks. Interaction of Urea and Other Polar Compounds in Water. *Journal of the American Chemical Society*, 97:3:631–640, 1975.

[98] R.B. Bird, E.W. Stewart, and E.N. Lightfoot. *Transport Phenomena*. John Wiley & Sons, New York, 1966.

[99] L. Möltner. Internal Measurements IFA: FTIR-concentration measurements in exhaust gas and liquid film composition. Technical report, Institute for Powertrains and Automotive Technology, Vienna University of Technology, 2008.

[100] W. J. Massman. A review of the molecular diffusivities of H2O, CO2, CH4, CO, O3, NH3,N2O, NO and NO2 in air, O2 and N2 near STP. *Atmospheric Environment*, 32, No. 6:1111–1127, 1998.

[101] J. Thompson, J. Beeck, E. Joubert, and T. Wilhelm. Case Studies of Urea SCR Integration on Passenger Cars - Monitoring of Urea Inside theTank During Hot and Cold Environment Test Missions. *SAE Technical Paper Series*, 01-1181, 2008.

[102] G. Stiesch. *Modeling Engine Spray and Combustion Processes*. Springer, Berlin,, 2003.

[103] Roughness and Surface Coefficients of Ventilation Ducts, 2012. URL $www.engineeringtoolbox.com/surface - roughness - ventilation - ducts - d_209.html$.

[104] L. Costantino, G. D'Errico, O. Ortona, and V. Vitagliano. Transport Properties of Urea and Alkyureas Aqueous Solutions. A Velocity Correlation Study. *Journal of Molecular Liquids*, 84:179–191, 2000.

[105] I. L. Pioro, W. Rohsenow, and S. S. Doerffer. Nucleate pool-boiling heat transfer. II: assessment of prediction methods. *International Journal of Heat and Mass Transfer*, 47:5045–5057, 2004.

[106] Wayne Rasband. *ImageJ v.1.44p - Image Processing and Analysis in Java*. National Institutes of Health, 2012. URL http://imagej.nih.gov/ij.

[107] J.M. Beer and N.H. Chigier. Combustion Aerodynamics. *Applied Science*, 1972.

[108] T. Burden. Isotropic Turbulence. online, 2008. URL http://www2.mech.kth.se/courses/5C1218/Isotropic.pdf.

[109] T. K. Flesch, J. H. Prueger, and J. L. Hatfield. Turbulent Schmidt number from a tracer experiment. 111:299–307, 2002.

[110] G. He, Y. Guo, and A. T. Hsu. The effect of Schmidt number on turbulent scalar mixing in a jet-in-crossflow. 42:3727–3738, 1999.

[111] V. K. Vijayaraghavan. Numerical Modeling of species transport in turbulent flow and experimental study on areosol sampling. 2006.

[112] M.S. Ying Huai. *Large Eddy Simulation in the Scalar Field*. PhD thesis, Fachbereich Maschinenbau, Technische Universität Darmstadt, 2005.

[113] L. Prandtl. *Strömungslehre*. Vieweg, 1965.

Curriculum Vitae

Simon Fischer

born 6th of July 1983 in Lichtenfels, Germany

since 03/2008 Vienna University of Technology, Austria: PhD Student and Project Assistant at the Institute for Powertrains and Automotive Technology

10/2004–01/2008 University of Bayreuth, Germany: Main studies of Physics (Diploma)

09/2002–10/2004 University of Bayreuth, Germany: Basic studies of Physics

09/1993–07/2002 Grammar School Alexandrinum Coburg, Germany: Allgemeine Hochschulreife (Abitur)

09/1989–07/1993 Primary School Ebersdorf b. Coburg, Germany